Integrated Silicon-based Photonic, Acoustic and Optomechanical Devices

by

Yangyang Liu

B.S., Hong Kong University of Science and Technology, 2010

M.S., University of Colorado Boulder, 2014

A thesis submitted to the

Faculty of the Graduate School of the

University of Colorado in partial fulfillment

of the requirements for the degree of

Doctor of Philosophy

Department of Electrical, Computer, and Energy Engineering

2018

This thesis entitled:
Integrated Silicon-based Photonic, Acoustic and Optomechanical Devices
written by Yangyang Liu
has been approved for the Department of Electrical, Computer, and Energy Engineering

---

Prof. Miloš Popović

Prof. Kelvin Wagner

Date ____________

The final copy of this thesis has been examined by the signatories, and we find that both the content and the form meet acceptable presentation standards of scholarly work in the above mentioned discipline.

Liu, Yangyang (Ph.D., Electrical Engineering)

Integrated Silicon-based Photonic, Acoustic and Optomechanical Devices

Thesis directed by Prof. Miloš Popović

Integration of photonic and other types of micro- and nanoscale devices in silicon and silicon-based material platforms allows one to leverage existing large-scale wafer-based manufacturing infrastructure and tools developed for the integrated circuit (IC) industry. This thesis explores chip-scale silicon photonic structures that include physical contacts that are intimate with the optical field, evanescent confinement of acoustic waves using slowness contrast silicon-based materials, and the implementation of optomechanical devices in monolithic CMOS microelectronics platforms. The unifying objective of this work was to make progress toward photonic and optomechanical devices that are densely integrable on chip, and potentially also monolithically with state-of-the-art transistors, in optical and optomechanical circuits.

Loss avoidance in photonic structures with contacts is designed and explained using a novel mechanism, imaginary coupling of modes. Periodic contacts are treated as an index perturbation and designed to radiatively couple two eigenmodes of the unperturbed structure, so as to construct a low-loss supermode with a field distribution pattern that "avoids" the contacts. Using this concept, a linear waveguide crossing array and a circular "wiggler" resonator are designed and experimentally demonstrated. The "wiggler" resonator is further suspended while sustaining a high quality factor above 100,000.

Evanescent confinement and guiding of elastic waves on chip based on material contrast is investigated theoretically in the context of silicon-based materials, as an alternative to confining acoustic waves using air-solid interfaces in suspended structures. Calculations of material intrinsic and radiation losses suggest that compact wavelength-scale acoustic/phononic devices can be built on chip to form complex circuitries.

Combining optics and acoustics, optical forces and integration of suspended optomechanical devices in CMOS microelectronics processes are explored. Waveguide design to maximize static radiation pressure in a vertically coupled dual ring structure, and the initial design of an optomechanical "wiggler" resonator are discussed. Post processing steps to suspend devices fabricated in an unmodified CMOS microelectronics process are proposed with current experimental progress presented.

Dedication

To my husband and parents.

Acknowledgements

My PhD study has been a long journey made possible with the help of many people. I am most grateful to my advisor, Prof. Miloš Popović, for patiently teaching me from the very basics of photonics, for fostering rigor and first principle understandings, and for guiding and supporting me throughout my graduate studies. My fellow group members, Xiaoge Zeng, Jeff Shainline, Cale Gentry, Mark Wade, Fabio Pavanello, Nathan Dostart, Yossi Ehrlichman and many others provided friendship and insightful discussions, and I am fortunate to have worked alongside them.

A lot of people from outside of my research group gave me tremendous support during some of the most difficult and frustrating times, while I was exploring post-processing options for device suspension. Joseph Brown taught me how to use a critical point dryer, Tomoko Borsa and Ryan Brow helped me extensively around CNL, David Alchenberger from JILA assisted with mechanical lapping of some very small chips, Amir Atabaki from MIT shared his experience on substrate transfer, JD Deng and Ling Xie from Harvard CNS provided valuable advice on etching.

I would like to thank Dr. Tymon Barwicz, Dave Riggs and other colleagues at IBM/GlobalFoundries for a memorable and rewarding internship experience. I thank my undergraduate thesis advisor, Prof. Andrew Poon, for first introducing me to the world of photonics, and for his continued guidance and encouragement. I thank Prof. Juliet Gopinath, Prof. Wounjhang Park, Prof. Kelvin Wagner and Dr. Anatoly Khilo for serving on my committee and for providing valuable advice.

Lastly, my deepest thanks is to my husband and my parents. It is their endless love and support that has carried me to the finish line. Without them, I would never have been able to reach where I am today.

Contents

Tables

Table

Figures

Figure

Chapter 1

Introduction

1.1 Integrated Silicon Photonics

Integrated photonics is the photonic (or optical) counterpart of integrated electronics, and studies the generation, transport, manipulation and detection of light in micro- or nano-scale structures on a planar semiconductor chip. Since silicon is the dominant material used in the manufacturing of electronic integrated circuits (IC), development of photonic devices and systems in the same material platform has naturally and rapidly attracted much research and commercial interest since the mid 1980's [95]. Compared to free space and fiber optics, integrated silicon photonics takes advantage of modern lithography now capable of defining features below 100 nm, and the high optical refractive index contrast between silicon and its oxide or air with good material transparency over telecom wavelengths, which together enable tight confinement of light in wavelength-scale structures that can be densely integrated to form complex photonic circuitries with various functionalities at a low cost.

Over the past few decades, an enormously wide range of passive and active photonic devices and systems have been developed in integrated silicon-based platforms. Outside of academic laboratories, commercial foundries and multi-project wafer (MPW) services provide more scalable platforms with easier integration with electronics. A few basic components form a standard library of building blocks, which can be used to construct more sophisticated systems [27]. Among these components, rectangular waveguides are the most fundamental structures which evanescently confine light in the high index silicon device layer, and permit bi-directional transport and routing.

Waveguide crossings allow photonic waveguides to cross each other, unlike electrical wires which short circuit when joined. Ring resonators are closed waveguide loops that provide spectrally selective resonant enhancement for discrete wavelengths that constructively interfere after each round trip. Directional couplers facilitate transfer of optical power between photonic structures by evanescently exciting a polarization current. Other common devices include spot-size converters and grating couplers for fiber-to-chip coupling, polarization splitters and rotators for polarization management, Y junctions for splitting and combining optical power, and electro-optic modulators for signal generation and manipulation.

The confinement and propagation of light in photonic devices, and in other media, is governed by Maxwell's equations. In a non-magnetic and charge-free region,

$$\begin{aligned}
\nabla \cdot (\mu_0 \mathbf{H}) &= 0 \\
\nabla \cdot (\varepsilon \mathbf{E}) &= 0 \\
\nabla \times \mathbf{E} &= -\mu_0 \partial_t \mathbf{H} \\
\nabla \times \mathbf{H} &= \varepsilon \partial_t \mathbf{E} + \mathbf{J}
\end{aligned} \tag{1.1}$$

where $\mathbf{E}$ and $\mathbf{H}$ are the electric and magnetic vector fields, ε and μ_0 are permittivity and vacuum permeability, and $\mathbf{J}$ is the current density. This leads to the electromagnetic wave equation

$$\overline{\overline{\varepsilon_r}}^{-1} \nabla \times \nabla \times \mathbf{E} = k_0^2 \mathbf{E} \tag{1.2}$$

where $\overline{\overline{\varepsilon_r}}$ is the relative permittivity tensor of the structure and k_0 is the vacuum wavenumber. Equation 1.2 is an eigenvalue problem, with each solution being an eigenmode of the system. The eigenvector $\mathbf{E}$ describes the electric field distribution of each eigenmode, and the square root of the corresponding eigenvalue $k_0 = \omega/c$ gives the ratio between the eigenfrequency and speed of light in vacuum c. Integrated photonic devices are often designed to have optical power in a finite and small number of guided modes, making eigenmode based analysis a powerful tool for understanding and engineering the behavior of different structures.

The two most basic photonic structures, rectangular waveguide and ring resonator, both have a cross-section which is invariant in one dimension, making it possible to reduce three dimensional problems to 2D. Coupled mode theory (CMT) can be used to perturbatively model a variety of compound photonic structures, that consist of a collection of such coupled elements or modified versions of them, based on eigenmodes of a single straight waveguide or ring resonator. In a non-absorbing structure, eigenmodes of the unperturbed system are orthogonal, and there is no transfer of power between modes. An index perturbation causes two originally orthogonal modes to couple, which results in two supermodes that are approximately solutions to the new system with the index perturbation. With this theoretical tool, one can engineer the spectral response as well as mode field profile of complex photonic structures based on eigenmodes of simple structures.

Commonly used numerical tools for designing integrated photonic devices include eigenmode and finite-difference time-domain (FDTD) solvers. Eigenmode solvers find the solutions to the electromagnetic wave equation (Eqn. 1.2). They can be implemented on a discrete grid, and are especially efficient for structures with a constant cross-section, where the problem can be reduced to 2D. FDTD solves Maxwell's equations (Eqns. 1.1) to propagate $\mathbf{E}$ and $\mathbf{H}$ fields in the time domain from a given excitation $\mathbf{J}$. Using a pulse excitation, a single FDTD simulation can provide the spectral response of a structure. Combined with information on the eigenmode fields of each port from a mode solver, an FDTD simulation provides the full scattering matrix of a multiport photonic component across a range of wavelengths.

1.2 Chip-scale Acoustic and Optomechanical Devices

Mechanical motion in solid material has been studied for centuries since even before Robert Hooke published what later became known as Hooke's law in 1678 and Sir Isaac Newton formulated the laws of motion in 1687. Much similar to electromagnetic waves, mechanical motion in elastic solids can be described by waves, where associated energy is transferred in space without transport of mass in the medium. Mathematically, the acoustic wave equation can be derived from Hooke's law and Newton's 2nd law, which together yield [5]

$$\nabla \cdot \bar{\bar{c}} : \nabla_s \mathbf{v} = \rho \partial_t^2 \mathbf{v} - \partial_t \mathbf{F} \tag{1.3}$$

where $\bar{\bar{c}}$ is the material stiffness tensor, $\mathbf{v}$ is the velocity field, and $\mathbf{F}$ is the force density. Different areas of research study the elastic wave equation to understand mechanical motion in solid structures on drastically different scales. Seismologists study earthquakes by extracting information from the propagation of elastic (seismic) waves of different polarizations through the earth [12]. Optical researchers study the interaction between mechanical vibration and guided optical modes through stimulated Brillouin scattering (SBS) in optical fibers [39]. On chip scale, surface acoustic wave (SAW) and bulk acoustic wave (BAW) devices are integrated with electronics to provide sensing and signal processing capabilities [18].

Optomechanics is an emerging field of research that studies the interaction between light and mechanical motion, and has captured much attention over the past decade [4, 47]. Optical fields produce force through two different mechanisms: radiation pressure results from the change in photon momentum from scattering at material interfaces, and electrostriction is a consequence of the dependence of material refractive index on strain. In wavelength-scale structures, the magnitude and distribution of these forces can be engineered through design [80]. To have efficient interaction, both optical and mechanical (acoustic) fields need to be localized. Nearly all existing resonator-based optomechanical systems use suspended structures [10, 99, 107], so the air-solid interface naturally terminates and confines acoustic waves within the scope of solid mechanics. Optomechanical interaction in integrated waveguides through SBS has recently explored simultaneous evanescent confinement of optical and acoustic fields in silicon/chalcogenide waveguides [66]. It is of interest to further explore evanescent guiding of acoustic waves in silicon-based integrated platforms, for optomechanics and potentially for building integrated "phononic circuits" as well.

In photonic waveguides, evanescent confinement is achieved between two materials with different optical refractive indices – scattering at material interface requires conservation of tangential momentum, and when this requirement forces the normal component of the propagation constant to become imaginary for waves going from a high index material into a low index material, total internal reflection occurs and light becomes confined in the high index material. For scattering of acoustic waves, the same is true, that the tangential component of the wavevector needs to be conserved, and two materials with different acoustic wave speed can provide evanescent confinement of acoustic waves. (There is no vacuum speed of sound, so acoustic refractive index isn't universally defined. But since optical refractive index is equal to the ratio between the speed of light in vacuum and the speed of light in that material, refractive index contrast is equivalent to slowness contrast). Silicon and silicon dioxide have a high contrast in acoustic wave speeds, which means it would have the same benefits of high index contrast photonic systems – that fields can be tightly confined to allow sharp bends and high-density integration of devices.

1.3 Outline of Thesis

In this thesis, several topics in integrated silicon-based photonics, acoustics and optomechanics are studied. Theoretical analysis, numerical design and calculations, and in some cases experimental demonstration are included.

Chapter 2 describes loss avoidance in contacted photonic structures using imaginary (radiative) coupling of modes. The principle of operation is explained, and two different types of devices are designed based on the same concept: a low-loss waveguide crossing array and a high-Q "wiggler" resonator. Both devices are fabricated and experimentally measured. Post-processing techniques developed to further suspend "wiggler" resonators are described, and high-Q air-suspended devices are demonstrated.

Chapter 3 investigates the feasibility of building acoustic devices on a silicon chip using evanescent confinement without requiring suspension. The confinement mechanism is explained in the context of a silicon, silicon dioxide and silicon nitride material system typical in CMOS technology. Example waveguide geometries are proposed and simulated. Material intrinsic and radiation losses are discussed and calculated. Acoustic components for dense "phononic" circuits that are counterparts of common photonic structures are simulated and discussed.

Chapter 4 explores the integration of optomechanical devices in CMOS platforms. Optimization of static radiation pressure in a vertically coupled dual ring resonator structure through waveguide dimension design is presented. Initial design of an optomechanical "wiggler" resonator is also discussed. A process flow for substrate removal to prevent optical leakage, and for subsequent device suspension is proposed, with current progress discussed.

In addition, Appendix A presents the implementation of a 3D finite-difference eigenmode solver. Construction of the discrete operator matrix is described, and results of test cases are shown. Appendix B presents details of fabrication methods developed and used, including suspension of "wiggler" resonators in a silicon-on-insulator (SOI) process, and substrate removal for CMOS chips.

Chapter 2

Loss Avoidance in Contacted Photonic Structures

2.1 Motivation

Photonic structures with contracts have important applications in integrated photonics. The addition of contacts to linear waveguides and resonant devices can enable waveguide crossings for dense planar photonic circuit integration [55], provide access for electrical and thermal modulation of guided light [90] as an alternative to ridge waveguide based designs which require a partial etch in the fabrication process [79], and facilitate suspension of photonic structures for various purposes, where these contacts can directly connect the suspended structures to the rest of the chip to provide mechanical support [53].

Without special design, adding contacts to a waveguide or a resonator can introduce a strong index perturbation to the original structure, causing the guided optical fields to scatter. In the waveguide case, this would cause reflection and propagation loss issues, as well as strong crosstalk in the case of a waveguide crossing array, where the contacts are also individual waveguides. In whispering gallery mode based resonators, since the optical mode fields are concentrated on the outer circumference, pedestals [46] and inner contacts [99, 106] can be relatively easily placed, as long as they are far enough from the fields, to permit structure suspension. The ability to attach contacts on the outer circumference of a resonator brings additional and unique benefits, such as enforcing a designed coupling gap even with the presence of built-in material stress, but would normally substantially degrade the quality factor of the resonator [88, 113].

In this Chapter, a general approach is proposed to study and design contacted photonic structures with low scattering loss based on imaginary coupling of modes. In Section 2.2, the general theoretical concept of avoiding scattering loss through imaginary coupling of modes will be described. Contacts are treated as periodic imaginary index perturbation to the original waveguide or resonator structure, and their locations of placement are designed to efficiently couple specific eigenmodes of the unperturbed structure, in order to construct a pair of supermodes maximally split in imaginary propagation constant β or resonant frequency ω. Between these two supermodes, the one with the smaller imaginary component in complex β (spatial decay rate) or ω (temporal decay rate) would correspond to a field profile that spatially avoids the contacts, thus minimizing scattering loss. Using the same fundamental concept, two different types of geometries will be presented. In Section 2.2, the construction of a waveguide crossing array consisting of a straight waveguide with linearly periodic contacts will be presented. In Section 2.4, the design and implementation of a circular version of the same concept, a ring resonator with azimuthally periodic contacts, will be introduced. Both devices are designed, fabricated and experimentally measured, showing that this type of structures can be further tailored to suit a wide range of applications in optical communication, electro- and thermo-optics and optomechanics.

2.2 Loss Avoidance Through Imaginary Coupling of Modes

Photonic structures with contacts can take a variety of geometric forms. Figure 2.2.1 shows three special cases: straight waveguides with symmetric/staggered (inversion symmetric) linearly periodic contacts on the two sides of the waveguide, and a ring resonator with staggered azimuthally periodic contacts on the inner and outer circumferences. Each of these geometries can be studied and designed using coupling of modes, by identifying the waveguide or resonator without contacts as the unperturbed structure, and treating the contacts as a periodic index (or boundary wall) perturbation.

The modes of the contacted waveguide as shown in Fig. 2.2.1a, for instance, can be expanded in the basis of the eigenmodes of a continuously z invariant straight waveguide, with z dependent expansion coefficients determined by coupling between modes induced by scattering from the periodic (discrete translational symmetry) contacts. Moreover, since the entire structure is periodic, there exist Bloch mode eigenstates that can propagate along the structure without substantially scattering off the contacts.

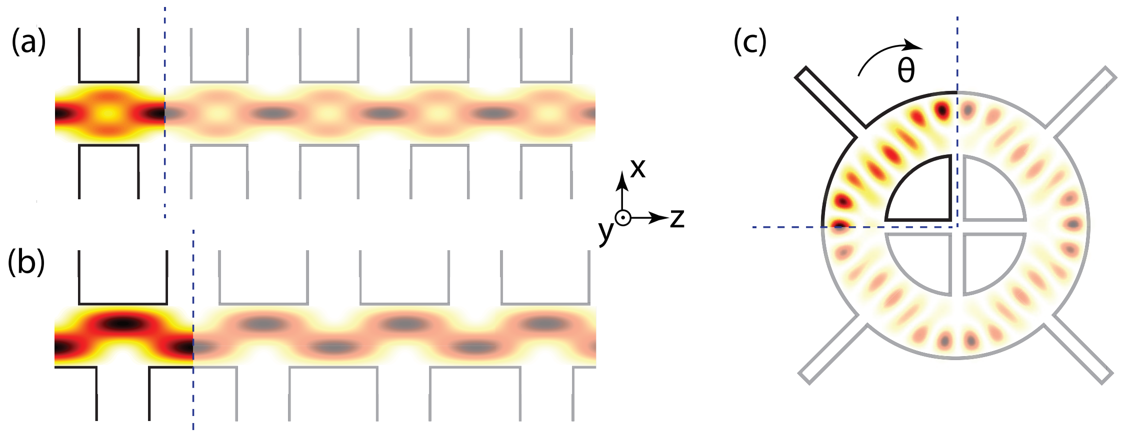

Figure 2.2.1: Photonic structures with periodic contacts: (a) straight waveguide with symmetric and linearly periodic contacts on two sides; (b) straight waveguide with staggered and linearly periodic contacts on two sides; (c) ring resonator with radially staggered and azimuthally periodic contacts on inner and outer circumferences.

Consider an unperturbed straight waveguide with a width that supports only the first three TE modes. Because of structural symmetry, potential coupling between guided TE modes is nonzero only between the first and third order modes, which both have the same symmetry with respect to the y-z plane. The Bloch supermode can therefore be expanded as

$$\mathbf{e}_B(x,y,z) = a_1(z)\mathbf{e}_1(x,y) + a_3(z)\mathbf{e}_3(x,y) \tag{2.1}$$

where $\mathbf{e}_m(x,y)e^{-i\beta_m z}$ is the normalized mth order TE eigenmode of the unperturbed straight waveguide with propagation constant β_m, and a_m is the corresponding z dependent expansion coefficient with

$$\frac{d}{dz}a_m = -i\beta_m a_m - i\sum_{m,n=1,3}\kappa_{mn}e^{i(\beta_n-\beta_m)z}a_n \tag{2.2}$$

and κ_{mn} is the coupling coefficient between unperturbed modes $\mathbf{e}_m$ and $\mathbf{e}_n$ [103]

$$\kappa_{mn} = \frac{\omega\varepsilon_0}{4}\iint \delta n^2(\mathbf{e}_{Tm}\mathbf{e}_{Tn} - \frac{n^2}{n^2+\delta n^2}e_{zm}e_{zn})dS \tag{2.3}$$

where $\mathbf{e}_{Tm}$ and e_{zm} are the transverse and longitudinal components of $\mathbf{e}_m = \mathbf{e}_{Tm} + \hat{z}e_{zm}$. To efficiently couple between the 1st and 3rd order unperturbed TE modes, the index perturbation from the contacts must have a strong Fourier component that is matched to $\beta_1 - \beta_3$ (the simplest possibility being for the contacts to have a period $\Lambda = \frac{2\pi}{\beta_1 - \beta_3}$). The same index perturbation also couples both unperturbed guided modes to phase matched radiation modes, and this leads to an additional, radiation facilitated coupling between the two guided modes, which differs from the reactive coupling directly between the two guided modes.

A toy-model problem to consider, for optimizing the placements of the contacts to construct a low-loss Bloch mode, is the same geometrical structure, but with an absorbing imaginary term added to make the refractive index of the contacts complex, such that the unperturbed 1st and 3rd order TE modes are absorbed at the contacts, rather than being scattered into radiation (Fig. 2.2.2). In this new system, we can now consider the resulting supermodes from direct coupling between only the two guided modes due to a complex periodic index perturbation, without having to calculate coupling between the guided modes and a continuum of radiation modes. We use this simple system as a heuristic for the actual system with radiation loss. The coupling coefficient given by Eqn. 2.3 becomes complex, and the coupled mode equation Eqn. 2.2 leads to two supermodes with propagation constants that are split in both real and imaginary parts, between which the one with the smaller imaginary part corresponds to lower scattering loss. To obtain the actual low-loss Bloch mode, $a_1(z)$ and $a_3(z)$ can be solved for specifying the Bloch-Floquet boundary condition on a unit cell of the periodic structure and solving for the (leaky mode) band structure numerically.

A similar analysis applies to a straight waveguide perturbed by a periodic and antisymmetric array of contacts such as the one depicted in Fig. 2.2.1b. Here the 1st and 2nd order TE modes of the unperturbed waveguide can be coupled using an array of contacts with a period $\Lambda = \frac{2\pi}{\beta_1 - \beta_2}$, and the constructed low-loss Bloch mode would have a wiggling intensity field that "avoids" the scattering points. In a circular resonator with contacts on the inner and outer circumferences (Fig. 2.2.1c), two unperturbed degenerate ring modes with different radial and azimuthal orders can be coupled to create a circular version of the wiggling field pattern, and phase matching requires

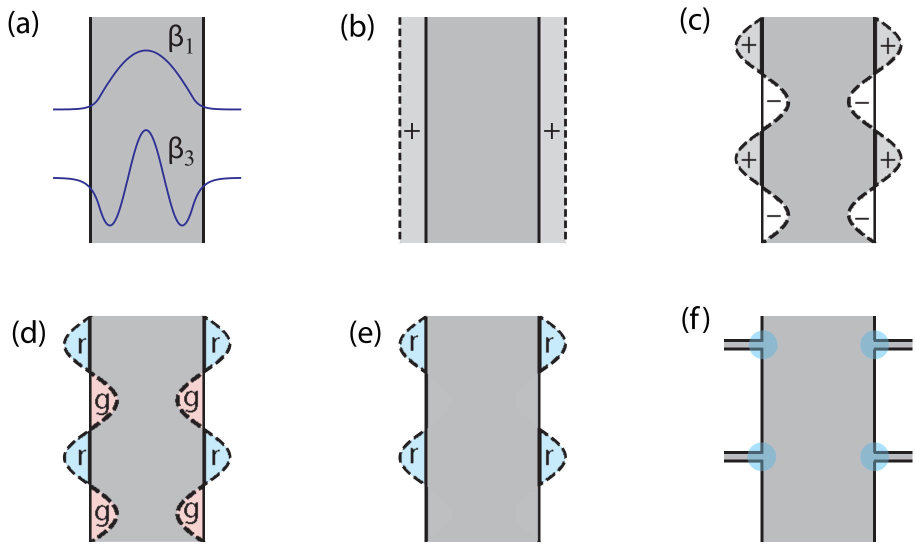

Figure 2.2.2: Coupling two waveguide modes through index perturbation. (a) 1st and 3rd order TE modes of an unperturbed straight waveguide with propagation constants β_1 and β_3. (b) A constant symmetric index perturbation gives zero coupling phase-matching is not satisfied. (c) Waveguide width modulation (real index perturbation) with period $\Lambda = 2\pi/(\beta_1 - \beta_3)$ couples modes 1 and 3 and leads to a real splitting in the propagation constants of the resulting supermodes. (d) Material gain (g) and loss (r) modulation (imaginary index perturbation) with the same spatial period leads to a complex splitting in β, with the imaginary part representing spatial decay rate. (e) Half of the imaginary grating in (d) with only loss and no gain still leads to a complex splitting in β. (f) Effects of phase-matched contacts can be heuristically understood as a periodic, scattering loss induced imaginary grating.

that the number of the periodic contacts must match the difference in azimuthal mode orders of the two unperturbed ring modes.

2.3 Monolithic Broadband Waveguide Crossing Array

An important application of a linear symmetric contacted waveguide (Fig. 2.2.1a) is a waveguide crossing array, a device that allows waveguides to physically cross each other while keeping optical energy in the same waveguide mode. Silicon photonics is beginning to enable complex on-chip optical networks comprising hundreds of devices. With increasing device density and complexity in a planar photonic circuit, efficient waveguide crossings are indispensible in many network topologies. For some network topologies, the number of waveguide crossings required rises quickly with circuit size and tolerable levels of loss and crosstalk per crossing accordingly drop to very small limits [11]. A multitude of work has considered crossing designs over the past decade. Crossing designs based on adiabatic aperture widening are large [13, 28, 105], while resonant designs permit low loss and crosstalk in a compact footprint, but have narrow bandwidth [61] (e.g. $\sim$4 nm [114]). Multilayer processes allow reduced scattering in crossing waveguides [14] or their complete isolation through vertical displacement [42], but they require multiple lithographic steps and/or material layers, and in the latter case may require interlayer couplers with additional loss and footprint penalties. Multimode-interference (MMI) based crossings [21, 52, 74, 75, 97, 116], despite ostensibly multimode behavior, have a number of attractive features, with individual crossings down to 0.18 dB loss and 41 dB crosstalk [116].

Here we describe ultra-low-loss waveguide crossing arrays based on a periodic multimode structure. Popović *et al.* [75] proposed an efficient approach to design a crossing array (Fig. 2.3.1) by constructing a low-loss Bloch wave in a matched periodic structure where the optical field synthesizes periodic focii that jump across gaps and avoid diffraction loss and scattering at the crossing points, and where non-adiabatic tapered excitation structures are used to efficiently excite these low-loss Bloch waves. This concept is reminiscent of periodic lens-array microwave beam guiding [31]. Microphotonic implementations use a minimum of modes to implement focusing physics, eliminate reflections, and introduce new degrees of freedom. In the first experimental demonstration of this concept [54], we showed record low waveguide-crossing loss of 0.04 dB/crossing (0.9%), equal to theoretical design efficiency [75], demonstrating the robustness of these structures. Another recent paper [115] demonstrated similar crossing arrays which achieved 0.14 dB loss, based on our proposal in Ref. [75], and introduced an improvement based on subwavelength patterning of the sidewalls, reducing the loss further to below 0.02 dB. To our knowledge, these two results represent respectively the lowest achieved crossing loss in CMOS-compatible photolithography processes [54] and in high-resolution processes allowing nanopatterning, such as scanning electron-beam lithography [115].

In this Section, we present the low-loss unidirectional Bloch mode concept, its use in design of waveguide crossing arrays, and our experimental results on record loss in CMOS-compatible crossings. We show an excellent match between theory and experiment.

2.3.1 Design of Linearly Periodic Contacts

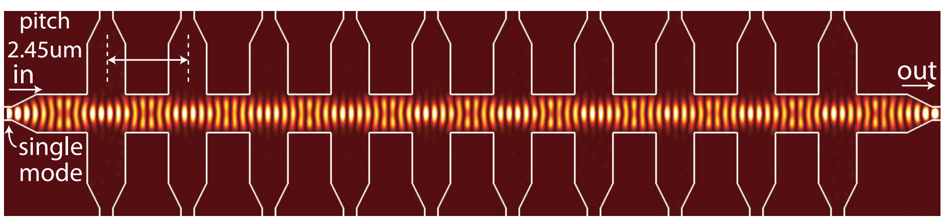

Figure 2.3.1: Ultra-low-loss waveguide crossing array, based on excitation of a low-loss breathing Bloch wave, formed of 1st and 3rd modes of a multimode waveguide (2D FDTD simulation) [75]. The mode is stabilized by radiative loss.

The basic concept is similar to MMI-based [21, 52] synthesis of fields that focus across a waveguide crossing region [97] to prevent diffraction loss, extended to an open-system periodic array. The periodicity gives rise to a unique, novel type of Bloch wave formed from two forward propagating modes of different transverse spatial order, which we can refer to as a unidirectional Bloch wave (Fig. 2.3.2). This kind of Bloch wave is formed of a superposition of the fundamental and third-order mode in a multimode waveguide, where a periodic perturbation (in this case the crossing

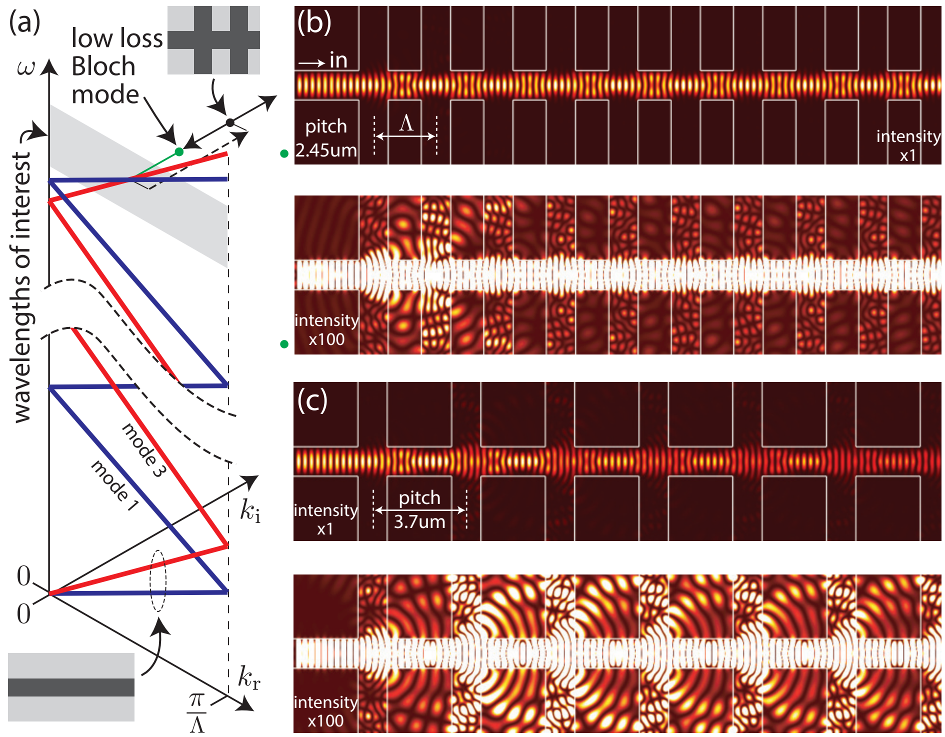

Figure 2.3.2: Unidirectional low-loss Bloch modes: (a) illustration of complex-k band structure of unperturbed waveguide and imaginary-k splitting due to radiative crossings; (b) low-loss breathing field due to matching periodicities of the structure and of the breathing optical field [2D FDTD; bottom: 100x oversaturated intensity to show detail, green dot in a] [75]; (c) high propagation loss with mismatched structure and breathing mode periodicities.

waveguides) provides coupling between the two modes and leads to an anticrossing. This Bloch wave differs from typical Bloch waves formed in photonic crystals by periodic coupling in that the half-wave periodicity of the PhC structure leads to bandgaps at the edges of the Brillouin zone, formed by an anticrossing between the dispersion curves of a forward and a backward guided mode. In the present case, the periodicity leads to an anticrossing of a high order, between forward fundamental and third-order modes, which can be anywhere within the Brillouin zone [Fig. 2.3.2a]. In this sense, the crossing array is more analogous to a long-period (fiber) grating than a photonic crystal. The typical Brillouin-zone edge bandgap that is the key characteristic of photonic crystals will be primarily absent in these structures because they have nearly no periodicity-induced reflection.

The band structure is unusual in a second way. The coupling at the waveguide-crossing points is not (only) a standard reactive, i.e. power-exchange, coupling that results from index perturbations, but includes radiative interference coupling that scatters light from both the 1^{st} and 3^{rd} order transverse modes, leading to imaginary k-splitting. When this scattering interferes destructively, a low radiation loss eigenstate is established. This means there is a propagation constant splitting that is not real, but imaginary (or, more generally complex when the standard index perturbation part is also accounted), and leads to one Bloch mode with a low imaginary part of the complex propagation constant (low loss), and another with a high loss. There are analogous frequency eigenstates in resonators based on similar physics [23, 29].

Physically, the low-loss Bloch mode corresponds to a superposition of modes 1 and 3 of the unperturbed waveguide with the right ratio of amplitudes to produce a field minimum (or null) at the scattering points. The high-loss mode in turn has constructive interference at these points. The unique insight is that the complex-propagation-constant eigenstates of the periodic structure uniquely select the field distribution with a high and low scattering loss. Then, to realize a low-loss crossing array, the objective is to choose the waveguide cross-sectional dimensions, and crossing periodicity, that minimize the loss of the lower loss Bloch mode. This insight also applies to the design of single crossings [52, 74, 116] and should be the first step their design.

To arrive at a low-loss Bloch mode, our strategy is to maximize the imaginary splitting of the propagation constants for a **given** scatterer geometry. Radiation loss through scattering provides an imaginary part to the propagation constants [dashed arrow, Fig. 2.3.2a], while radiative splitting brings back the low-loss mode down to as close to zero loss as the geometry permits via radiative cancellation [split arrows, Fig. 2.3.2a]. As with real splitting, for a given perturbation, the maximum splitting occurs at the phase matching condition. In the case of degenerate modes, a perturbation uniform along the waveguide suffices. Since in our structure modes 1 and 3 differ in propagation constant, a periodic perturbation that matches this difference is required, and leads to the optimal periodicity of the array. Hence, to excite a low-loss breathing mode, the period of the crossing array is designed to first order to match the difference in (effective) propagation constants of the 1^{st}- and 3^{rd}-order eigenmodes of the waveguide, $\Lambda = 2\pi/(\beta_1 - \beta_3)$. Since β_1 and β_3 are eigenstates of the unperturbed waveguide without crossings, rigorous simulations that account for self-coupling perturbations [76] in the crossings lead to a small correction to the periodicity in the actual design.

2.3.2 Excitation of the Low-loss Mode

If the fundamental mode is launched into the multimode guide [Fig. 2.3.2b], the first few crossings strongly scatter until the low-loss wave is established. The incident mode 1 field can be thought of as a superposition of the low-loss and high-loss Bloch waves with mode 1 components adding and mode 3 components canceling. As the high-loss Bloch mode decays with a fast decay rate, only the low loss, breathing mode remains. We can observe the fraction of mode 1 and 3 present in a cross-section where the low-loss wave has converged to a steady state. If this ratio of modes 1 and 3 is excited at the start of the structure in Fig. 2.3.2b (as is done in Fig. 2.3.1), no power needs to be initially coupled to the high-loss Bloch wave, and thus no scattering will occur at the first few crossing points.

For efficient excitation of the low-loss Bloch wave from a single mode waveguide, we employ a symmetric, non-adiabatic taper. It acts as a "directional coupler" between modes 1 and 3 of the multimode guide [52, 74, 75] (by symmetry there is no coupling to asymmetric mode 2). Another approach, MMI excitation at an abrupt junction [21], is equivalent to our non-adiabatic taper design in the (non-optimal) limit of zero taper length.

2.3.3 Experimental Demonstration

Devices for experimental demonstration were designed to be implemented in the 220 nm silicon device layer ($n = 3.476$ at 1550 nm wavelength) of a standard silicon photonics silicon-on-insulator (SOI) platform with a 2 μm oxide undercladding, and oxide overcladding ($n = 1.45$). The width is chosen to sufficiently confine the first and third modes, without admitting a 5^{th} mode. Dimensions are given in Fig. 2.3.3c, with the period obtained from a parameter sweep in 3D FDTD simulations to provide the minimum loss per crossing.

A non-adiabatic taper can be designed to excite the optimum ratio of 1^{st} and 3^{rd} eigenmodes from a single-mode waveguide input to minimize loss. This ensures that only the low-loss Bloch

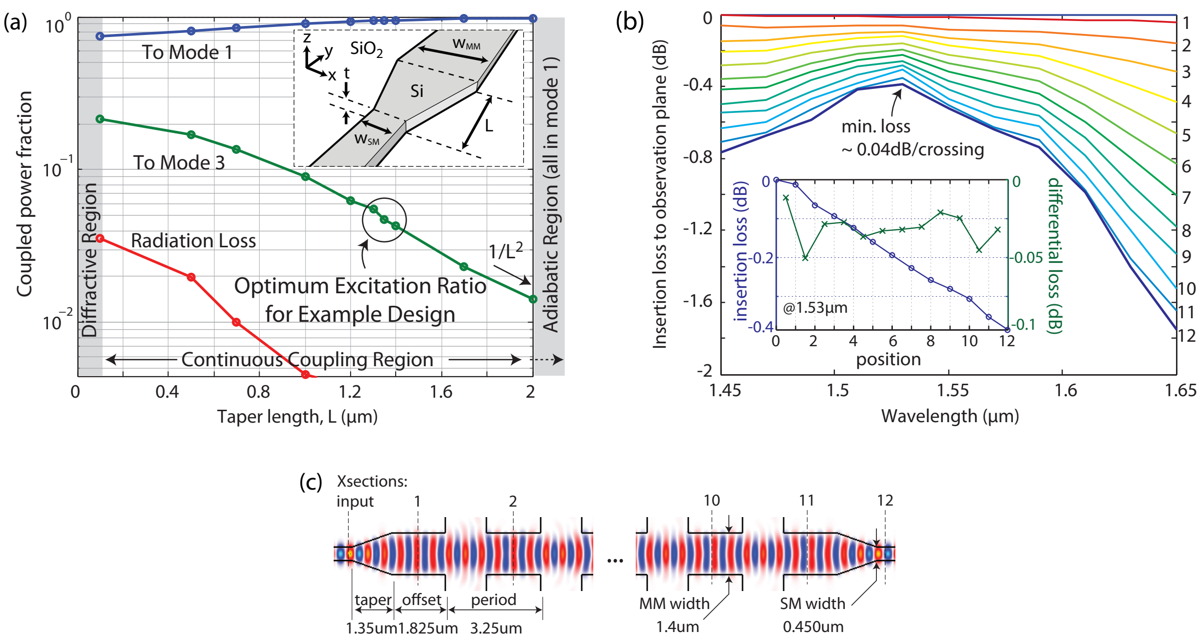

Figure 2.3.3: Crossing design: (a) short, non-adiabatic symmetric taper as a directional coupler between the 1st- and 3rd-order modes, allowing efficient excitation of a breathing Bloch mode of the crossing array; coupling and loss vs. length. (b) Simulated transmission after 1-10 crossings, and through entire structure including tapers (3D FDTD). (c) Field from a monochromatic 3D FDTD simulation at 1550 nm.

wave is excited. Figure 2.3.3a shows 3D FDTD simulations of a linear taper design, showing coupling to mode 3, and corresponding radiative loss. For an optimum mode 3 coupling ratio of just under 5%, a 1.35 μm taper suffices, and the radiation loss is negligible (<0.4%) so we didn't consider more complex taper shapes here. In general, tapers that gradually rather than abruptly couple modes 1 and 3, i.e. distribute coupling along the taper can minimize coupling to radiation modes. The taper in Fig. 2.3.3a is broadband, with 4.75% coupling at 1550 nm, a 0.3% variation over 1450–1550 nm, increasing to 6% at 1650nm.

Figure 2.3.3b shows the simulated transmission spectra of a complete waveguide crossing array with 10 crossings and input/output tapers to 450 nm-wide, single mode waveguides. The insertion loss vs. wavelength is computed after 1–10 crossings, with observation planes labeled in Figs. 2.3.3b (right) and 2.3.3c, and through the entire structure including tapers, using 3D FDTD. Peak theoretical transmission is $\sim$ 0.4 dB for 10 crossings and two tapers, and $\sim$0.033 dB average per added crossing (Fig. 2.3.3b inset). Figure 2.3.3c shows the transverse electric field distribution in the structure designed to excite the low-loss Bloch wave with a monochromatic 1550 nm source in the fundamental mode of the input waveguide. The input taper must be placed at a particular offset from the first crossing in order for the first "focal point" of the field envelope to coincide with the first crossing waveguide. This is found from the relative phases of the two modes exiting the taper, and the beat length necessary to arrive at the relative phase of the low-loss Bloch wave's focal point.

Arrays with $N = 10, 50, 150$ and 250 crossings were realized. Fig. 2.3.4a shows a subset of the on-chip devices, fabricated through the ePIXfab multiproject wafer service [45]. To pre-compensate for bias in the lithography, the width of the multimode waveguide section was varied in layout from 1450 nm to 1510 nm, with other dimensions remaining at design target (Fig. 2.3.3c). Figures 2.3.4b and 2.3.4c show scanning electron micrographs (SEMs) of a Bloch-wave 10-crossing array and a "normal" 10-crossing array based on 450 nm-wide single mode waveguides, respectively.

Figure 2.3.5a shows measured total insertion loss experimentally measured in these devices, normalized to a plain single mode waveguide of equal total length. Thus, input and output grating

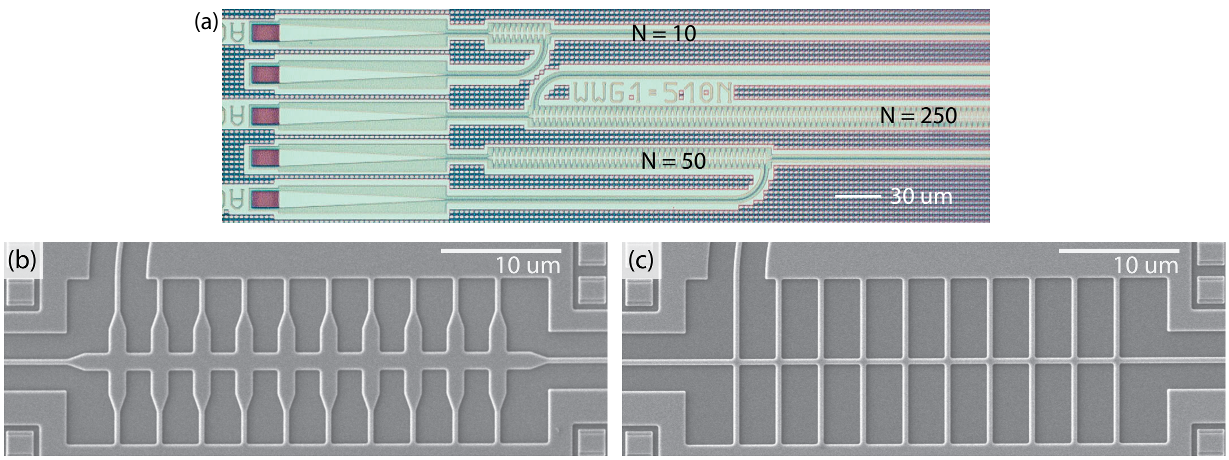

Figure 2.3.4: Fabricated crossing test structures. (a) Optical micrograph of on-chip crossing arrays fabricated through IMEC/ePIXfab [45] with 10, 250 and 50 periods. (b) SEM of a 10-period low-loss Bloch crossing array. (c) SEM of a 10-period normal crossing array.

coupler responses are normalized out of the spectra. The data represents the insertion loss of the array, including losses from the non-adiabatic tapers and the crossings, relative to a plain single mode waveguide. Here, insertion loss means the additional cost of replacing a single mode waveguide with the crossing array; hence, in principle, if there is substantial propagation loss due to sidewall roughness, by this definition it is possible for the insertion loss to be slightly negative, if the multimode waveguide has lower sidewall roughness loss, and the crossings are near lossless. For each waveguide width variant, the slope of insertion loss versus number of crossings gives the loss per crossing (not including the tapers) at each wavelength (linear fits, see Fig. 2.3.5a inset, give Fig. 2.3.5b). A device with waveguide width 1510 nm shows an average loss per crossing of 0.04 dB at $\lambda = 1505.8$ nm. The flatter loss slope of the last 100 crossings (Fig. 2.3.5a, inset) shows loss of 0.032 dB/crossing with $\sim\pm0.005$ dB uncertainty due to coupling (equivalent to $\sim$100 dB/cm distributed loss). SEMs of the 1510 nm wide structure (Fig. 2.3.4b) confirm that its measured width is near the targeted 1400 nm. The demonstrated loss of 0.04 dB/crossing matches theory closely, but the minimum loss wavelength is shifted down by about 25 nm. This is consistent with an error in device layer thickness/width. For small shifts, the minimum insertion loss is unchanged. The loss per crossing doubles for a width error of $\sim$50 nm (Fig. 2.3.5b), but the wavelength at which it occurs changes.

At the 250-crossing Bloch array's optimal wavelength (Fig. 2.3.6a), it has lower insertion loss than a 10-crossing single-mode array. Figure 2.3.6b shows the transmission and crosstalk of a 1510 nm-wide 10-crossing Bloch-wave design and a 10-crossing single-mode array. Apart from 13 dB higher transmission, approaching sub-1% loss per crossing, the Bloch-wave crossing array also suppresses crosstalk by at least 35 dB (limited by measurement noise), 20 dB more than a normal crossing array. This is consistent with the theoretical prediction [75].

The experimental demonstration of CMOS compatible waveguide crossing arrays with ultra-low losses, matching theory, may be enabling and impact photonic network-on-chip architecture. These structures offer capabilities for electrically/thermally active, suspended and optomechanical photonic structures with minimized scattering loss. More generally, this concept extends to higher

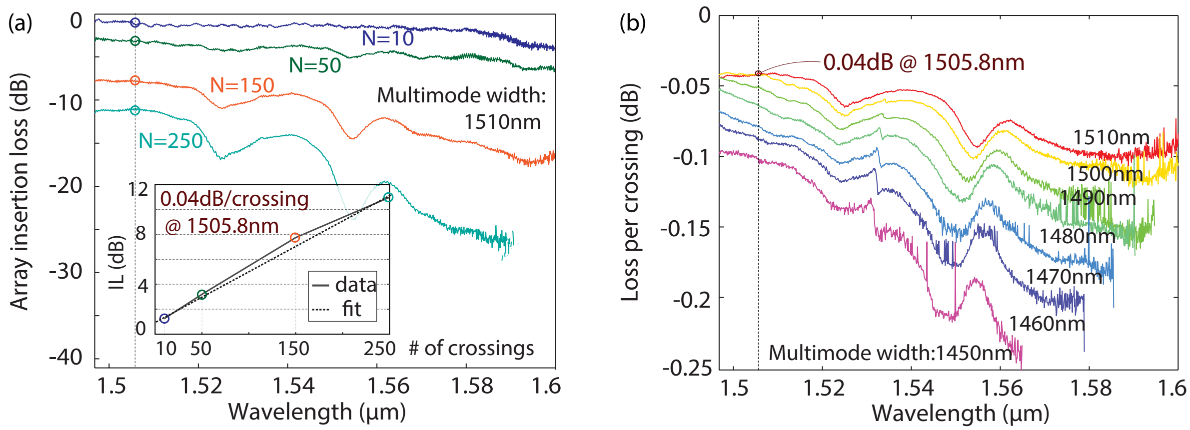

Figure 2.3.5: Experimental measurements. (a) Spectral insertion loss of Bloch arrays with 10, 50, 150 and 250 crossings (1510 nm width); (b) insertion loss/crossing vs. wavelength of crossing arrays with waveguide widths from 1450 nm to 1510 nm.

order, as well as transversely asymmetric structures [54, 74], as recently applied in modulators [90].

2.4 High-Q Wiggler Resonator

Microcavities with attachments such as the one illustrated in Fig. 2.2.1c have important applications in integrated photonics. Ridge waveguides extend a flange of the core into the cladding, permitting electrical contacts and good optical confinement to enable electro-optics modulators [113]. Suspended microcavities relying on pedestals [46] or inner spokes [99, 106] for mechanical support have been used in optomechanics. Many of these approaches have limitations: ridge waveguides require a partial etch step, not available for example in standard complementary metal-oxide semiconductor (CMOS) processes [72, 90] nor suitable for suspended structures. Pedestal and inner-spoke cavities either rely on disk-like whispering gallery modes and provide limited degrees of freedom for mechanical design, or have external contacts [88, 113] at the expense of substantial degradation in Q factor due to scattering.

Recently an approach has been proposed to design multimode linear waveguides and resonators with periodic attachments that support modes whose fields avoid those attachments so as to maintain low propagation loss [55, 75]. High-Q resonators based on linear, periodically contacted

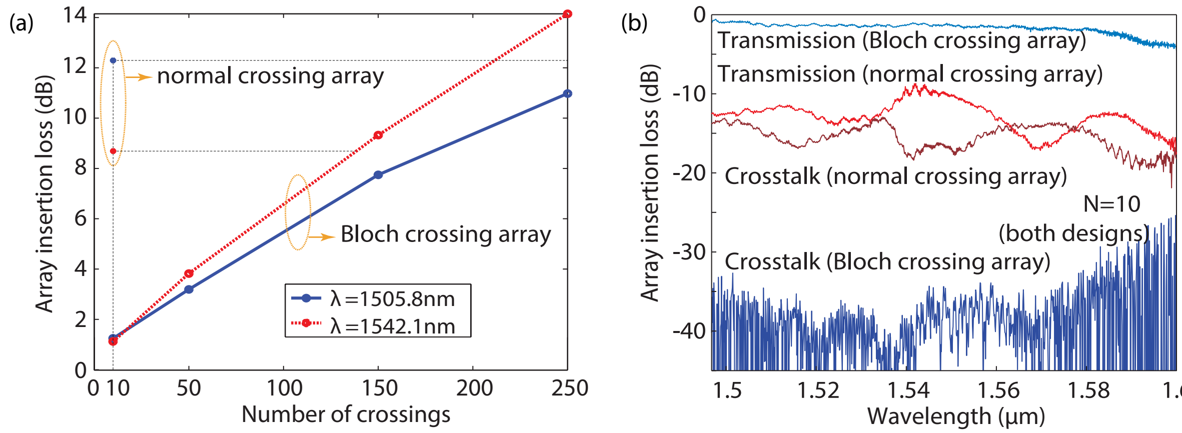

Figure 2.3.6: (a) Insertion loss vs. number of crossings in Bloch crossing array (width 1510 nm) and a 10-crossing normal array, at $\lambda = 1505.8$ nm where the Bloch crossing has the lowest loss and at $\lambda = 1542.1$ nm where the normal crossings have the lowest loss. (b) Transmission and crosstalk spectra of the Bloch and normal crossing arrays with 10 periods.

waveguides that support low-loss "wiggler modes" were recently demonstrated [89, 90]. However, these cavities are large and require non-adiabatic tapers for single-mode to wiggler-mode transitions that may limit their loss Q.

In this section, we demonstrate azimuthally periodic contacted ring microcavities comprising a multimode microring waveguide with periodic attachments to the inner and/or outer walls (Fig. 2.4.1a). These cavities implement a circular symmetry version of the structural Bloch matching and complex Q-splitting concept previously demonstrated in a non-resonant linear waveguide geometry [55, 89, 90]. As in the linear devices, the attachments act as perturbations that lead to a radiative coupling (as opposed to the usual reactive coupling between coupled structures) that splits the first and second fundamental radial eigenmodes (of different azimuthal order and initially degenerate) of the ring in **imaginary frequency**. This results in a "wiggler" supermode with a field whose spatial distribution avoids the scattering attachments that contact the core, preserving a high Q (Fig. 2.4.1b), and another one with high scattering loss at the contacts and thus low Q. In a mode coupling picture, the attachments add both a real and imaginary frequency shift to each mode, through each mode's self-coupling with the perturbation. The physics that results in the low-loss supermodes is a cross-coupling between the modes, mediated by the periodicity-matched perturbation, which provides imaginary frequency splitting and recovers most of the imaginary frequency shift (loss) introduced by the self-coupling term. This concept has many applications, allowing electrically and thermally contacted resonators with great freedom in contact geometry and reasonably high optical Q. Further releasing of the devices from the substrate enables thermal isolation and mechanical suspension, which may be useful for thermo-optic effects and thermal isolation design as well as tuning of mechanical properties and optomechanics (light-forces-based devices on chip). We experimentally demonstrate silicon-core ring microcavities that are silica cladded with $N = 6$ contacts to the core at the outer radius, and show a low-loss resonant supermode with a Q of $258,000$, and an air-suspended, smaller-radius ring with $N = 4$ contacts and a measured Q of $139,000$.

2.4.1 Design of Circularly Periodic Contacts

To construct a contacted ring resonator that supports a high-Q "wiggler" supermode, we start with a single ring that has resonant modes with first- and second-order radial fields. Interference between these two modes allows the resulting supermode to have a field intensity pattern that wiggles back and forth between the inner and outer walls along the ring (Fig. 2.4.1b), with a periodicity determined by the difference in azimuthal mode orders. If an array of contacts is then introduced to the ring, the resulting scattering loss at the contact points can be seen as a perturbation of imaginary permittivity to the original structure, which couples and splits the two modes in imaginary (and real) eigenfrequency (or equivalently in loss Q). As in real splitting, the coupling is maximized when the phase matching condition is met, i.e. when the periodicity of the contact array equals the difference in azimuthal mode numbers of the first- and seconds-order radial modes. This loss avoidance behavior of the high-Q "wiggler" mode can be understood as the excitation of the right relative amplitudes of the first-order and second-order radial resonant modes of a ring to produce a null in the beat pattern (spatial envelope) of the total electric field at the contact points. Note, however, that the "wiggler" supermode is an eigenstate rather than a

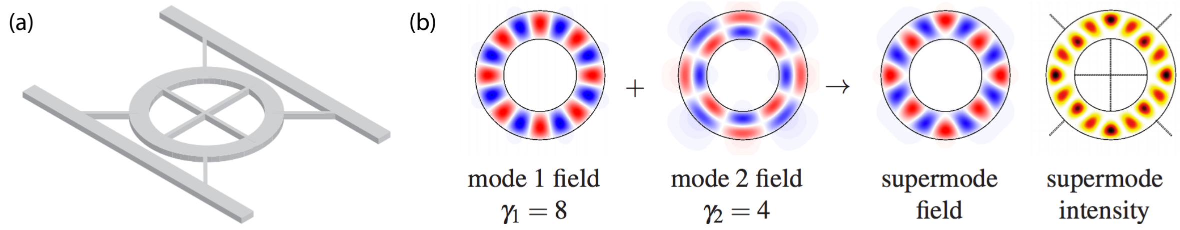

Figure 2.4.1: (a) Illustration of proposed microcavity with azimuthally periodic contacts. (b) Two degenerate-frequency eigenmodes of an unperturbed ring (1^{st}-order radial mode with azimuthal mode number $\gamma_1 = 8$, and 2^{nd}-order radial mode with $\gamma_2 = 4$). A superposition of these modes, which form a low-loss supermode under the scattering perturbation, has a vanishing field intensity at the contact points.

superposition of multiple modes in the perturbed system with contacts, and a standard single-mode waveguide coupler suffices to excite this mode.

For experimental demonstration, microcavities were designed in a 220 nm-thick silicon device layer of typical custom silicon-on-insulator (SOI) wafers for photonics [45]. Figure 2.4.2a plots the azimuthal mode numbers of the first-order radial mode (γ_1, blue dashed lines), and the difference between azimuthal mode numbers ($\gamma_1 - \gamma_2$, red solid lines) of the first and second radial modes in an unperturbed ring cavity without contacts. At crossing points of the red and blue contours, γ_1 and γ_2 are integers and both radial modes are resonant at the design wavelength of 1550 nm. Bending loss further restricts the dimensions at which high-Q modes can be obtained. Requiring high-Q initial (uncoupled) modes limits the design space to the upper right part of Fig. 2.4.2a, for example beyond contours of constant bending loss Q of 10^5 or 10^6, given as examples in the figure. The orange marker shows an example design, with $\gamma_1 = 32$, $\gamma_2 = 26$, and the bend-loss Q of the second mode without attachments just above 10^6.

An azimuthally periodic array of contacts is then introduced, with periodicity equal to the beat length between the two degenerate modes – the number of attachment periods is equal to the difference in azimuthal orders of the two modes ($N = \gamma_1 - \gamma_2 = 6$). These attachments force the resonator into radiative splitting along the imaginary axis on the complex frequency plane (Fig. 2.4.2b, left). This is in contrast to direct reactive coupling of resonators, which leads to real

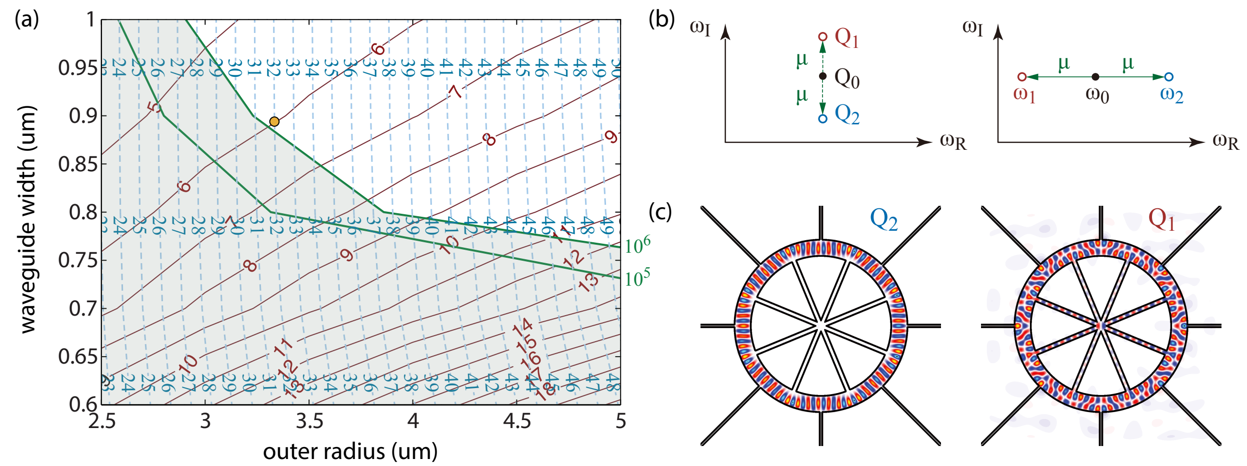

Figure 2.4.2: (a) Azimuthal mode number (γ_1) of 1st order radial mode of an unperturbed ring at 1550 nm (blue, dashed), difference between azimuthal mode numbers of 1st and 2nd order radial modes ($\gamma_1 - \gamma_2$, red), and bending loss Q of the 2$^{\text{nd}}$ radial mode (green, thick) versus ring width and outer radius. (b) Imaginary (left) and real (right) splitting of initially degenerate modes. (c) High-Q (left) and low-Q (right) supermode fields resulting from radiative coupling by ring attachments.

frequency splitting (Fig. 2.4.2b, right). Since quality factor is related to the imaginary part of the complex resonant frequency [$Q \equiv \omega_R/(2\omega_I)$], the imaginary splitting leads to a high-Q supermode whose field distribution spatially avoids the scattering contacts (illustrated in Fig. 2.4.2c, left), and a complementary low-Q supermode whose field distribution has strong overlap with the contacts (Fig. 2.4.2c, right).

2.4.2 Experimental Demonstration

Figure 2.4.3a shows an optical micrograph of a fabricated device with $N = 6$ contacts attached to the outer wall of the resonator. An array of devices was designed around the optimum parameters to account for fabrication variations and to show that a particular combination of radius and width is required for high-Q operation. The best-performing device was designed with a target outer radius of 3.89 μm, (multimode) ring cross-section of 990×220 nm, and contact width of 100 nm. For this device, Fig. 2.4.3b shows the highest measured Q factor of $258,000$. The observed resonance doublet is a result of the typical splitting of high-Q traveling-wave modes due to contra-directional coupling (note that here four modes are near-degenerate prior to inclusion of the attachments). In this case, a lack of azimuthal invariance of the structure contributes enhanced contra-directional coupling. Note that the drop port is over 15 dB beneath the through port transmission, which means that the total Q is dominated by the cavity loss Q, not the external coupling [73]. While the highest observed Q was 258k, many devices with a loss Q over 100k were measured.

Evidence that the thin contacts visible in Fig. 2.4.3a are not inconsequential, i.e. that our design approach is necessary to obtain high Q, is provided in Fig. 2.4.3c. The figure shows drop-port spectra of representative devices with a fixed waveguide-cavity coupling gap (250 nm) and radius ($R_{\text{center}} = 3.4\,\mu$m), while the width is linearly varied (see Fig. 2.4.3c). The resonances red-shift with increased width due to increase in effective index. However, the transmission and the Q increase (linewidth decreases) as one approaches the center device from either side. These both confirm that the highest loss Q is in the central device, as the waveguide coupling is broadband and does not contribute to variation in insertion loss from one resonance to the next. In addition, these spectra show very broad, low transmission resonances interspersed between the high Q ones (e.g. see broad resonances in Fig. 2.4.3d). These resonances represent the complementary, low-Q resonant supermodes that result from the imaginary frequency splitting.

A different device designed for air cladding on both sides of the silicon layer was fabricated on the same chip and further released in post processing (Fig. 2.4.4). Etch windows are created on a chromium mask and transferred onto a 900 nm layer of positive resist (NR9-1000P) covering the device chip. After development, buffered oxide etch (BOE) was used to selectively remove the oxide under the resonator region. To avoid sticking of the device to the bottom silicon due to surface tension in normal evaporative drying, after rinsing in deionized water, isopropyl alcohol (IPA) is used to replace the liquid covering the chip, and is eventually removed in a CO_2 critical point dryer.

Figure 2.4.5a shows an scanning electron micrograph (SEM) image of a released structure and a zoomed in picture of the resonator. The device is a ring resonator with 4 contacts connected to an input and an output coupling waveguide, similar to the 6-contact device shown in Fig. 2.4.3a. The small squares visible on the four corners are density fill pattern required in the SOI fabrication

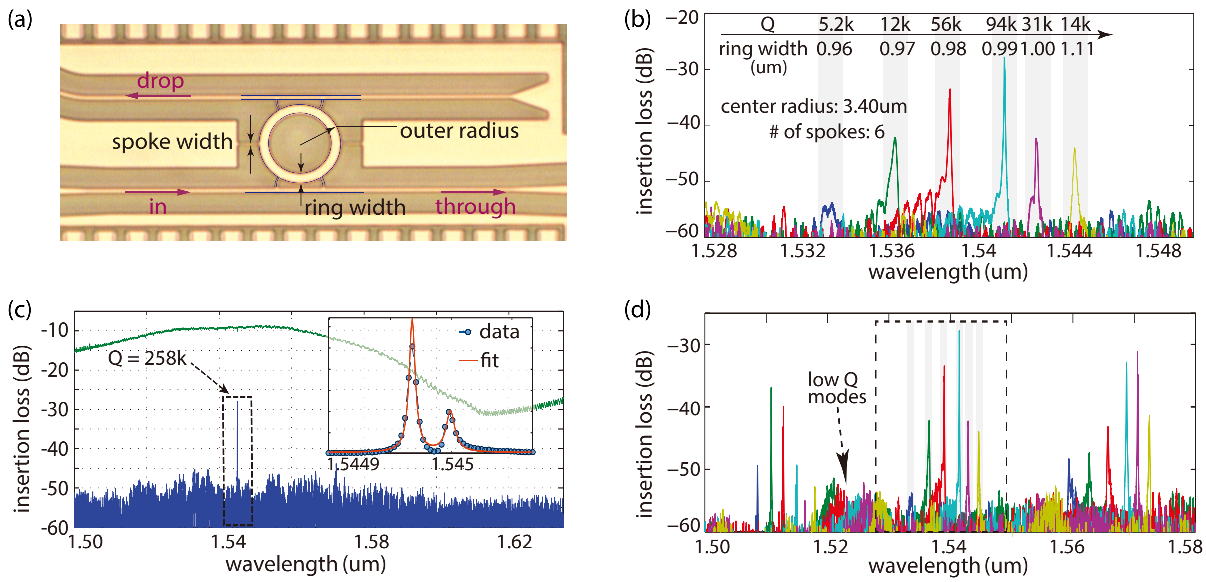

Figure 2.4.3: (a) Microscope image of a fabricated ring resonator with 6 attachments. (b) Measured through- and drop-port spectral responses. Inset: resonance with a Q factor of 258,000. (c) High-Q resonances of 6 devices with linear width variation show an optimum design with maximum Q factor. (d) Zoomed out view of c showing wider spectra.

process for process uniformity [45]. BOE etching was timed to remove the entire thickness (2 μm) of the silica under the device layer, and some fill shapes within the etch window were removed from the chip during the etching and drying, leaving pyramid shaped residuals at their original sites. A higher magnification SEM image on the right confirms that the air-suspended resonator is supported by its 4 contacts connecting it to the partially released waveguides. Direct mechanical connection to a waveguide can be a useful feature for suspended photonic structures, as built in stresses in the device layer can produce out of plane misalignment of adjacent waveguides and other structures without proper stress relief within the design[40]. In this paper, we did not design scattering avoiding structures into the waveguide as well, only the resonator, since the waveguide sees only a single pass loss. However, straight wiggler mode taper arms could be incorporated in the bus waveguide, similar to those in racetrack resonators[89, 90], to minimize overall transmission loss of attached wiggler-mode cavities.

Figure 2.4.5b shows measured through- and drop-port spectral responses from a suspended

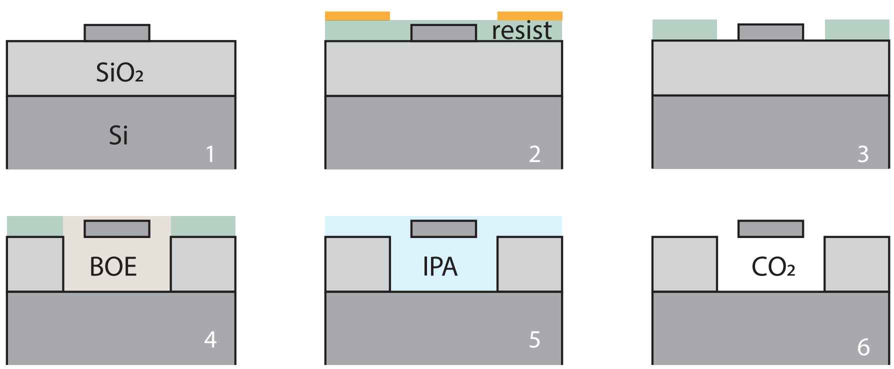

Figure 2.4.4: Process flow for suspending the resonators. A positive resist is spin on the substrate and patterned with a chromium mask to serve as etch windows; oxide under the resonator is then selectively etched with a buffered HF solution (BOE); liquid under device layer is replaced with IPA and eliminated in a CO_2 critical point dryer.

"wiggler" resonator with a quality factor of 139,000, indicating low loss. Out of 42 devices of this design with an intentional dimensional parameter sweep, about half were optically accessible after release, and a third showed Qs above 50,000. In comparison to the devices in Fig. 3 that are not suspended, these structures also show significantly stronger thermal nonlinearity under higher input power.

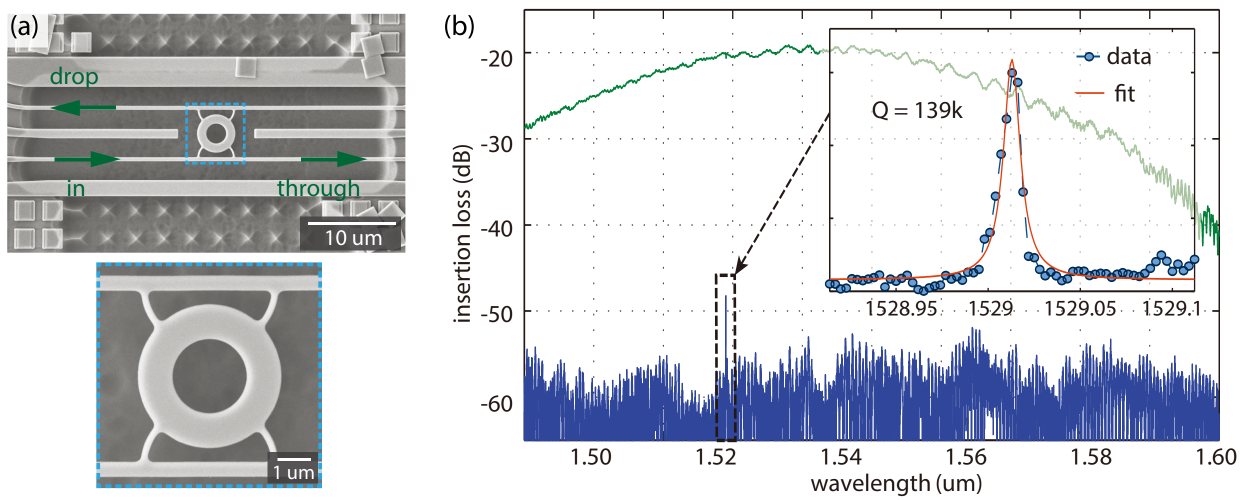

Figure 2.4.5: (a) SEM images of an air suspended ring resonator with 4 attachments attached to coupling waveguides (left) and a zoomed in image of the resonator region (right). (b) Measured through- and drop-port spectral responses. Inset: resonance with a Q factor of 139,000.

The proposed wiggler mode concept, incorporating imaginary coupling (frequency splitting), is demonstrated in a circular symmetry geometry with azimuthal periodicity. The demonstrated resonators may enable important additional degrees of freedom in design of photonic and nanomechanical structures by allowing manipulation of electrical function, thermal properties (mass, impedance), nanomechanical design and phonon modes while preserving a high optical Q. The design may be enabling for applications in light-force actuated photonics on chip, e.g. for state trapping and self-adaptive photonics[81], very efficient thermal tuning by allowing mechanical suspension with potentially higher thermal impedance than e.g. microdisks on a pedestal or even wheel resonators, as well as in other applications such as enabling the tighter mode confinement of an air-silicon interface within a microcavity.

Chapter 3

Evanescent Confinement of Acoustic Waves On Chip

With the tremendous advances in modern lithography and high-resolution nanofabrication that were driven by the electronic integrated circuit (IC) industry, micron-scale photonic circuits, including silicon photonic circuits, have emerged over the past five decades, as a new chip technology showing substantial promise to enable many applications and provide performance superior to electronics (particularly for communication), as well as to enhance CMOS technology itself [43, 98]. High optical refractive index contrast between core and cladding materials in planar photonic waveguide geometries has allowed small, wavelength-scale microphotonic and optoelectronic components to be integrated in complex circuits and systems on a chip, providing capabilities for a wide range of compact high performance applications in communication, sensing and information processing [73]. Since acoustic and optical (electromagnetic) waves share many mathematical similarities [6], an analogous high slowness contrast acoustic wave confinement scheme could bring the same possibilities to acoustics to enable microphononic circuits, where the manipulation of signals in the acoustic domain can maximally benefit from the advancing integration technology and wavelength scale confinement. A key benefit is that evanescent confinement provides for efficient coupling between circuit elements such as waveguides and resonators. The viability of such a scheme will be determined by the achievable device size scale and propagation losses – which will determine the complexity (how far waves can propagate, i.e. through how many components), and the bandwidth (i.e. how long acoustic waves can spend in the circuit without dissipating).

Coherent phonons travel at much slower speeds than photons and can directly interact with radiofrequency or optical signals [26], making chip-scale acoustics or microphononics an interesting domain for researchers in phononics, optomechanics and micro-/nano-electro-mechanical systems (MEMS/NEMS). A wide range of systems have recently been explored, where acoustic waves interact with electronics and photonics in chip-scale integrated platforms to enable optical delay lines [26, 85], narrow-linewidth RF photonic filters [92], photonic-phononic memory [65], frequency locking of micromechanical oscillators [87], systems in the quantum mechanical ground state [19], and on-chip optomechanical signal detection [100]. The ability to confine and guide acoustic waves not only enables the construction of individual devices, but may also provide a means to connect them to form a complete on-chip acoustic circuitry.

Early investigation into acoustic waveguides proposed various geometries including flat overlay waveguides with thin metal strips deposited on a substrate, topological waveguides that confine acoustic fields to a ridge or wedge in a homogeneous material, and in-diffused waveguides that are locally implanted with metals to create a weak impedance contrast [71]. Later developments in surface acoustic wave (SAW) and bulk acoustic wave (BAW) technologies make use of acoustic fields vertically bound to a free material surface or between air and an acoustic reflector, and have enabled commercial applications in radar and communication systems, radio/intermediate frequency signal processing, and chemical/biological sensing [18, 84], despite lack of lateral confinement that allows sharp bends. Acoustic confinement in off-chip cylindrical waveguides has also been investigated, e.g. in the context of Brillouin scattering in low-contrast silica optical fibers [91] and analytically in GaAs-AlAs quantum wires [70].

It would be beneficial to construct lithographically defined, wavelength-scale acoustic waveguides in solid CMOS or CMOS-like chip technology, where circuit complexity could be scaled and efficient interaction with electronics and photonics be utilized. Modern fabrication technologies have enabled the construction of planar structures with an inhomogeneous distribution of materials in the cross-section. Such structures may have high acoustic slowness contrast that allows efficient evanescent guiding of acoustic waves, the topic of this paper. Chip-scale acoustic devices so far still heavily rely upon 1) air suspension, where discontinuation of solid material reflects acoustic waves at free boundaries [93], and 2) phononic crystal structures, where engineered slowness mismatch in a periodic composite material provides wave confinement [62], or a combination of these two mechanisms [33]. Recently, resurgent interest in optomechanics and stimulated brillouin scattering in on-chip devices has led to investigations of novel acoustic waveguiding geometries for strong light-sound coupling, including geometrical [86] and material slowness contrast based (evanescent) [77, 78] confinement.

This chapter investigates in-plane waveguiding in high-slowness-contrast material systems that are compatible with CMOS and amenable to the construction of complex, multielement circuits. In Section 3.1, some basic concepts in solid mechanics will be introduced, including the acoustic wave equation. In Section 3.2, I will discuss guiding of acoustic waves specifically in silicon-based solid materials. Section 3.3 presents considerations on acoustic loss mechanisms, including intrinsic and bending radiation losses and their impact on operating frequency, time and spatial scales of circuits, followed by Section 3.4 the prospects for integrated phononic components in a solid unsuspended platform that would be beneficial to many integrated platforms including CMOS.

3.1 Basics of Solid Mechanics

Strain and Stress Displacement $\mathbf{u}$ of a particle located at $\mathbf{L}$ in the equilibrium state and at $\mathbf{l}(\mathbf{L}, t)$ at time t is

$$\mathbf{u}(\mathbf{L}, t) = \mathbf{l}(\mathbf{L}, t) - \mathbf{L}$$

with its gradient field

$$\mathcal{E}(\mathbf{L},t) = \nabla\mathbf{u} = \begin{bmatrix} \dfrac{\partial u_x(\mathbf{L},t)}{\partial L_x} & \dfrac{\partial u_x(\mathbf{L},t)}{\partial L_y} & \dfrac{\partial u_x(\mathbf{L},t)}{\partial L_z} \\ \\ \dfrac{\partial u_y(\mathbf{L},t)}{\partial L_x} & \dfrac{\partial u_y(\mathbf{L},t)}{\partial L_y} & \dfrac{\partial u_y(\mathbf{L},t)}{\partial L_z} \\ \\ \dfrac{\partial u_z(\mathbf{L},t)}{\partial L_x} & \dfrac{\partial u_z(\mathbf{L},t)}{\partial L_y} & \dfrac{\partial u_z(\mathbf{L},t)}{\partial L_z} \end{bmatrix}$$

A measure of material deformation that reduces to zero for rigid translation and rotation can be define as

$$\Delta = dl^2(\mathbf{L},t) - (dL)^2$$

which can be expressed in matrix form

$$\Delta = 2\left(\begin{bmatrix} dL_x & dL_y & dL_z \end{bmatrix} \begin{bmatrix} S_{xx} & S_{xy} & S_{xz} \\ S_{yx} & S_{yy} & S_{yz} \\ S_{zx} & S_{zy} & S_{zz} \end{bmatrix} \begin{bmatrix} dL_x \\ dL_y \\ dL_z \end{bmatrix}\right)$$

where

$$S_{ij}(\mathbf{L},t) = \frac{1}{2}\left(\frac{\partial u_i}{\partial L_j} + \frac{\partial u_j}{\partial L_i} + \frac{\partial u_k}{\partial L_i}\frac{\partial u_k}{\partial L_j}\right)$$

For small deformation (displacement gradient much smaller than 10^{-4} to 10^{-3}), the quadratic term is negligible, and the linearized strain is

$$S_{ij}(\mathbf{L},t) = \frac{1}{2}\left(\frac{\partial u_i}{\partial L_j} + \frac{\partial u_j}{\partial L_i}\right)$$

$$\mathbf{S} = \frac{1}{2}\left(\mathcal{E} + \mathcal{E}^T\right) = \frac{1}{2}\left[\nabla\mathbf{u} + (\nabla\mathbf{u})^T\right] = \nabla_s\mathbf{u}$$

The antisymmetric component of $\mathcal{E}$ corresponds to local rotation, and the operator ∇_s takes the symmetric component of the gradient field to yield linearized strain tensor $\mathbf{S}$, which is a measure of deformation that excludes rigid body translations and rotations.

Abbreviated Subscript Notation

Since the strain tensor $\mathbf{S}$ is symmetric, this 3×3 matrix can be reduced to a 6-element column matrix following

$$\mathbf{S} = \begin{bmatrix} S_{xx} & S_{xy} & S_{xz} \\ S_{yx} & S_{yy} & S_{yz} \\ S_{zx} & S_{zy} & S_{zz} \end{bmatrix} = \begin{bmatrix} S_1 & \frac{1}{2}S_6 & \frac{1}{2}S_5 \\ \frac{1}{2}S_6 & S_2 & \frac{1}{2}S_4 \\ \frac{1}{2}S_5 & \frac{1}{2}S_4 & S_3 \end{bmatrix}$$

The symmetric gradient operator thus becomes

$$\nabla_s \to \nabla_{Ij} = \left[\begin{array}{ccc} \partial_x & 0 & 0 \\ 0 & \partial_y & 0 \\ 0 & 0 & \partial_z \\ \hline 0 & \partial_z & \partial_y \\ \partial_z & 0 & \partial_x \\ \partial_y & \partial_x & 0 \end{array}\right]$$

Stress

Stress $\mathbf{T}_n$ acting on a surface normal to $\hat{\mathbf{n}}$ in a deformed medium with stress tensor $\mathbf{T}$ is

$$\mathbf{T}_n = \mathbf{T} \cdot \hat{\mathbf{n}}$$

Newton's law in the limit of a small volume gives the translational equation of motion for a vibrating medium:

$$\nabla \cdot \mathbf{T} = \rho\, \partial_t^2 \mathbf{u} - \mathbf{F}$$

where ρ is the mass density of the material, and $\mathbf{F}$ is the external force density acting on the mass. In abbreviated subscript notation,

$$\mathbf{T} = \begin{bmatrix} T_{xx} & T_{xy} & T_{xz} \\ T_{yx} & T_{yy} & T_{yz} \\ T_{zx} & T_{zy} & T_{zz} \end{bmatrix} = \begin{bmatrix} T_1 & T_6 & T_5 \\ T_6 & T_2 & T_4 \\ T_5 & T_4 & T_3 \end{bmatrix}$$

and the divergence operator becomes

$$\nabla \cdot \to \nabla_{iJ} = \left[\begin{array}{ccc|ccc} \partial_x & 0 & 0 & 0 & \partial_z & \partial_y \\ 0 & \partial_y & 0 & \partial_z & 0 & \partial_x \\ 0 & 0 & \partial_z & \partial_y & \partial_x & 0 \end{array}\right]$$

Acoustic Field Equations

In small deformation regime, Hooke's Law states that the stress and the strain are linearly dependent:

$$\mathbf{T} = \mathbf{c} : \mathbf{S}$$

$$\mathbf{S} = \mathbf{s} : \mathbf{T}$$

where $\mathbf{c}$ and $\mathbf{s}$ are the stiffness and compliance tensors. In abbreviated subscript notation,

$$c_{IJ} = c_{ijkl}$$

I	1	2	3	4	5	6
ij	xx	yy	zz	yz	xz	xy

Elastic damping depends on temperature, frequency and type of vibration. At room temperature, acoustic losses can be described by the viscosity and relaxation constants $\boldsymbol{\eta}$ and $\boldsymbol{\tau}$:

$$\mathbf{T} = \mathbf{c} : \mathbf{S} + \boldsymbol{\eta} : \partial_t \mathbf{S}$$

$$\mathbf{S} = \mathbf{s} : \mathbf{T} - \boldsymbol{\tau} : \partial_t \mathbf{S}$$

Introducing the particle velocity field $\mathbf{v} = \partial_t \mathbf{u}$, the equation of motion becomes

$$\nabla \cdot \mathbf{T} = \rho\, \partial_t \mathbf{v} - \mathbf{F}$$

and the strain-displacement relation becomes

$$\nabla_s \mathbf{v} = \partial_t \mathbf{S}$$

Using the elastic constitutive equation

$$\mathbf{S} = \mathbf{s} : \mathbf{T} - \boldsymbol{\tau} : \nabla_s \mathbf{v}$$

the field equation becomes

$$(1 + \tau : \partial_t)\, \nabla_s \mathbf{v} = \mathbf{s} : \partial_t \mathbf{T}$$

Since $\mathbf{c}\,\mathbf{s} = \mathbf{I}$, the acoustic wave equation is

$$\nabla \cdot \mathbf{c} : \nabla_s \mathbf{v} = \rho\, \partial_t^2 \mathbf{v} - \partial_t \mathbf{F}$$

Acoustic Plan Waves in Isotropic Materials The stiffness matrix of an isotropic material has the general form

$$\mathbf{c} = \begin{bmatrix} c_{11} & c_{12} & c_{12} & 0 & 0 & 0 \\ c_{12} & c_{11} & c_{12} & 0 & 0 & 0 \\ c_{12} & c_{12} & c_{11} & 0 & 0 & 0 \\ 0 & 0 & 0 & c_{44} & 0 & 0 \\ 0 & 0 & 0 & 0 & c_{44} & 0 \\ 0 & 0 & 0 & 0 & 0 & c_{44} \end{bmatrix}$$

where

$$c_{12} = c_{11} - 2c_{44}$$

$$\lambda = c_{12},\ \mu = c_{44}$$

In a lossy medium,

$$c_{IJ} \to c_{IJ} + i\omega\eta_{IJ}$$

In a source free region ($\mathbf{F} = 0$), a plane wave propagating along

$$\hat{\mathbf{l}} = \hat{\mathbf{x}}l_x + \hat{\mathbf{y}}l_y + \hat{\mathbf{z}}l_z$$

has fields proportional to $\mathbf{u} \sim \exp[i(\omega t - k\hat{\mathbf{l}} \cdot \mathbf{r})]$. The abbreviated subscript operators reduce to

$$\nabla_{iK} = -ik_{iK} = -ikl_{iK} \to -ik \left[\begin{array}{ccc|ccc} l_x & 0 & 0 & 0 & l_z & l_y \\ 0 & l_y & 0 & l_z & 0 & l_x \\ 0 & 0 & l_z & l_y & l_x & 0 \end{array}\right]$$

$$\nabla_{Lj} = -ik_{Lj} = -ikl_{Lj} \to -ik \left[\begin{array}{ccc} l_x & 0 & 0 \\ 0 & l_y & 0 \\ 0 & 0 & l_z \\ \hline 0 & l_z & l_y \\ l_z & 0 & l_x \\ l_y & l_x & 0 \end{array}\right]$$

The wave equation reduces to

$$\nabla \cdot \mathbf{c} : \nabla_s \mathbf{v} = \rho\,\partial_t^2 \mathbf{v}$$

$$\nabla_{iK}\, c_{KL}\, \nabla_{Lj} v_j = \rho\,\partial_t^2 \mathbf{v}_i$$

$$k^2(l_{iK}c_{KL}l_{Lj})v_j = k^2\Gamma_{ij}v_j = \rho\omega^2 v_i$$

where

$$\Gamma_{ij} = l_{iK}c_{KL}l_{Lj}$$

is the Christoffel matrix. In isotropic material, the term on the left is equal to

$$k^2 \left(c_{44} + (c_{11} - c_{44}) \begin{bmatrix} l_x l_x & l_x l_y & l_x l_z \\ l_y l_x & l_y l_y & l_y l_z \\ l_z l_x & l_z l_y & l_z l_z \end{bmatrix} \right) \begin{bmatrix} v_x \\ v_y \\ v_z \end{bmatrix} = c_{44} k^2 \mathbf{v} + (c_{11} - c_{44}) \mathbf{k}(\mathbf{k} \cdot \mathbf{v})$$

The Christoffel equation for plane waves in anisotropic solid can be rewritten as

$$\left[k^2 \Gamma_{ij} - \rho \omega^2 \delta_{ij}\right] [v_j] = 0$$

and a dispersion relation can be obtained from

$$\Omega(\omega, k_x, k_y, k_z) = \left| k^2 \Gamma_{ij}(l_x, l_y, l_z) - \rho \omega^2 \delta_{ij} \right| = 0$$

For fixed ω, $k(\mathbf{l})$ defines the wave vector surface which scales with ω. The inverse of the phase velocity $k/\omega = 1/V_p$ gives the slowness (inverse velocity) surfaces.

3.2 Guiding Acoustic Waves in Silicon-based Solids

In an inhomogenous material geometry, scattering at a material boundary requires that the particle displacement and normal stress fields be continuous. For example, at a planar interface at $z = 0$ (normal position $\mathbf{r}_\perp \equiv \hat{z}z = 0$), the tangential wave vector $\mathbf{k}_\parallel \equiv \hat{x}k_x + \hat{y}k_y$ must be equal in both materials to give the same spatial field dependence $\exp(i\mathbf{k}_\parallel \cdot \mathbf{r}_\parallel)$ that avoids discontinuities. In the slowness picture, when a wave is incident on the interface from one side, this means that the tangential component of $1/\mathbf{v}_p = \mathbf{k}/\omega$ must be conserved across the interface as a corresponding wave is excited in transmission on the other side of the interface. If the interface undulation is slower than the wave in the second, cladding material, then the "transmitted" wave is evanescent with an imaginary $\mathbf{k}_\perp$, as in the familiar case of optical waveguides.

However, since materials are in general trirefringent for acoustic propagation, with three slowness curves, for one longitudinal and two shear/transverse polarizations (amorphous materials are isotropic with degenerate shear modes), acoustic confinement is more complex to achieve than optical confinement. Depending on the relation between wave speeds in materials, up to five critical angles can exist, $\theta_{\mathrm{cr}} = \sin^{-1}(\frac{v_i}{v_r})$, where v_i and v_r are the velocities of the incident and refracted waves and $v_i < v_r$. These critical angles are associated with reflected waves of other polarizations in the incident material, and refracted waves in the other material. Beyond all possible critical angles the incident wave undergoes total internal reflection. For a cladded structure to be evanescently confining, the slowness of its waveguide modes must fully enclose the slowness curves of all polarizations in the cladding, to prevent scattering into propagating bulk modes.

In a rectangular waveguide with Si cladding and SiO_2 core, sidewalls couple shear and longitudinal plane waves into hybrid modes, among which the ones with primarily shear components have slower speeds than the fastest polarization in the cladding and can thus be fully confined in the SiO_2 core. Figure 3.2.1b illustrates four possible configurations for high-contrast dielectric acoustic waveguides utilizing evanescent confinement between two materials and free air interfaces that can potentially suit different applications and fabrication platforms. The fully-cladded waveguide (Fig. 3.2.1b[i]) consists of a slow core surrounded by a fast cladding, drawing a direct analogy to cladded rectangular optical waveguides. Figure 3.2.1b[ii] and [iii] are half-cladded waveguides with the top surface of the core exposed to air. The embedded version (Fig. 3.2.1b[iii]) has a planar top surface that could further interface to transducers, such as patterned metal electrodes. Side-cladded waveguides on an air-suspended membrane (Fig. 3.2.1b[iv]) provide an alternative to phononic crystal waveguides for systems without a compatible layer stack to evanescently confine acoustic waves in the vertical direction.

As a simple example to illustrate the behavior of evanescent mode acoustic waveguides, Fig. 3.2.1c shows the mode field distributions of a fully-cladded rectangular waveguide with SiO_2 core and Si cladding simulated using COMSOL Multiphysics [68]. A 3D section of the waveguide was simulated using the Solid Mechanics module, with Perfectly Matched Layer (PML) boundary conditions applied on the lateral faces and Floquet-Bloch boundary condition on the longitudinal faces for a given propagation constant. Guided modes split into two categories, horizontal (H) modes with a strong field component in the transverse plane along the horizontal edges of the core cross-section and vertical (V) modes along the vertical edges. Figure 3.2.1d shows the slowness

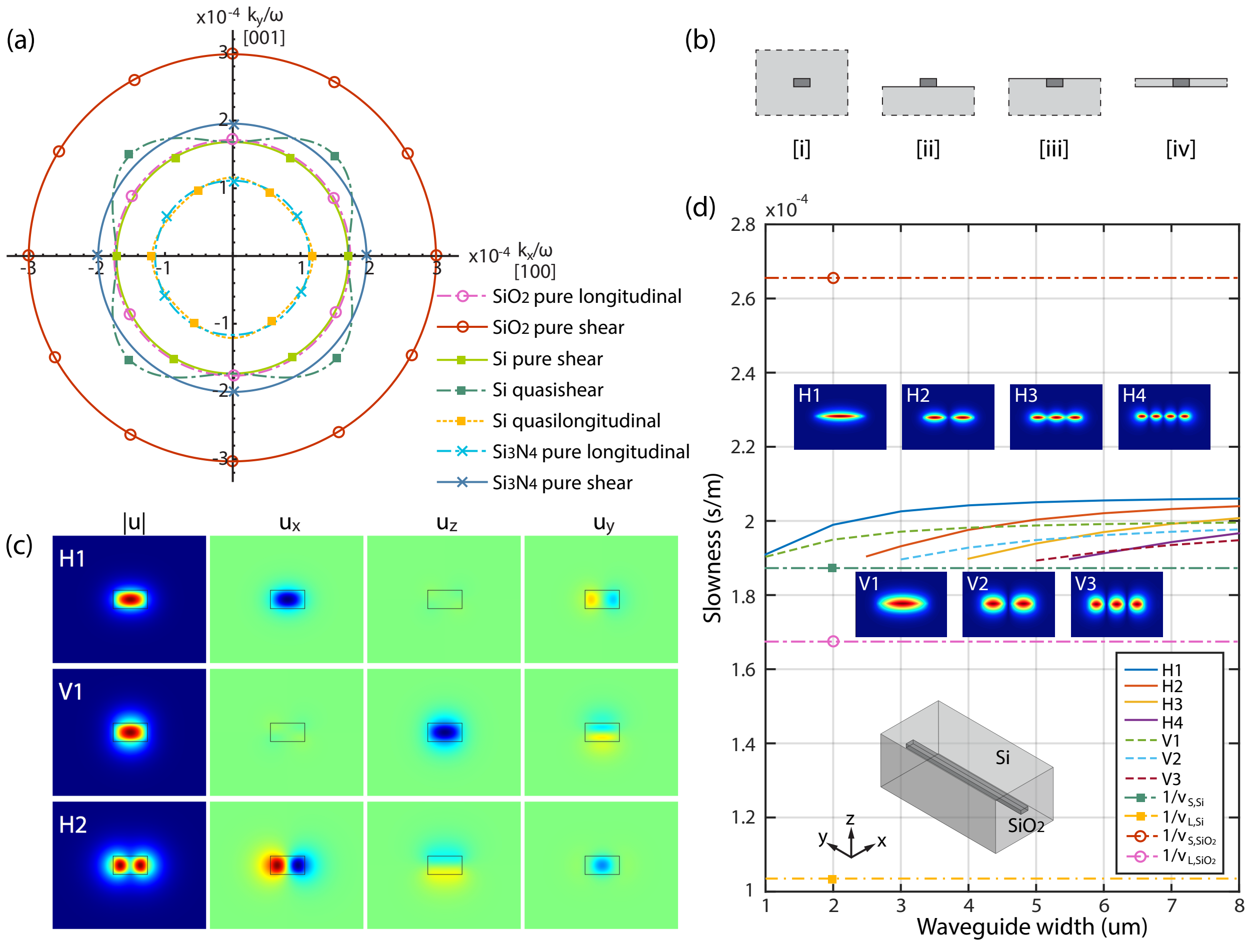

Figure 3.2.1: (a) Slowness curves of acoustic plane waves propagation along crystal faces in bulk Si, SiO_2 and SiN. (b) Possible geometries for high-contrast dielectric acoustic waveguides: [i] fully-cladded [ii] half-cladded [iii] half-cladded, embedded [iv] side-cladded, membrane. (c) Total displacement $|u|$ (blue/red represents min/max displacement), and horizontal u_x, vertical u_z and longitudinal u_y components (blue/red represents negative/positive displacement) of the first three horizontally (H) and vertically (V) polarized eigenmodes in a fully cladded rectangular waveguide with a $1\mu\text{m}\times 2\mu\text{m}$ SiO_2 core surrounded by Si cladding. (d) Slowness ($1/v_p$) v.s. waveguide core width for fixed waveguide height of 0.5μm and wavelength $\lambda = 1.5\mu$m.

curves of the first few horizontal and vertical modes versus waveguide width for a fixed height of 0.5μm and wavelength $\lambda = 1.5\mu m$. In 3D, a short slice of a y-invariant waveguide can be simulated with the displacement field $\mathbf{u}$ satisfying the Floquet-Bloch boundary condition, $\mathbf{u}(y_2) = \mathbf{u}(y_1)\exp[ik_y(y_2 - y_1)]$, where $k_y = 2\pi/\lambda = \omega/v_p$. (Alternatively a 2+1D solver can more efficiently solve for the modes of a waveguide with constant crosssection [24]). All guided modes are below the shear wave slowness in the SiO_2 core, but above that in the cladding, at which point waves in the core start refracting into the cladding, losing evanescent confinement at the interface. The width of an acoustic waveguide can be designed through numerical simulation to support only the lowest order horizontal and vertical modes, which approach degeneracy at small waveguide widths, and thus there is no apparent cutoff for the fundamental vertically polarized (V1) mode.

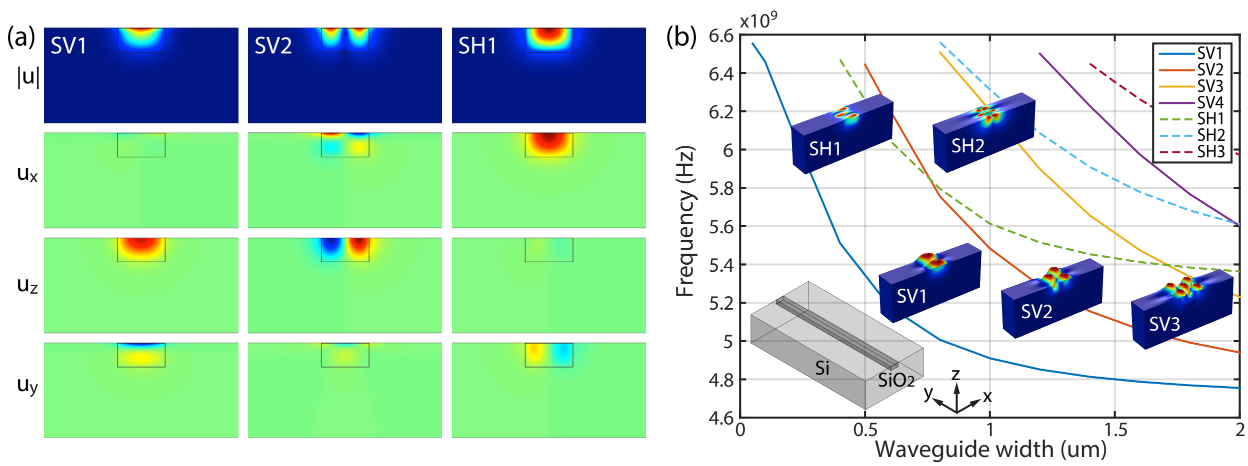

Figure 3.2.2: (a): Total displacement $|\mathbf{u}|$ (blue/red represents min/max displacement), and horizontal u_x, vertical u_z and longitudinal u_y components of the first three vertically (SV) and horizontally (SH) polarized surface modes (blue/red represents negative/positive displacement) of a half-cladded waveguide with a 0.5μm$\times$1μm Si core embedded in SiO_2 cladding. (b) Slowness ($1/v_p$) v.s. waveguide core width for fixed waveguide height of 0.5 μm and wavelength λ= 0.75 μm.

Combining evanescent confinement and free air interfaces, the embedded half-cladded geometry, Fig. 3.2.1b[iii], can be a more practical configuration in terms of fabrication, and it provides better access to the mode fields that are tightly concentrated on the exposed top surface of the core and leverage surface wave components. Figure 3.2.2a shows the field components of the first three vertically (SV) and horizontally polarized (SH) surface modes. The SV modes have a dominant vertical shear component (u_z), which spreads across the core with field maxima on the top surface; the shear horizontal (u_x) and longitudinal (u_y) components are evanescently confined to the top surface, resembling Love waves in a half-cladded slab [6]. The SH waves have a dominant shear horizontal (u_x) component. The half-cladded acoustic waveguides could be fabricated directly into a silicon substrate using localized thermal oxidation defined by a hardmask. Alternative fabrication methods include chemical vapor deposition of SiO_2 on a pre-patterned silicon trench followed by chemical mechanical planarization (CMP), or a different fast material such as SiN can be used as a substrate underneath the Si/SiO_2 layer to provide a bottom cladding, and the oxide waveguide can be patterned from a device layer using regular scanning electron beam or optical lithography. This waveguide geometry has tight lateral confinement that allows for sharp bends with low radiation loss, enabling ultra-compact components, and high concentration of fields on the top surface, making it a versatile candidate to allow interfacing acoustic waves to other systems with different signal carrying physics, such as electronic circuits or guided light waves.

Our ultimate goal in considering high slowness contrast evanescent confinement is to construct chip-scale phononic components and coupled-element circuits that can enable a richer signal processing capability. High slowness contrast enables compact components on the order of $10\,\mu$m, which will be discussed in more detail in Sec. 3.4. However, the practicability of a phononic circuitry such as that described here requires that signal propagation lengths in waveguides are large enough to traverse a few components, and that excitation lifetimes in resonators are long enough to process (e.g. filter or delay) relevant bandwidth signals and couple the energy faster to the next circuit element than to the radiation loss mechanisms. Therefore, in the following, we first consider acoustic loss mechanisms and the bounds they place on performance of waveguides and resonators in order to evaluate the viability of high-contrast microphononic circuits. We consider intrinsic material losses in the next section, and then radiation loss (a generalized anchor loss mechanism) in the following section on device design.

3.3 Loss Considerations

A key consideration in understanding the utility, and range of applicability, of these acoustic waveguides is loss. In this paper we consider two mechanisms: material intrinsic loss, dealt with in this section, and acoustic radiation loss, a fundamental loss mechanism which occurs due to bending of otherwise lossless waveguides, discussed in the next section because it is associated with device design. For conventional on-chip acoustic devices, energy dissipation is mainly caused by air damping, anchor loss and intrinsic material losses [58, 112]. Air damping includes a few different mechanisms and is often dominated by squeeze-film damping for suspended structures with small air gaps between a vibrating film and a stationary substrate [16, 112]. Anchor loss is caused by acoustic radiation into the substrate through attachments such as pedestals and spokes [53, 55] that provide mechanical support for suspension. Having acoustic waves fully confined in solids evanescently (without air suspension) exempts this type of devices from squeeze-film damping and from conventional anchor loss (radiation into the cladding, in straight sections), but intrinsic material losses still impose a limit on the frequency range where low loss waveguides and resonant cavities with high quality factors can be achieved. Hence they are addressed first in the context of their impact on wavelength scale devices and circuits.

The two main intrinsic loss mechanisms for acoustic devices are thermoelastic dissipation (TED) and phonon-phonon interaction associated dissipation (PPD), which both result from coupling between the acoustic field and thermal phonons in solids, at different time and length scales [7, 15, 20, 25, 63]. The total material intrinsic loss limited quality factor $Q_{\text{intrinsic}}$ is given by $Q_{\text{intrinsic}}^{-1} = Q_{\text{TED}}^{-1} + Q_{\text{PPD}}^{-1}$, where Q_{TED} and Q_{PPD} are Q limits due to TED and PPD respectively.

TED describes the energy dissipation associated with coupling between a strain field and a temperature gradient through irreversible heat flow (absent in volume preserving pure shear waves). TED is dependent on the specific geometry of an acoustic device, and can be minimized in design by reducing the overlap of the strain field induced by the acoustic wave and the heat diffusion eigenmodes of the system [20], but the bulk limit still provides a general measure of feasibility of materials for acoustic wave guiding. Landau and Lifshitz calculated the attenuation coefficient for longitudinal waves in amorphous (isotropic) solids, which also gives an order of magnitude estimate for anisotropic crystals [49]. An equivalent expression for Q_{TED} at angular frequency ω and temperature T is [7, 15, 20]

$$Q_{\text{TED}} = \frac{9C_v^2}{\omega\kappa T\beta^2\rho} \tag{3.1}$$

where C_v, κ, β and ρ are the volumetric heat capacity, thermal conductivity, thermal expansion coefficient and mass density.

PPD describes interactions between incident acoustic waves and thermally excited phonons that happen at shorter time and length scales than TED. Akhiezer considered this loss mechanism in the low frequency regime $\omega\tau \ll 1$ (Akhiezer regime), where τ is the lifetime of the thermal phonons, and used the Boltzmann equation to derive the attenuation by calculating the increase in entropy due to collisions between thermal phonons [2]. Woodruff and Ehrenreich and others further developed this theory for $\omega\tau > 1$ in the regime $\omega \ll k_B T/\hbar$ [111]. A simplified expression for Q_{PPD} in the extended frequency range $\omega \ll k_B T/\hbar$ is [51, 63]

$$Q_{\text{PPD}} = \frac{1+\omega^2\tau^2}{\omega\tau}\frac{\rho v_g^2}{C_v T}\left(\langle\gamma^2\rangle - \langle\gamma\rangle^2\right)^{-1} \tag{3.2}$$

where v_g is the group velocity of the acoustic wave, related to the mode (or phase) velocity v_p by $1/v_g \equiv \frac{\partial}{\partial\omega}(\omega/v_p(\omega))$, and γ is the phonon mode Grüneisen parameter. Here, neglecting dispersion, v_g is taken to be approximately equal to the phase velocity of the acoustic wave $v_p = \omega/k$, and τ is estimated using the kinetic relation $\kappa = \frac{1}{3}\tau C_v V_D^2$ and $3V_D^{-3} = V_l^{-3} + 2V_t^{-3}$, where V_D, V_l and V_t are the Debye, longitudinal and transverse wave velocities [15, 63]. $\langle\rangle$ indicates averaging over interacting thermal phonon modes [3, 51, 69].

Using material property values listed in Table 3.1, Fig. 3.3.1(a) plots the upper bounds, due to each of TED and PPD, to the quality factors (Q) achievable in Si, SiO_2 and SiN, at room temperature (T = 300K). The upper bound Q is a loss Q of a resonator implemented in the respective material, and a specific acoustic resonator design based on evanescent confinement using multiple materials will see a average of these losses with the mode field as weighting function, in

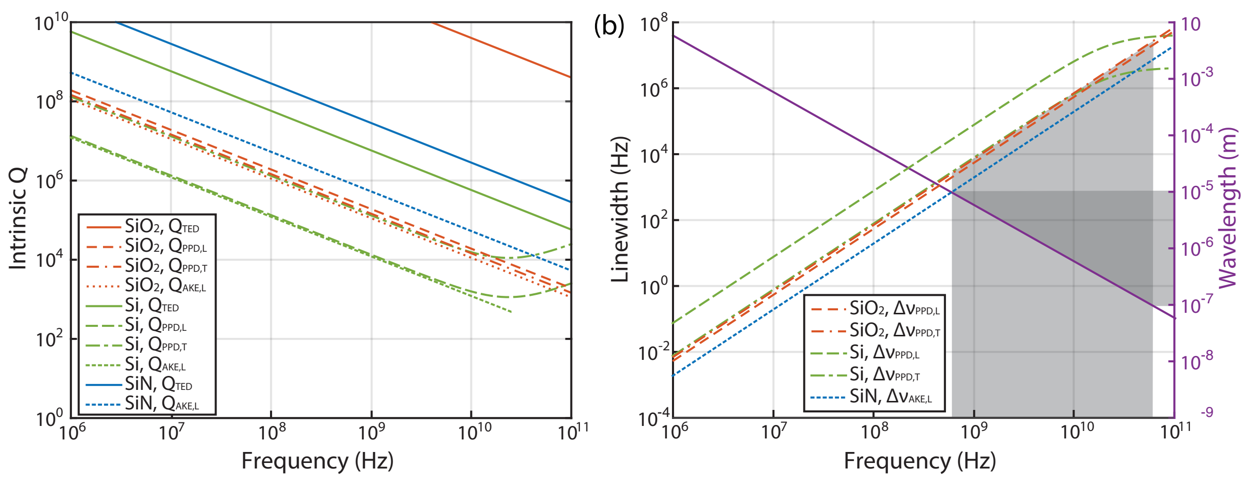

Figure 3.3.1: (a) Q limits due to thermoelastic (solid lines) and phonon-phonon dissipations (dashed lines) for SiO_2, Si and SiN. (b) Intrinsic linewidths corresponding to the Q limits (dashed/dotted lines) and characteristic wavelength (pure shear wave in bulk Si, solid line) scaling versus frequency.

Parameter	density (kg/m^3)	specific heat capacity (J/kg·K)	thermal conductivity (W/m·K)	thermal expansion ($\times 10^{-6}$K^{-1})	wave speed long. (m/s)	wave speed trans. (m/s)	Debye temperature (K)	Grüneisen parameters long.	Grüneisen parameters trans.	Grüneisen parameters long.	Grüneisen parameters trans.	phonon lifetime ($\times 10^{-12}$s)
Symbol	ρ	$C_s = C_v/\rho$	κ	β	V_l	V_t	θ	γ_L	γ_T	$\langle\gamma^2\rangle - \langle\gamma\rangle^2$	$\langle\gamma^2\rangle^{\dagger\dagger}$	τ
Si[25]	2330	713	145[32]	2.6[32]	7470	5860	640	0.65	0.75	0.46[69]	0.03[69]	$6.7^\ddagger$
SiO_2	2300[56]	1000[56]	1.1[56]	0.5[60]	5748[56]	3333[56]	290[44]	−2.1[104]	−1.75[104]	0.88[69]	0.38[69]	$0.13^\ddagger$
SiN	2500[57]	170[57]	19[60]	0.8[60]	8788[57]	5053[57]	290[67]	0.4[17]†	$0.4^\dagger$	–	–	$4.2^\ddagger$

Table 3.1: Material properties used for calculating Q limits due to thermoelastic and phonon-phonon dissipations at $T = 300K$. † Bulk value for β-Si_3N_4 used as estimate. ‡ Calculated using $\tau = \frac{3\kappa}{\rho C_s V_D^2}$[15, 63]. $^{\dagger\dagger}\langle\gamma\rangle$ vanishes for transverse waves [50, 64].

addition to possible interface losses, but these values provide bounds. Since there is very limited data in the literature on $\langle\gamma\rangle$ and $\langle\gamma^2\rangle$ for materials other than Si, a slightly different form of the Q_{PPD} in the low frequency Akhiezer regime ($\omega\tau \ll 1$) for longitudinal waves was plotted in addition to Eq. 3.2, following derivation from Duwel **et al.**[25]

$$Q_{\mathrm{AKE,L}} = \frac{\rho V_l^5 \hbar^3}{k_B^4 T^4}\left[\frac{3\omega\tau}{2\pi^2}\left(\frac{V_l}{V_t}\right)^3 \int_0^{\frac{\theta}{T}} \frac{x^4 e^x dx}{(e^x - 1)^2}\right]^{-1} \gamma_{\mathrm{eff}}^{-2} \tag{3.3}$$

where θ is the Debye temperature. Eqn. 3.3 is evaluated in addition to Eqn. 3.2 for comparison, using effective Grüneisen parameter $\gamma_{\mathrm{eff}} = (\gamma_L + 2\gamma_T)/3$, where γ_L and γ_T are the longitudinal and transverse Grüneisen parameters [3, 104]. Q_{TED} drops in inverse proportion to frequency, as does Q_{PPD} in the Akhiezer regime. As $\omega\tau$ exceeds 1, Q_{PPD} turns around and improves as frequency increases. For all three materials (and as a more general rule of thumb), PPD is the more limiting loss mechanism.

A key interest in phononics is as a competing or complementary and potentially synergistic technology to photonics in signal processing, where relevant context is provided by assessing signal processing bandwidths, or potential interaction with optical modes via radiation pressure, photoelasticity or electrostriction. Although the Q limits in Fig. 3.3.1(a) for acoustic resonators may appear low compared to optical devices ($Q \equiv \omega_o\tau_r/2$, with τ_r the lifetime), the critical metric is the resonance lifetime τ_r and associated linewidth $2/\tau_r$, and the much lower center frequency of acoustic waves makes it possible to design resonant devices with much narrower linewidths than typical optical devices on chip that are compatible with silicon processing and usually support no narrower than several GHz of bandwidth. The dashed lines in Fig. 3.3.1(b) are calculated resonance linewidths that correspond to the material loss limited Q in Fig. 3.3.1(a). Pure shear wave wavelength in bulk Si is plotted versus frequency in solid line to provide a characteristic length scale [shear wave slowness in Si cladding cuts off guided modes in the all cladded waveguide geometries, c.f. Fig. 3.2.1(d)]. For modern fabrication processes, a relevant range of device dimensions is between 100nm and 10μm, corresponding to operating frequencies in the $1-100$ GHz range and material intrinsic linewidths from 1 kHz to 10 MHz in SiO_2. In terms of spatial propagation, these linewidths correspond to a loss Q of about 3,000 to 300,000, which can be converted to an equivalent waveguide propagation loss attenuation constant in dB/mm by the relation $\alpha_{\mathrm{dB/mm}} = \frac{0.01}{\ln(10)}\frac{\omega}{2Qv_g}$. The approximate attenuations corresponding to the gray region in Fig. 3.3.1(b) are 0.004 to 90 dB/mm (assuming $v_g \approx 3,000\,\mathrm{m/s}$, i.e. SiO_2 core). With compact circuits down $10-100\,\mu$m this is still sufficient for useful functions even at the higher end of the frequency range. These linewidths and lengthscales suggests a potentially viable technology for discriminating signals of such or larger bandwidths and/or producing delays (and associated propagation distances) about the inverse of these bandwidths with reasonable loss.

Alternatively to Eqns. 3.2 and 3.3 and similar expressions where acoustic attenuation due to PPD is evaluated using Grüneisen parameters, the effective phonon viscosity method can be used to describe material loss from the same mechanism [35, 48, 51, 110]. The phonon viscosity tensor is a representation that relates stress $\mathbf{T}$ to strain $\mathbf{S}$ as $\mathbf{T} = \mathbf{c} : \mathbf{S} + \boldsymbol{\eta} : (\partial_t \mathbf{S})$. It is analogous to the imaginary part of complex refractive index (i.e. permittivity tensor) for optical waves, which describes material absorption. The effective attenuation constant α of a particular mode of an acoustic waveguide can be calculated by an overlap integral of the displacement field $\mathbf{u}$ with the material viscosity tensor $\boldsymbol{\eta}$, $\alpha = \frac{\omega^2}{P_B}\int d^2r \sum_{jkl} u_i^* \partial_j \eta_{ijkl} \partial_k u_l$, where P_B is the power of the acoustic mode [110]. While an analogue to optical refractive index provides an intuitive formalism and straightforward accounting of mode field distribution in overall loss via overlap integrals, there are discrepancies between the experimental values of the viscosity tensor of Si as measured in the few available previously published experiments [51]. Further, the viscosity tensors of SiO_2 and SiN do not appear to be available in existing literature [110]. For these reasons the Akhiezer model with Grüneisen parameters is used in this paper to provide a rough estimate of limitations on the acoustic loss Q due to phonon-phonon interactions, which is sufficient for evaluating the promise of wavelength-scale phononic components and multi-element "circuits". A more accurate characterization of the bulk material losses, as well as of material interface losses which we do not address here, could become important in the detailed design of devices but are beyond scope for our discussion.

3.4 Integrated Phononic Devices

In this section, we discuss the design of components. The intrinsic material losses set the upper limits for propagation length and time delay, and complex circuits are only possible if useful functions can be accomplished in smaller length and time scales, thereby allowing several components to be traversed before the signal is lost. We show here that high slowness contrast allows compact enough components and strong enough confinement to enable practical microphononic circuits, including coupling and routing of signals between elements. A second key loss mechanism which is critical to determining the compactness of components (and hence viability of the circuits) is radiation loss, a generalized form of anchor loss that we address first.

The evanescent confinement between fast and slow materials enables a family of guided, traveling acoustic wave components that can be designed using techniques similar to those developed for photonic components. Fig. 3.4.1 shows simulations of example components we designed: an evanescent directional power coupler, a 1×2 3 dB wave power splitter, and an acoustic microring resonator. They are based on a $0.5\times0.5\,\mu$m silica core embedded into a silicon substrate, similar to Fig. 3.2.2. We simulated guided acoustic wave propagation through these devices, and find that compact components on the order of $10\,\mu$m in dimension can achieve full power transfer, power splitting, or provide a functioning high-Q resonator. We next discuss design in more detail.

Radiation loss occurs when a confined mode has an accessible radiation channel, and loses energy (referred to as a leaky mode). Straight embedded acoustic waveguides can be designed to be fully confining, with no radiation loss. Curved acoustic waveguides formed in a solid, however,

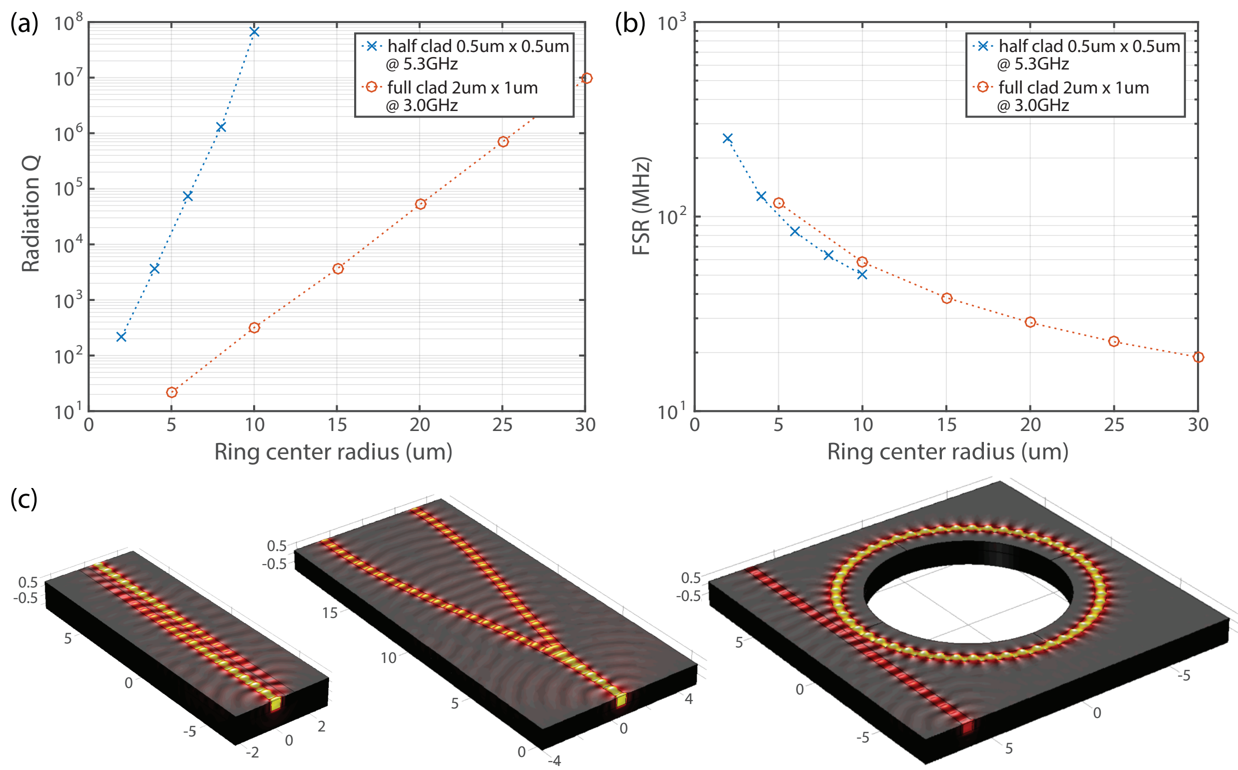

Figure 3.4.1: (a) Radiation loss Q and (b) free spectral range versus ring center radius of half-cladded rings with $0.5\mu m \times 0.5\mu m$ SiO_2 core and fully-cladded rings with $1\mu m \times 2\mu m$ SiO_2 core from finite element simulations. (c) Simulated field profiles of acoustic directional coupler, Y-splitter and coupled ring resonator using an embedded waveguide cross-section with $0.5\mu m \times 0.5\mu m$ SiO_2 core half-cladded with Si.

have a fundamental radiation loss mechanism, analogous to that in optical waveguides. Because there is an evanescent tail of the acoustic wave extending into the cladding material (orthogonal to the mode propagation direction), and the phase fronts circulate azimuthally around a circular waveguide bend, there is a radius at which the guided wave phase fronts exceed the local speed of sound. This radius defines the acoustic radiation caustic, and results in radiation. The radiation loss increases exponentially with smaller radius of curvature of the waveguide. This loss mechanism limits how small a radius can be used to form a waveguide bend to route an acoustic signal between components, or an acoustic microring resonator. Fig. 3.4.1a plots the resonator Q due to bending-induced radiation loss for two designs of acoustic ring resonator, as a function of the ring resonator radius. One can also obtain from these curves the single-pass signal attenuation in dB per 90-degree turn due to bending, relevant to compact routing of signals between components, as $\mathrm{L_{dB90}} = \frac{5}{2\ln 10}\frac{2\pi R\omega}{v_g Q}$.

In Fig. 3.4.1a, one ring design has a half-cladded cross-section (see Fig. 3.2.1b[iii], dimensions in caption of Fig. 3.4.1), and is designed for a resonant frequency of 5.3 GHz as an example. As the radius is varied, different azimuthal mode orders (number of wavelengths around the ring) correspond to the 5.3 GHz resonance frequency. A very small increase in radius (to a few microns) is needed to make the radiation loss negligible, and the total Q to be limited by another (e.g. intrinsic material loss) process. A second ring design uses a fully-cladded cross-section (Fig. 3.2.1b[i], dimensions in caption of Fig. 3.4.1), and is designed for a 3.0 GHz resonant frequency at various radii. The first design is shown in Fig. 3.4.1c[iii], for a radius (to center of ring waveguide) of 6 μm, coupled to a bus waveguide. The bus waveguide excited the ring resonator via evanescent coupling, i.e. same power transfer mechanism seen in the directional coupler in Figure 3.4.1c[i], discussed next. This provides a 2-port (notch, or all-pass) filter function. Both ring resonator geometries allow for tight micron scale bends that are suitable for integrated systems on chip.

Because each azimuthal order yields a resonance, the ring resonator has a period pattern of resonances with a spacing called the free spectral range (FSR). Smaller-radius resonators have fewer wavelengths around, so they need a larger increase in frequency to add a full extra wavelength and reach the next resonance condition – that is, the spacing between azimuthal mode frequencies is larger. The FSR is given by the inverse of the round trip travel time (group delay) around the ring, i.e. FSR$= v_g/L_{\mathrm{rt}}$, where L_{rt} is the cavity round trip length.

Figure 3.4.1b shows the free spectral range (FSR) of the two specific designs showing that several MHz to several tens of MHz FSRs are supported. The FSR can accommodate a number of frequency channels and serve as a multiplexer if the FSR is much larger than a passband of one filter. Assuming radii are chosen large enough, bending loss Q's can exceed 10^4 to 10^5, so that intrinsic linewidths are 0.05 MHz to 0.5 MHz. The other loss mechanism considered here was material intrinsic loss, and Fig. 3.3.1 shows that at $3 - 5.3$ GHz frequencies the intrinsic linewidth is limited to $20 - 70$ kHz, corresponding to Q's of 75,000 to 150,000. Total loss Q is due to the summation of inverse Q's, $1/Q_{\mathrm{total}} = 1/Q_{\mathrm{intrinsic}} + 1/Q_{\mathrm{bending}}$. Thus, total loss Q's in the 10^4 to 10^5 range might be expected, giving intrinsic cavity linewidths of 50 kHz to 500 kHz. A resonant filter of the kind shown in Fig. 3.4.1c[iii], configured with a waveguide-ring gap spacing to produce critical coupling results in a notch filter with twice the bandwidth, 100 kHz to 1 MHz. Thus, with several MHz FSR, a frequency demultiplexer comprising several channels to tens of channels could be designed. In general, since radiation loss is subject to design (e.g. choice of ring radius) while material losses are more constraining , a designer will usually aim for a radiation Q that considerably exceeds the intrinsic Q so as to not further degrade the loss Q and linewidth. This analysis shows that compact, few-micron-scale bends and resonators are realizable in an embedded acoustic waveguide platform with high slowness contrast. Beyond ring resonators, other acoustic components can be designed as well, by analogy with their optical counterparts.

Having covered the viability of waveguides and resonators, the two basic elements of wave systems in that one carries power and the other stores energy, we next turn to the fundamental elements needed to interconnect them. Our goal is again to evaluate the scaling of these components in the high slowness contrast regime. Fig 3.4.1c shows field profiles from frequency domain simulations of an acoustic directional coupler [left] and a Y-splitter [middle], using an embedded waveguide cross-section with $0.5\mu\mathrm{m}\times0.5\mu\mathrm{m}$ SiO_2 core half-cladded with Si (c.f. Fig. 3.2.1b [iii]).

The directional coupler (DC) is a fundamental component, having two input ports and two output ports, that enables a designed splitting ratio of the power in a wave at one input port into the two output ports. DCs enable the connection of resonators to ports as in the example given above, and the construction of interferometers. The DC shown in Fig 3.4.1c[left] employs evanescent coupling whereby modes of two waveguides that are in closer transverse proximity than the extent of their evanescent fields outside the core will interact and exchange significant power if they are synchronous, i.e. their propagation constants are matched, which automatically occurs with two identical guides. A few comments can be made with respect to the scaling of directional couplers. The basic figure of merit for a directional coupler is the length for a given fraction of power transferred – here we choose the full-power transfer length as a baseline. In the high slowness contrast regime, the power transfer can be rapid and full-transfer lengths very short – order of 10 μm in the case of Fig. 3.4.1c[left]. Since power transfer from one waveguide to the other after length l of coupling is $|t_{21}|^2 = \sin(\kappa l)^2$, where κ is the coupling strength (in rad/m) which falls exponentially with the gap between the waveguides due to the exponential evanescent field. The full power transfer length, or beat length, is given by $l_{\text{full}} = \pi/(2\kappa)$, and κ can be related to the propagation constants of the symmetric and antisymmetric guided supermodes of the guided pair, $\kappa = \beta_s - \beta_a$ – the stronger the coupling, the higher the splitting of β_s and β_a. Since the phase velocities of the supermodes $v_{p,s}$ and $v_{p,a}$ typically fall between the core and cladding wave speeds for bulk dominated modes, the guidance condition and material slowness contrast imposes an upper limit on the coupling strength, $\kappa < \omega/v_{p,core} - \omega/v_{p,cladding}$.

Clearly, high slowness contrast provides a larger upper bound to the coupling strength, and hence shorter coupling length. For our case using SiO_2 core and Si cladding, and assuming shear wave dominance in the modes, we can approximately use 3,000 and 6,000 m/s as the respective velocities. For frequencies in the gray region in Fig. 3.3.1b (about 1 to 100 GHz), this lower bound on coupler length is 5 μm or shorter depending on frequency. Note that all of these estimates are independent of particular geometry. In reality confinement and design for radiation loss will produce designs with longer lengths – consistent with our 10 μm length example in Fig 3.4.1c[left].

For directional couplers, the straight coupling region does not incur limitations of bending losses, although bringing isolated waveguides to them does, so the total length of a coupler including connections might be 2-3 times the size given our estimates of bend radii.

Another fundamental component of wave circuits (such as integrated optical circuits, or microwave circuits) are Y-branch 3 dB splitters. Directional couplers provide arbitrary splitting ratios, but broadband designs are difficult to achieve even in integrated optics, where 1% bandwidth is considered broadband (i.e. 2 THz of a 200 THz carrier). In acoustic circuits, one may desire 10% or higher bandwidths, requiring wideband design more akin to microwave engineering than integrated photonics. DCs are furthermore sensitive to fabrication variations. Hence, the Y-branch splitter is a device that guarantees 3 dB (50:50) splitting, an important ratio for interferometers and power splitter trees, by symmetry. The Y-branch splitter involves a splitting region and branch arms to separate the ports. The splitting region can be very compact – a few microns in both in-plane dimensions following similar slowness contrast arguments to the DC length. Based on bend radii of order 10 μm, Fig 3.4.1c[middle] shows a 3 dB power splitter that using S-bends that is about 20 μm long and 10 μm wide (including port separation) for 3.35 GHz operating frequency. Smaller structures are possible using multi-mode interference or more advanced taper concepts and more aggressive bend design.

3.5 Conclusions

Microphononic circuits can realize both coupled-element circuits via evanescent coupling based on embedded waveguides (analogously to dielectric integrated photonic circuits), or via physically interconnected suspended structures (closer to microwave circuits based on metal-walled microwave cavities, where the free boundary in acoustics corresponds to the perfect electric conductor wall of a microwave cavity). In this paper, we investigated the former and found that the confinement and losses are consistent with enabling micron-scale devices and circuits that operate on 1-100 GHz bandwidth signals, where the low end of frequencies is likely to be limited by device size and the high end by losses and lithographic resolution.

High-slowness-contrast embedded acoustic waveguides allow complete, radiation-free guided wave confinement in $1\,\mu$m scale cross-sections. Intrinsic material losses permit operation in the 1-100 GHz frequency range with Q's in the thousands and linewidths that permit efficient signal processing – and tens of microns to millimeters or centimeters of low loss propagation depending on frequency.

Basic building blocks based on evanescent confinement and coupling of embedded structures include waveguide bends, ring resonators, directional couplers and Y splitters that all benefit from the high slowness contrast to provide $10\,\mu$m scale structures at few-GHz frequencies, thus enabling complex multi-element circuits. We believe this kind of microphononic circuit platform, which does not require suspended components, warrants further investigation, and could provide valuable components integrable directly with microelectronics and microphotonics in CMOS as well as specialized custom chip technology.

Evanescently confined microphononic circuits could find applications in sensing, communication and RF signal processing, interfaced either to electronics or photonics. With additional attention paid to simultaneous confinement of optical and acoustic waves, applications in optomechanics, signal domain transduction, and microwave photonic signal processing could benefit. The presented study of guidance and loss supports the feasibility of such structures in dimension and frequency ranges of interest, and suggests the next steps of experimentally demonstrating these geometries. The possibility of microphononic circuits being incorporated within planar CMOS technology, could enable complex systems-on-chip that can benefit from the narrowband signal processing capabilities and long time delays enabled by confined sound waves. Investigation of some of these possibilities is a worthy subject for future work.

Chapter 4

Optomechanics in Advanced CMOS Platforms

4.1 Light Forces: Radiation Pressure and Electrostriction

Optomechanics is the study of interactions between light and mechanical motion. In micro- and nano-scale high index contrast photonic systems, strong confinement of both optical and mechanical fields makes it possible to greatly enhance these interactions, and thus enabling efficient optomechanical coupling in devices and systems for various applications, such as optical delay lines [26, 85], photonic-phononic memory [65], narrow-linewidth RF photonic filtering [92], and on-chip optomechanical signal detection [100]. A given electromagnetic field exerts optical forces on the physical structure through two different mechanisms: radiation pressure and electrostriction. Radiation pressure is a result of changes in photon momentum in emission, absorption and scattering processes. For a given electromagnetic field with electric field $\mathbf{E}$ and magnetic field $\mathbf{H}$, the radiation pressure force $\mathbf{F}^{rp}$ can be calculated by taking the gradient of the Maxwell Stress Tensor $\mathbf{T}$:

$$T_{ij} = \varepsilon(E_i E_j - \frac{1}{2}\delta_{ij}|\mathbf{E}|^2) + \mu(H_i H_j - \frac{1}{2}\delta_{ij}|\mathbf{H}|^2) \tag{4.1}$$

$$\mathbf{F}^{rp} = \nabla \cdot \mathbf{T} \tag{4.2}$$

Electrostrictive force is a consequence of the strain dependence of material permittivity ε. An electrostrictive tensor σ_{ij}^{es} can be defined in a form similar to the Maxwell stress tensor [80]

$$\sigma_{ij}^{es} = -\frac{1}{2}\varepsilon_0 n^4 p_{klij} E_k E_l \tag{4.3}$$

where p_{klij} is the photoelastic tensor, and the electrostrictive force $\mathbf{F}^{es}$ is given by

$$\mathbf{F}^{es} = -\nabla \cdot \sigma^{es} \tag{4.4}$$

Figure 4.1.1 plots the electric fields of the fundamental TE mode of a rectangular Si waveguide in air. Using Eqns. 4.1 – 4.4, $\mathbf{F}^{rp}$ and $\mathbf{F}^{es}$ are computed using the mode fields in Fig. 4.1.1a, and the results are plotted in Figs. 4.1.1b and 4.1.1c, respectively. For dielectric waveguides, $\mathbf{F}^{rp}$ exists only on material boundaries, where $\nabla\varepsilon$ is nonzero; whereas $\mathbf{F}^{es}$ exists both on material boundary and inside the waveguide core.

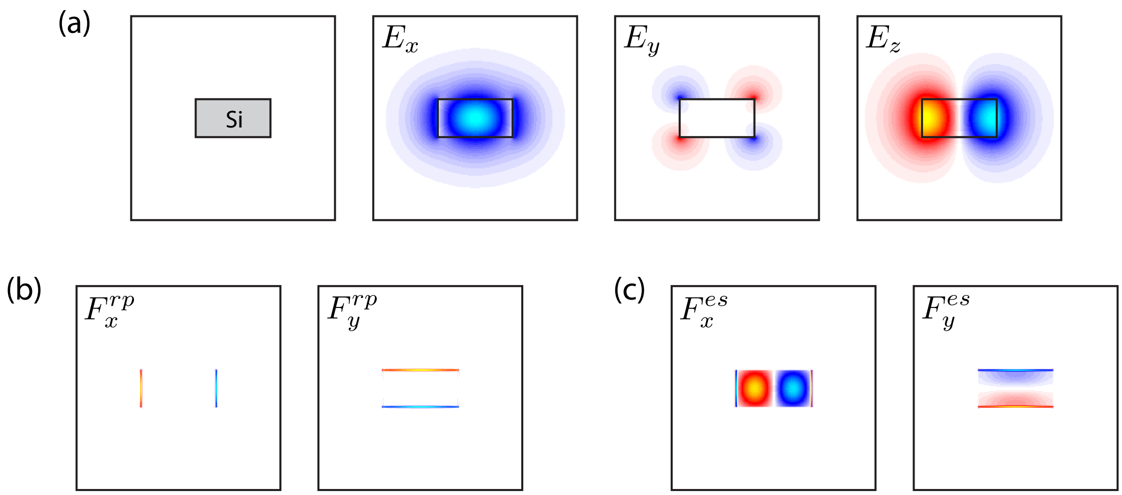

Figure 4.1.1: Optical forces in a rectangular microphotonic waveguide. (a) A rectangular Si waveguide in air and E field components (E_x, E_y and E_z) of its fundamental TE mode. (b) Radiation pressure force along x (F_x^{rp}) and y (F_y^{rp}), calculated from the E fields. (c) Electrostrictive force along x (F_x^{es}) and y (F_y^{es}), calculated from the E fields.

In this chapter, the design of optomechanical devices will be discussed. In optomechanical interactions where the mechanical motion is slow, light forces can be treated as static forces with time averaged electromagnetic fields. Chapter. 4.2 explores the maximization of radiation pressure force in a vertically coupled dual ring resonator structure through optimization of waveguide cross sectional dimensions. When the mechanical motion involved in the interaction becomes faster with a mechanical frequency Ω comparable to the optical decay rate, dynamic effects must be considered. Section 4.3 describes the coupling between modes in a triply resonant optomechanical system, with the frequency of the mechanical mode matched to the difference in frequencies of the two optical modes. Section 4.4 considers the specific challenges in building suspended optomechanical devices in a CMOS platform, introduces some initial test structures and presents on-going efforts in post processing and release of these structures.

4.2 Maximizing Radiation Pressure in Coupled Waveguides

In optically coupled optomechanical resonators, optical forces can be localized and resonantly enhanced to construct optomechanic potential wells for self alignment of cavity resonances, by controlling the position of the coupled structures [81]. This section presents the design of waveguide cross-sections that optimizes forces between suspended and evanescently coupled dual-ring resonator optomechanical cavities with a variable coupling gap. The formalism and procedure for calculating forces is described and figures of merit for optical forces evaluated. The fundamental supermodes of TE and TM polarization, each in even and odd symmetry (symmetric and anti-symmetric), are studied. The scaling of force and pressure is discussed, which shows asympototic behavior of forces at small and large gaps.

4.2.1 Formulation of Radiation Pressure Force in Coupled Cavities

In a pair of suspended and optically coupled waveguides, the optical force per unit length (L) per unit input power (P) can be obtained by computing the derivative of effective index n_{eff} of the eigenmode with respect to the separation between the waveguides g at a fixed wavenumber k [59]:

$$\frac{F}{LP} = -\frac{1}{c}\frac{n_g}{n_{eff}}\frac{\mathrm{d}n_{eff}}{\mathrm{d}g}\bigg|_k \tag{4.5}$$

where n_g is the group index of the eigenmode and c is the speed of light. Equivalently, for a resonant cavity made of suspended and coupled waveguide pair (Figure 4.2.1), the optomechanic force per unit energy inside the cavity is

$$\frac{F}{N\hbar\omega} = \frac{1}{n_g}\frac{\mathrm{d}n_{eff}}{\mathrm{d}g}\bigg|_\omega \tag{4.6}$$

where N is the number of photons inside the cavities and ω is the optical frequency. When material

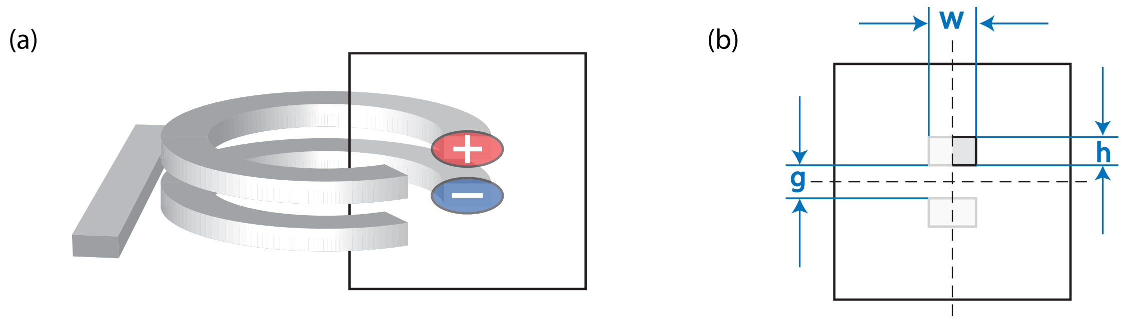

Figure 4.2.1: (a) Two vertically coupled rings suspended in air. (b) Cross-section of the suspended structure, with waveguide dimension $w \times h$ and separated by gap g. At infinite ring radius, symmetry allows the optical modes to be solved using a quarter of the structure.

indices are assumed to be constants in the computation of eigenmodes, photoelastic effect is not considered in the calculation, and the resultant F accounts only for radiation pressure force, but not electrostriction, which is the case for the analysis that follows. For each waveguide cross-section width and height combination, the slope of the group index versus gap $\mathrm{d}n_{\mathit{eff}}/\mathrm{d}g$ at $g = g_0$ can be obtained by solving for the eigenmodes of two structures with gap $g_0 - \Delta g/2$ and $g_0 + \Delta g/2$,

$$\left.\frac{\mathrm{d}n_{\mathit{eff}}}{\mathrm{d}g}\right|_{g=g_0} = \frac{1}{\Delta g}\left(n_{\mathit{eff}}|_{g=g_0+\Delta g/2} - n_{\mathit{eff}}|_{g=g_0+\Delta g/2}\right) \tag{4.7}$$

or perturbatively by taking the overlap integral using the electric field $\mathbf{E}$ and magnetic field $\mathbf{H}$ of an eigenmode at gap g and the change in permittivity $\Delta\varepsilon$ due to δg using standard perturbation theory:

$$\left.\frac{\mathrm{d}n_{\mathit{eff}}}{\mathrm{d}g}\right|_{g=g_0} = \frac{\varepsilon_0 c}{\Delta g}\left.\frac{\int(\mathbf{E}\cdot\Delta\varepsilon\cdot\mathbf{E}^*)\mathrm{d}a}{\int(\mathbf{E}\times\mathbf{H}^* + \mathbf{E}^*\times\mathbf{H})\cdot\hat{z}\mathrm{d}a}\right|_{g=g_0} \tag{4.8}$$

This formulation allows for calculation of the optical force through solving for the specific eigenmode of the unperturbed system only once. However, in structures with high refractive index contrast, since the normal component of the electric field is highly discontinuous across material interfaces, using Eqn. 4.8 to calculate force can be problematic, especially since radiation pressure force exists only on these boundaries. Reference [41] provides an expression that uses the normal component of the electric displacement field $\mathbf{D}$, which yields more accurate results for high index contrast (HIC) structures:

$$\left.\frac{\mathrm{d}n_{\mathit{eff}}}{\mathrm{d}g}\right|_{g=g_0} = \left.\frac{\varepsilon_0 c}{\Delta g}\frac{\int(\mathbf{E}_{\parallel}\cdot\Delta\varepsilon\cdot\mathbf{E}_{\parallel}^{*} - D_{\perp}\cdot\Delta\frac{1}{\varepsilon}\cdot D_{\perp}^{*})\mathrm{d}a}{\int(\mathbf{E}\times\mathbf{H}^{*}+\mathbf{E}^{*}\times\mathbf{H})\cdot\hat{z}\mathrm{d}a}\right|_{g=g_0} \tag{4.9}$$

To compare these three methods, $\mathrm{d}n_{\mathit{eff}}/\mathrm{d}g$ is calculated using Eqns. 4.7 – 4.9 for the symmetric TE supermode of two identical and vertically coupled ring resonators using a finite difference modesolver with discretizations 5nm, 10nm and 20nm, and the results are plotted in Fig. 4.2.2. Directly solving for the modes of structures with slightly different gaps (Equation 4.7) yields more accurate results than using perturbative methods, but requires solving twice the number of structures. Taking overlap integrals with an index perturbation (Eqns 4.9 and 4.8) is computationally much more efficient, and with the HIC correction (Eqn. 4.9) the results are relatively accurate. We will therefore use Eqn. 4.9 for design optimization.

4.2.2 Maximizing Radiation Pressure through Waveguide Cross-section Design

The cross-sectional dimensions of each waveguide can be designed to maximize the optical force in the dual-cavity structure for a specific eigenmode. Figure 4.2.3 shows the normalized force per unit energy computed using Eqns. 4.6 and 4.9 for TE and TM symmetric and antisymmetric modes as a function of waveguide width and height, at a fixed gap of 120nm, and the last column on the right is the analytical slab waveguide solution of the corresponding mode where the width of the waveguides is set to infinity. The sign of the force indicates its direction, with positive being repulsive force and negative being attractive.

The two symmetric supermodes (Figs. 4.2.3a and 4.2.3c) both produce an attractive force (blue) between the two waveguides. For a given width in the confined region, there is an optimum height where the optical force is maximized (dark blue). The antisymmetric supermodes (Figs. 4.2.3b and 4.2.3d) produce a repulsive force (orange) between the two waveguides. In the TE symmetric mode (Fig. 4.2.3b), maximum optical force is produced when the waveguide height is close to cutoff (dark red). The gray region Fig. 4.2.3d is due to the coupling between the TM_{11} antisymmetric mode and the TE_{21} symmetric mode, resulting in a hybrid supermode, and the

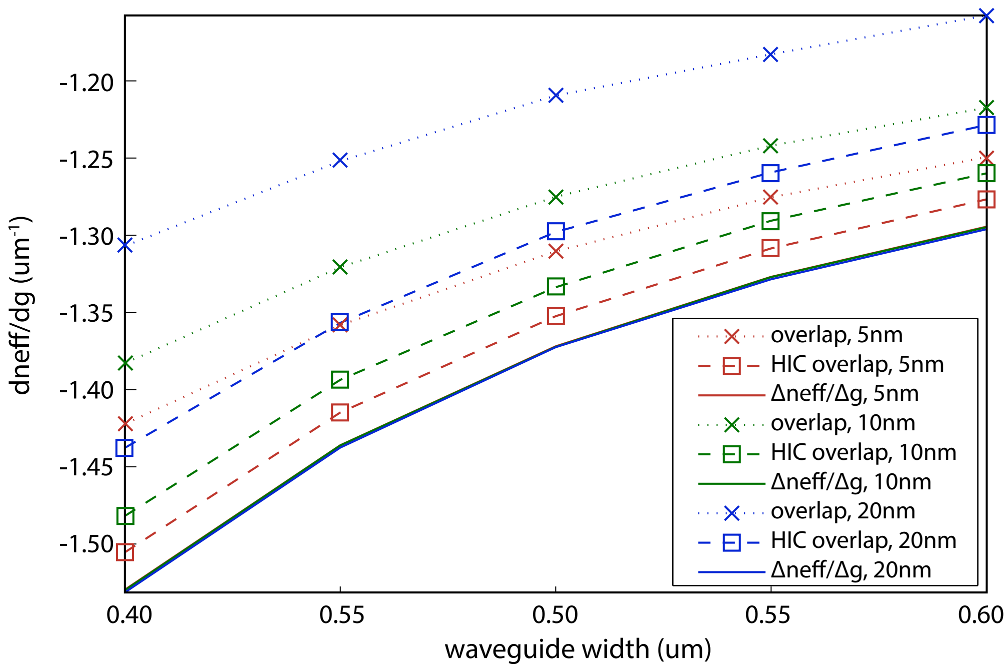

Figure 4.2.2: Comparison between different methods for calculating $\mathrm{d}n_{eff}/\mathrm{d}g$ for the symmetric TE supermode of two vertically coupled identical ring resonators with height = 220nm and gap = 120nm. Solid lines: directly solving for eigenmodes of two structures with gap $\pm\Delta g/2$ (Eqn. 4.7); crosses: standard overlap integral (Eqn. 4.8); squares: overlap integral with high index contrast correction (Eqn. 4.9). Colors represent different discretization used in finite difference modesolver. Red: 5nm; green: 10nm; blue: 20nm.

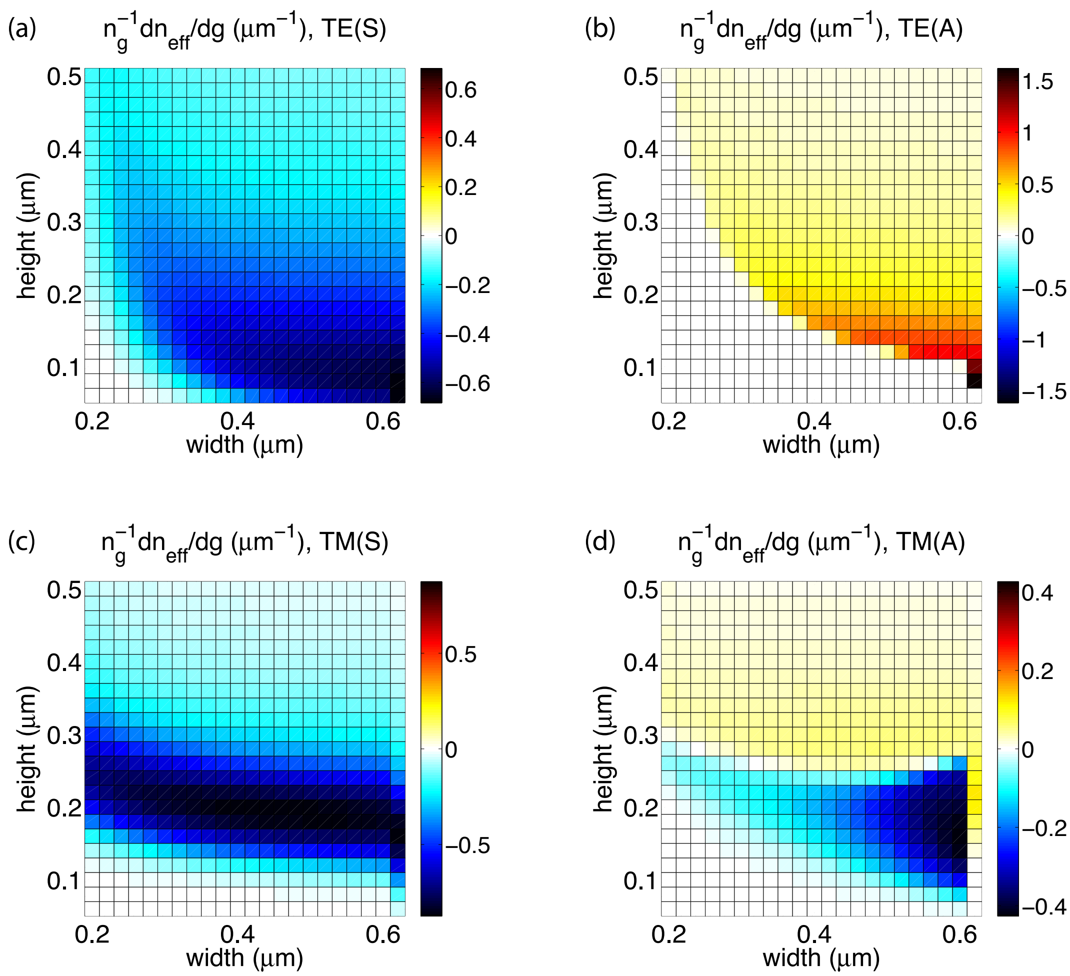

Figure 4.2.3: Force per unite energy in a dual ring structure with different waveguide cross-section for (a) symmetric TE mode, (b) antisymmetric TE mode, (c) symmetric TM mode and (d) antisymmetric TM mode, gap between the two rings is fixed at 120nm. Last column in each plot represents two coupled slab waveguides with infinite waveguide width. Positive: repulsive force; negative: attractive force.

maximum repulsive optical force is approximately an order of magnitude smaller than that of the TE antisymmetric mode.

To study the effect of vertical gap between the two rings, Fig. 4.2.4 plots the normalized optical force between two slabs (infinite waveguide width) per unit energy for different slab thickness (waveguide height) and gap. For both the TE and TM symmetric supermodes (Figs. 4.2.4a and 4.2.4c), there exists an optimal height where the optical force is greatest, and the gap between the two slabs needs to be small to maximize the force. The TE antisymmetric force produces a large repulsive force when the waveguide height and gap are close to cutoff of the mode (light blue region in Figure 4.2.4b). Force in the TM antisymmetric mode (Fig. 4.2.4d) is least sensitive to variation in the gap, and the magnitude is significantly smaller compared to the other three cases. Figure 4.2.5 shows the effect of waveguide gap on maximum optical force. The solid lines are the maximum force for each gap (maximum value of each row from Fig. 4.2.4), and the dotted lines plot optical force vs. gap for the optimum waveguide height (one column from Fig. 4.2.4 where the waveguide height gives the overall maximum force for that mode). The force from the two TE modes grow rapidly as the gap between the two waveguides decreases.

Another consideration for designing the cross section of the waveguides is the confinement of the optical modes. Figure 4.2.6 plots the contour of minimum radius required for a single ring to achieve a given Q of 10^5, 10^6 and 10^7, with each waveguide width and height combination. In general, at a smaller waveguide width/height, a larger radius is needed to achieve the same Q; and for a cross section with waveguide width larger than height, TM is less well confined than TE and thus requires a larger radius to achieve the same Q. Comparing with Figure 4.2.3, the TE symmetric and antisymmetric supermodes can produce a reasonable force in rings of a radius smaller than 10μm at a height around 100nm and 200nm respectively. The TM symmetric supermode is relatively insensitive to changes in waveguide width, and the force peaks around a waveguide height of 200nm. The symmetric supermode will have better confinement than the fundamental TM mode in a single ring. The antisymmetric TM supermode is less usable because of its poor confinement requiring a large radius.

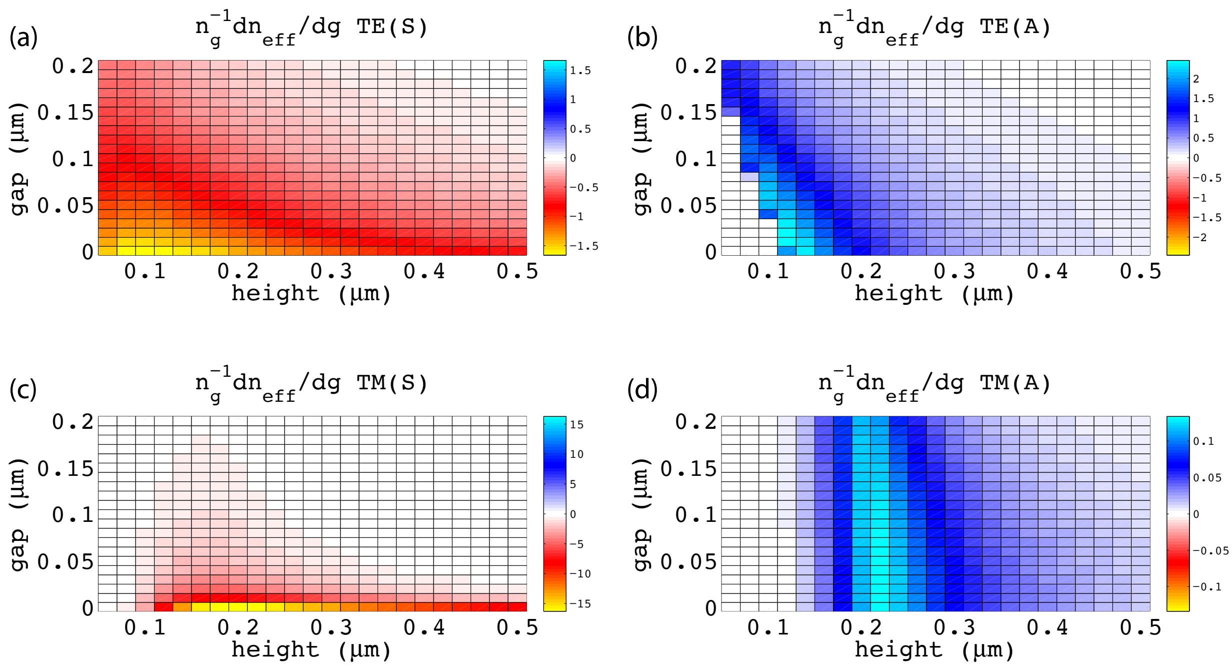

Figure 4.2.4: Force per unite energy in a dual slab structure with different waveguide height (slab thickness) and gap for (a) symmetric TE mode, (b) antisymmetric TE mode, (c) symmetric TM mode and (d) antisymmetric TM mode.

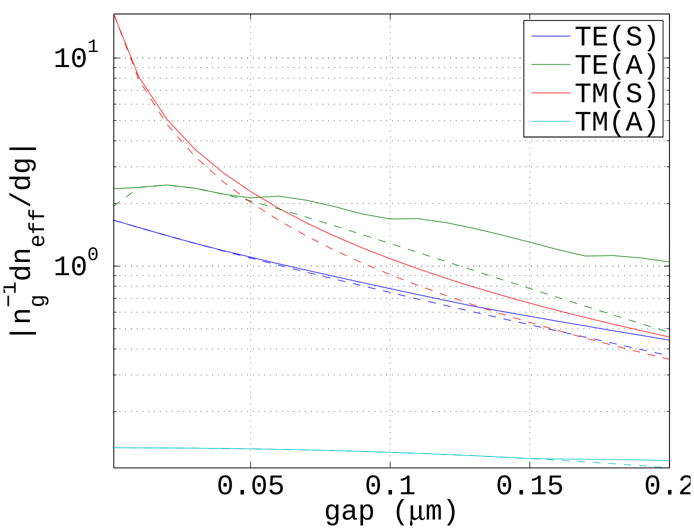

Figure 4.2.5: Magnitude of force per unite energy in a dual slab structure. Solid line: maximum optical force vs. gap, dotted line: force vs. gap for the optimal waveguide height, where overall maximum force is achieved. c.f. Fig. 4.2.4.

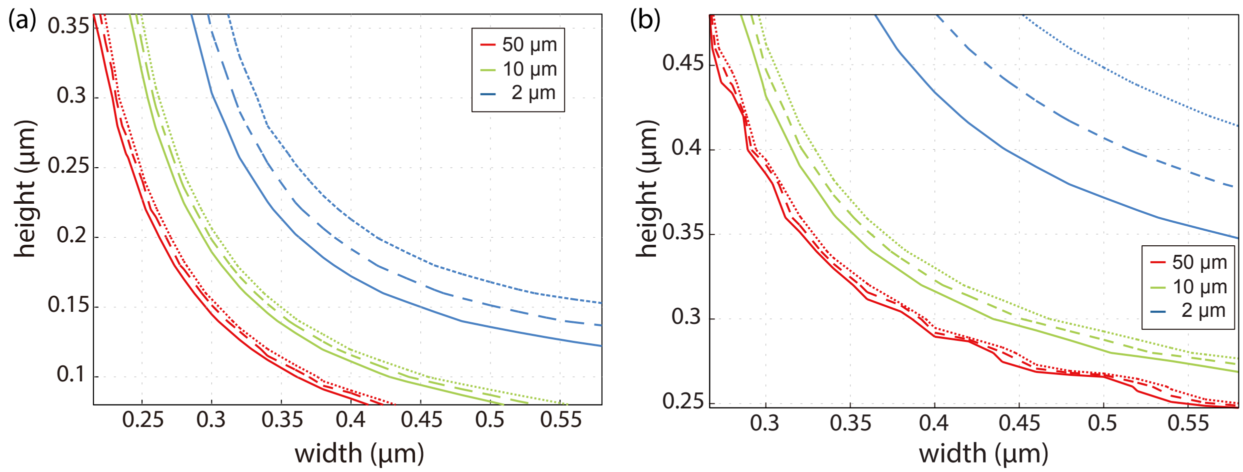

Figure 4.2.6: Contour plot of minimum radius required for a single ring to achieve given Q values. Solid lines: 10^5; dashed lines: 10^6; dotted lines: 10^7 for (a) TE and (b) TM mode.

4.3 Stimulated Brillouin Scattering in Wiggler Resonators

In contrast to the static scenario discussed in Sec. 4.2, the dynamic effects of optomechanics are primarily considered in systems where both the optical and mechanical decay rates are low. When phonons in a mechanical mode interact with photons in the same optical cavity mode, optomechanical dynamic backaction occurs as a consequence of the modification of the mechanical system due to the presence of optical field through optical forces, and manifests itself in the forms of mechanical amplification and cooling [47]. An optical pump at frequency ω interacts with a mechanical mode at Ω and generates two motional sidebands at $\omega \pm \Omega$, which are asymmetrically enhanced in the cavity if ω is detuned from the cavity resonance. This asymmetry leads to a nonzero net energy flow between the optical and mechanical modes, which results in amplification or cooling, depending on the direction of the flow.

It is possible to have more than one optical (or mechanical) cavity mode to participate in the optomechanical interaction [4]. Stimulated Brillouin Scattering (SBS) is one such example, conventionally studied in the context of fiber optic systems, where the guided optical modes couple to guided phonon modes through electrostrictive force. [82]

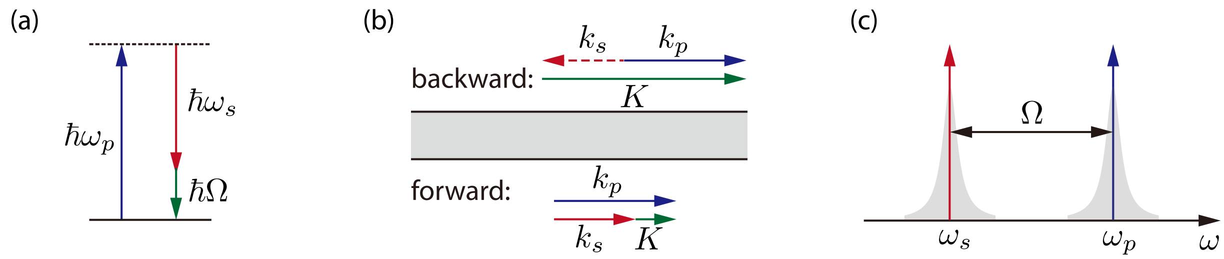

Figure 4.3.1: Stimulated Brillouin Scattering. (a) Energy conservation in SBS. Frequencies of the pump and stokes optical modes and that of the mechanical mode must satisfy $\omega_p = \omega_s + \Omega$. (b) Momentum matching in SBS in a waveguide. Wavevectors of the pump and stokes optical modes and that of the mechanical mode must satisfy $\mathbf{k}_p = \mathbf{k}_s + \mathbf{K}$. (c) SBS in a resonator.

For two optical modes and a mechanical mode with frequencies ω_p, ω_s and Ω, and propagation constants $\mathbf{k}_p$, $\mathbf{k}_s$ and $\mathbf{K}$, phase matching requires conservation of both energy $\hbar\omega_p = \hbar\omega_s + \hbar\Omega$ and momentum $\mathbf{k}_p = \mathbf{k}_s + \mathbf{K}$ (Fig. 4.3.1). In a waveguide setting (Fig. 4.3.1a), since the structure supports a continuum of frequencies for both optical and mechanical waves, exact phase matching can be achieved in design by intersecting the Ω vs. $|\mathbf{K}|$ dispersion curve of the mechanical mode and $(\omega_p - \omega_s)$ vs. $|\mathbf{k}_p - \mathbf{k}_s|$ for the two optical modes. In the case of a resonator (Fig. 4.3.1c), three discrete modes need to simultaneously satisfy the same phase matching conditions. Momentum matching requires that the azimuthal mode order (number of wavelengths around the resonator) must equal to the difference between the azimuthal mode orders of the optical modes. To satisfy energy conservation, since frequencies of the optical modes ($\sim 193\,\mathrm{THz}$) are much higher than that of the mechanical mode, the optical modes need to be close to degenerate.

In the design of the passive wiggler resonators described in detail in Sec. 2.4, degenerate optical modes of an unperturbed ring resonator are radiatively coupled by azimuthally periodic contacts that are phase matched to the difference in azimuthal mode orders of the optical modes. The same geometry can be used to construct an optomechanical system, where two eigenmodes of an unperturbed ring resonator with different radial and azimuthal modes can be coupled through SBS by a mechanical mode of the same structure.

A suspended ring resonator supports different types of mechanical modes. Figure 4.3.2 shows resonant frequencies and displacement fields of out-of-plane flexural (OP), in-plane flexural (IF) and radial contour (RC) modes of different radial and azimuthal orders, simulated in 3D using the Solid Mechanics module in COMSOL.

4.4 Optomechanics in Advanced CMOS

4.4.1 Challenges in Building Optomechanics in CMOS

Complementary metal-oxide-semiconductor (CMOS) is a modern technology capable of building densely integrated circuits on a very large scale. Designing photonic and optomechanical devices to be truly CMOS-compatible allows one to leverage the well invested and established manufacturing infrastructure of CMOS electronics, and to enable scalable fabrication of photonic and optomechanical devices at an affordable cost. Recent experiments have demonstrated optical communication links between processor and memory in an advanced and unmodified commercial CMOS process [98]. However, the small thicknesses in a CMOS material layer stack pose unique challenges in device design and post processing.

For good optical confinement, the thickness of buried oxide (BOX) between the Si device layer and the Si substrate must be large enough to prevent leakage of the guided power into the substrate. In conventional photonic silicon-on-insulator (SOI) platforms, BOX thickness is on the order of a couple microns [94], while in typical CMOS processes BOX is much thinner, allowing guided optical modes to evanescently couple into bulk modes in the Si substrate underneath and resulting in significant propagation loss. Using an optical eigenmode solver, substrate leakage can be calculated by solving for the complex propagation constants of different modes with perfectly matched layer (PML) placed on the bottom of the computation domain – optical power leaked into the Si substrate is then absorbed by the PML and reflected in the imaginary part of the complex propagation constant. Propagation loss in dB per cm is given by

$$L_{\mathrm{dB/cm}} = 0.2\alpha \log_{10} e \tag{4.10}$$

where α is the imaginary part of the propagation constant.

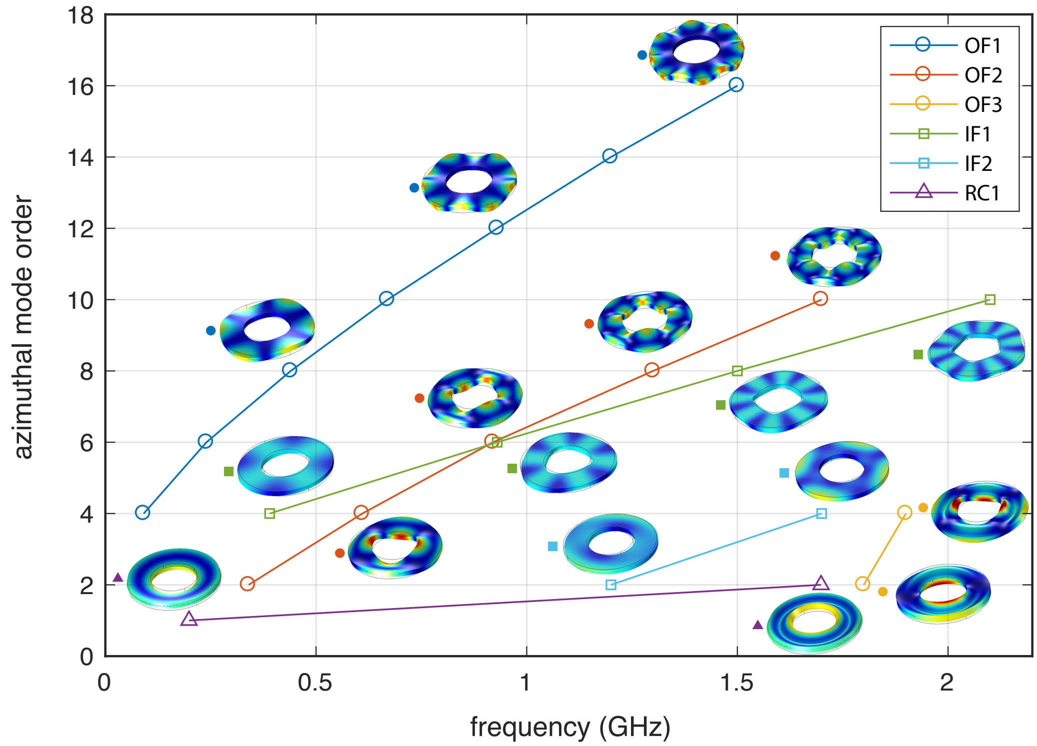

Figure 4.3.2: Resonant frequencies and displacement fields of various mechanical modes of a silicon ring resonator with outer radius 2.04 μm, waveguide width 1.02 μm and height 220 nm, simulated using the Solid Mechanics module of COMSOL. OF1-3: out-of-plane flexural modes with radial order 1-3; IF1-2: in-plane flexural modes with radial order 1-2; RC1: 1st radial order radial contour mode.

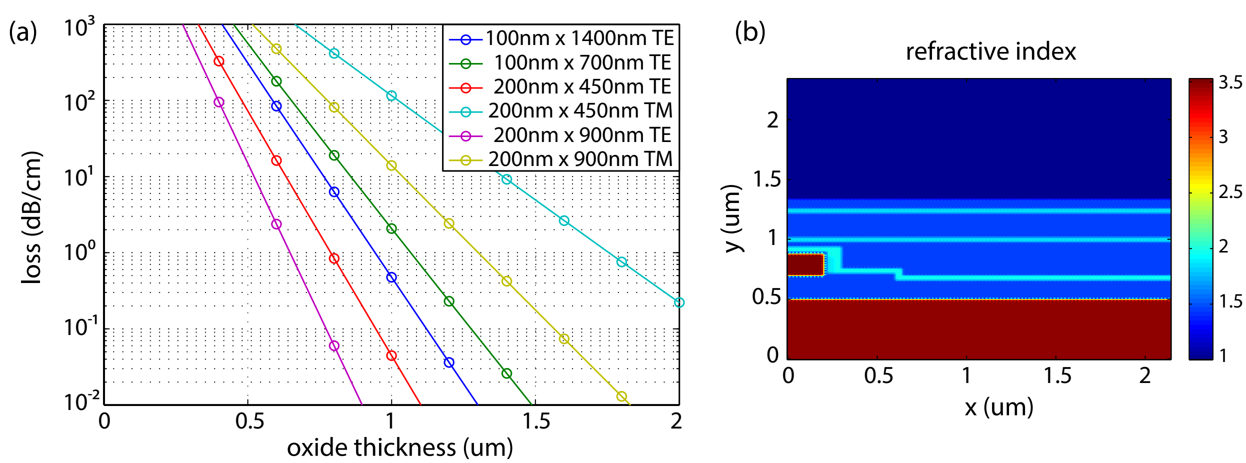

Figure 4.4.1: Substrate leakage in photonic waveguides in a CMOS process. (a) Propagation loss at 1565 nm for fundamental TE and TM modes in waveguides with different cross-sectional dimensions vs. thickness of buried oxide (BOX). (b) Cross-sectional refractive index distribution of half a waveguide in a typical CMOS process.

Figure 4.4.1a plots the propagation loss in dB/cm for fundamental TE and TM modes at 1565 nm, in waveguides with different cross-sectional dimensions, in a typical CMOS process with a material layer stack index profile as plotted in Fig. 4.4.1b. $L_{\mathrm{dB/cm}}$ increases exponentially as BOX thickness becomes smaller. At a BOX thickness larger than $2\,\mu$m, propagation losses for the different modes are well below a fraction of a dB per cm. However, as BOX thickness decreases below $0.5\,\mu$m, as is in the case of most existing CMOS processes, additional post-processing steps, such as local removal of the Si substrate under optical devices [37], are needed to re-enable optical confinement in the Si device layer.

In order to have mechanical confinement in the same platform, one possible scheme is to suspend Si structures, so the mechanical displacement fields are confined within the solid-air interfaces. Compared to conventional photonic SOI processes, suspending devices in a CMOS process generally requires enabling release in a much more complex material stack. The added complexity is manifold: 1) removal of multiple materials (e.g. SiO_2, SiN) may be required, 2) front end electronic layers must all be protected during the etch process, and 3) if Si substrate is removed to enable optical confinement, the chip to be etched would have a total thickness of a couple tens of microns, and become mechanically very fragile. Despite these difficulties, designing mechanical waveguides and resonators in CMOS processes is still a worthwhile pursuit, not only because of the existing manufacturing infrastructure, but also for the relative ease of accessing high speed electronics, potentially for driving and detection.

Contacted photonic waveguides and resonators, as discussed in detail in Chapter 2, are promising candidates for having simultaneous optical and mechanical confinement. The ability to attach suspended resonators to coupling bus waveguides provides one additional advantage of enforcing the designed coupling strength, by minimizing the change in coupling gap even in the presence of compressive and tensile stress in material layers, which would otherwise lead to structural deformation such as buckling of suspended waveguides. For microdisks for disk-like resonators based on whispering galley modes, metal vias and contacts could potentially serve as pedestals to enable suspension as well. Alternatively, evanescently confining acoustic waveguides as discussed in Chapter 3 could be designed in Si-based CMOS platforms to realize mechanical confinement without air suspension.

4.4.2 Proposed Post-processing Flow for Suspended Optomechanical Devices

Post-processing of suspended Si optomechanical devices in CMOS processes include three main tasks: Si substrate removal, device release and packaging. Si substrate removal is necessary not only to prevent optical substrate leakage, but also to allow etch access to the device layer from the back of the chip. In uncladded photonic devices fabricated in a conventional photonic SOI process, such as the wiggler resonators discussed in Section 2.4, the Si device layer is exposed and SiO_2 under the devices to be suspended can be directly removed in a selective wet etch step using BOE. In a CMOS or CMOS-like process, the Si device layer is vertically cladded by a stack of material layers on both sides – on the top, the front end of line (FEOL) layers contain metal contacts and vias that must be protected, so the only option is to locally or globally remove the Si substrate and BOX under the Si devices, and then proceed with device release.

To completely remove the bulk Si substrate, a combination of three methods can be used. Figures 4.4.2a–c describe the proposed process flow for Si substrate removal in suspended optomechanical devices. A fabricated chip is bonded to a glass slide upside down, with the Si substrate facing upward (Fig. 4.4.2b). The glass slide acts as a temporary handle substrate, and crystalbond seals the sides of the chip so only the bottom most layer is exposed during each process step, and the back end metals and dielectrics stay protected. As a first Si thinning step, chemical mechanical polishing (CMP) can quickly thin down the Si substrate to a thickness of $\sim 50\,\mu$m (Fig. 4.4.2b), at which point the chip becomes mechanically fragile and cracking can easily occur. In addition to being relatively fast and low cost, CMP involves a mechanical action which is not material selective, so adhesive (e.g. crystalbond) used for bonding and for protecting the sides of the chip can be planarized in the same step, which is desired for the photolithography steps in device release. To remove the remaining Si, reaction ion etch (RIE) followed by xenon difluoride (XeF_2) can be used. XeF_2 is a gas-phase etch which has an excellent selectivity of 1000:1 for Si vs. SiO_2 [108]. However, it has a severe loading effect, and the etch rate can drop below 11 nm/min for larger samples [9, 109], making it unsuitable for blanket removal of large and thick Si substrates. RIE uses sulfur hexafluoride (SF_6) and oxygen (O_2) plasma to remove Si with a etch rate around 1500 nm/min, and has a selectivity of 150:1 vs. SiO_2 [108]. Compared to XeF_2, RIE has better etch rate and overall uniformity, but worse selectivity and surface roughness. To take advantage of both methods, good results can be achieved by using RIE to thin down the Si substrate to $\sim 5\,\mu$m, followed by a quick slight over etch with XeF_2 to completely remove the remaining Si.

Figures 4.4.2d–g show the proposed flow for device release after substrate removal. A photoresist layer can be deposited on the back side of the BOX layer which is exposed after Si substrate removal (Fig. 4.4.2d), and lithography can be used to define etch windows (Fig. 4.4.2e). One practical difficulty is that the crystalbond sealing the sides would be slightly taller than chip surface after substrate removal, creating challenges in resist deposit as well as mask alignment. Immersion in acetone may be required prior to photoresist deposit, and crystalbond can be reapplied after resist development (Fig. 4.4.2e). BOX can be removed through wet etch with buffered oxide hydrofluoric acid (BOE) (Fig. 4.4.2f). SiN liners are often present in CMOS processes between the Si device layer and BEOL inter layer dielectrics. Depending on the type of SiN, BOE may be sufficient to remove both BOX and SiN in a single step [108], or one additional wet etch step with phosphoric acid (H_3PO_4) may be needed (Fig. 4.4.2g). Photoresist residue can be removed with IPA followed by critical point drying.

After device release, passive devices would be already functional, if the chip allows photonic access through the back side, e.g. through vertical grating couplers. To allow access to the electrodes on the front side for active devices, the chip needs to be transferred to a second handle substrate by bonding the back side of the chip to a glass substrate with optical adhesive (Fig. 4.4.2h), after which any remaining crystalbond residue can be removed with acetone. The substrate transferred chip can be further soldered to a printed circuit board (Fig. 4.4.2i) to complete the packaging step.

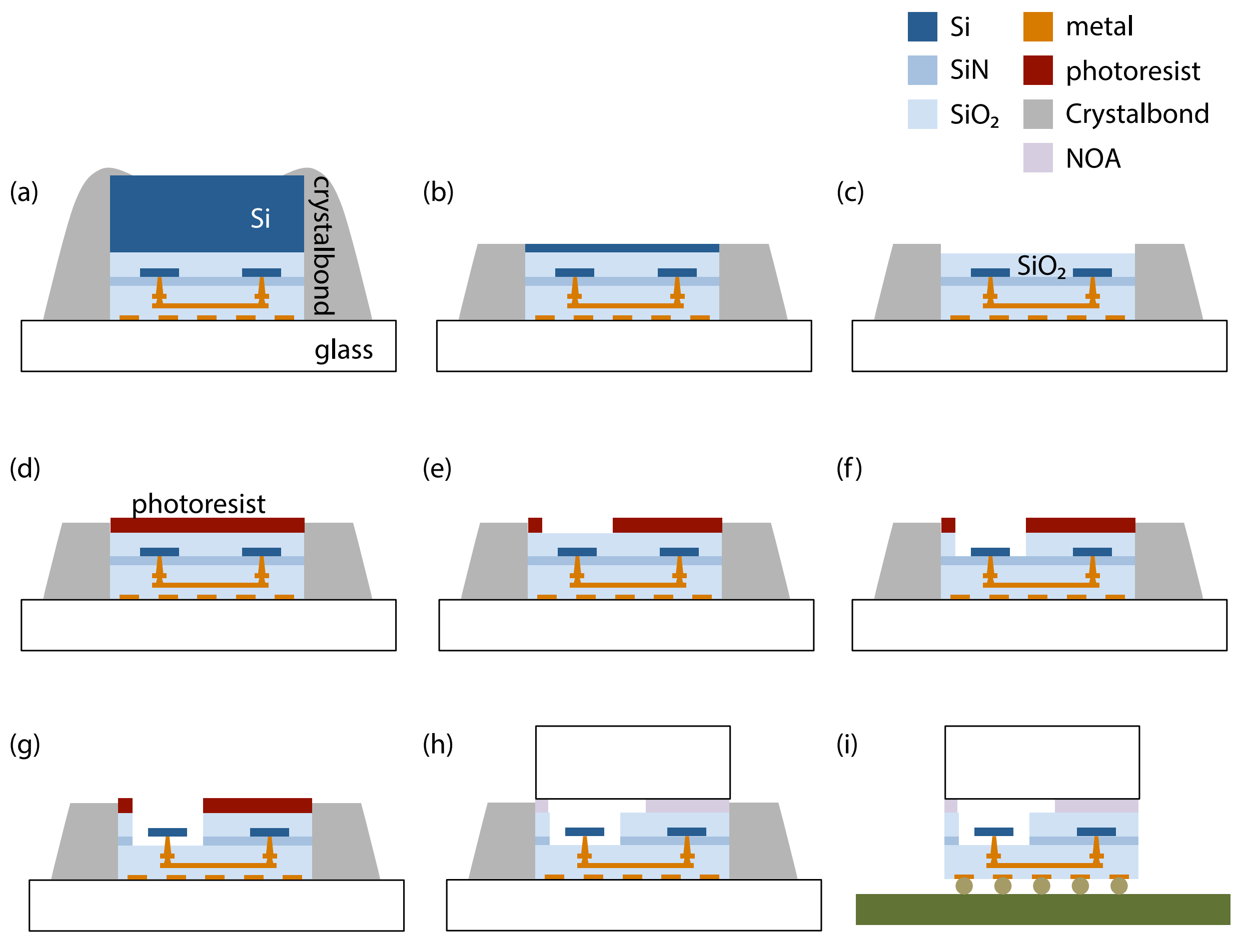

Figure 4.4.2: Proposed post-processing flow for suspending optomechanical devices in CMOS processes. (a) Mount fabricated chip on glass slide with crystalbond. (b) Remove $\sim 200\,\mathrm{um}$ of Si through chemical mechanical polishing (CMP). (c) Remove remaining Si using reactive ion etching (RIE) and/or XeF_2 dry etch. (d) Apply photoresist. (e) Define etch windows through photolithography. (f) Selectively remove SiO_2 with buffered oxide etch (BOE). (g) If SiN is resistant to BOE, remove SiN with phosphoric acid. (h) Encapsulate with glass and optical epoxy (NOA). (i) Remove crystalbond and glass substrate, and solder to printed circuit board (PCB).

4.4.3 On-going Efforts in CMOS Optomechanics

As an initial step toward the integration of suspended optomechanical resonators in a zero-change commercial CMOS microelectronics process, a couple different geometries were designed and fabricated in IBM's 45nm CMOS process. Figure 4.4.3a shows the layout of the test structures, and the resonator structures include a passive optomechanical wiggler resonator (Fig. 4.4.3b) and an active whispering gallery mode disk-like resonator. Both types of resonators are to be suspended following the steps proposed in 4.4.2. The wiggler resonators would be mechanically connected to the coupling waveguides, and the disk resonators would make use of the electrical vias connected to the center of the structure as pedestals.

Different methods for removing the silicon substrate are investigated (Fig. 4.4.2a-c) and discussed in more detail in Section B.2. Further development on selective removal of cladding material for device suspension and on packaging of suspended chips is still on going.

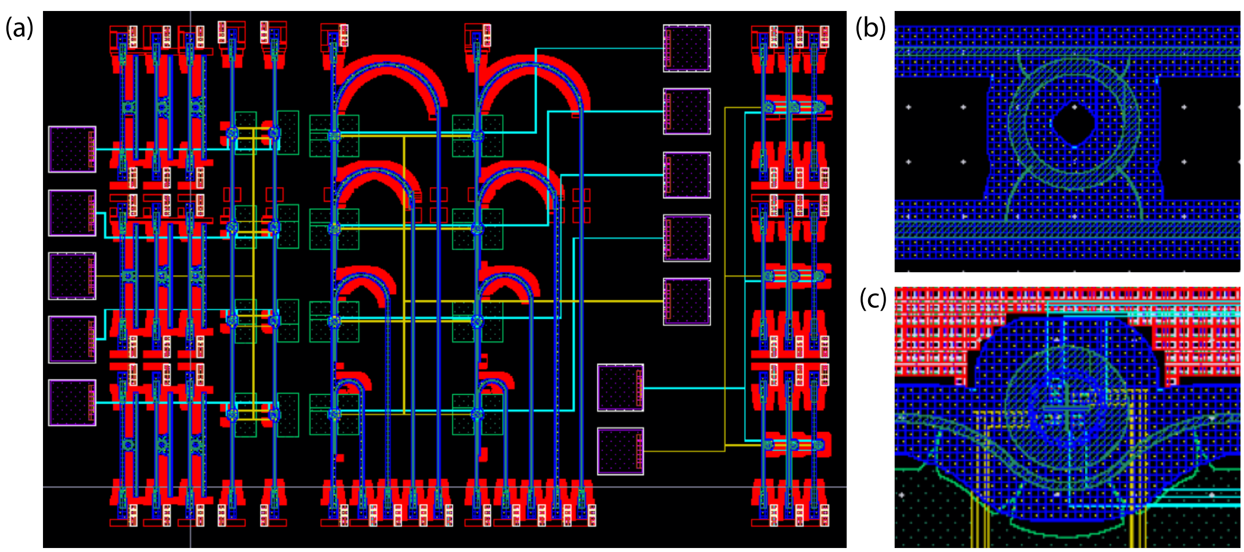

Figure 4.4.3: Layout of optomechanical devices designed and fabricated in a 45nm zero-change CMOS process. (a) Full testsite. (b) Optomechanical wiggler resonators. (c) Tunable disk filters.

Chapter 5

Conclusion

5.1 Summary of Major Achievements

Silicon photonics has seen continued rapid development over the past decade, with a growing need to make photonic devices and circuits densely integrable and directly interfaceable with CMOS microelectronics. Optomechanics is a cross-disciplinary field that has greatly benefited from the expanded design freedoms in chip-scale platforms. The work in this thesis explored various topics in photonics, acoustics and optomechanics, in an effort toward building devices that are monolithically integrable in advanced CMOS platforms. Toward this goal, a new method for designing contacted photonic structures with low scattering loss was presented and experimentally demonstrated, enabling suspension of waveguides and resonators; evanescent confinement and wave guiding was theoretically investigated in silicon-based materials, confirming the possibility of building integrated acoustic and optomechanical circuits in solid materials without device suspension; initial designs of optomechanical devices in integrated SOI platforms were described, with post-processing fabrication steps proposed and current progress presented.

The ability to attach physical contacts to photonic waveguides and resonators with low scattering loss allows these devices to be selectively suspended while staying connected to other structures in the silicon device layer for mechanical support. Loss avoidance based on imaginary coupling of modes was achieved by designing the physical contacts to radiatively couple two unperturbed eigenmodes of system without contacts, and form a supermode with an intensity pattern that spatially avoids the scattering contacts. Ring resonators with periodic contacts on the outer circumference, named the "wiggler" resonators, were designed based on this concept and fabricated in a 220 nm SOI process. Oxide-cladded wiggler resonators with center radius 3.4 μm and 6 contacts had Q factors experimentally measured up to $258,000$, and air-cladded wiggler resonators with center radis 1.5 μm and 4 contacts were selectively suspended in post-processing and sustained Q factors up to $139,000$. The same loss avoidance mechanism also has applications in non-suspended integrated photonic devices. A broadband monolithic linear waveguide crossing array was designed and experimentally demonstrated with record low loss of 0.04 dB/crossing.

As an alternative suspending lithographically defined structures in post processing, evanescent confinement of acoustic waves was theoretically investigated. Material intrinsic loss calculations and waveguide simulations show that micron-scale acoustic devices and circuits operating in the $1 - 100$ GHz frequency range can be implemented in silicon-based integrated platforms with Q's in the thousands, and the high slowness contrast between silicon and its oxide provides tight confinement of fields to allow 10-μm scale structures at few-GHz frequencies, including waveguide bends, ring resonators, directional couplers and Y splitters, which can be used as basic building blocks to form complex microphonotnic circuits on a chip, in addition to potentially enabling co-confinement of acoustic and optical fields for efficient optomechanical interactions in non-suspended structures.

Optimization of static radiation pressure through waveguide design in a vertically coupled dual ring structure through waveguide design was presented based on calculations using simulated optical fields. Integration of suspended SBS-based optomechanical devices in zero-change CMOS microelectronics platforms was discussed. Post-processing of suspended optomechanical devices fabricated in a zero-change CMOS process require 1) removal of the silicon substrate to prevent leakage of optical fields due to insufficient oxide thickness, and 2) selective removal of cladding dielectrics surrounding the structures to be suspended. A complete process flow was proposed, and a method for substrate removal was developed using a combination of chemical mechanical polishing (CMP), deep reactive ion etch (DRIE) and XeF_2 dry etch for silicon removal, and crystalbond for protecting the photonic and electronic layers during the various polishing and etch steps.

5.2 Remaining Challenges and Future Work

Post-processing fabrication still remains a big challenge in the construction of suspended optomechanical devices on a chip. After substrate removal, suspension/release of structures relies upon the ability to pattern etch windows and to selectively remove cladding materials surrounding the silicon structures. The two proposed suspension schemes – wiggler resonator based geometries where the suspended structures are physically connected to coupling waveguides or uncoupled silicon region through contacts, and disk-like whispering gallery mode resonators with electrical vias serving as pedestals – are both realizable in principle, but still require much experimental development to solve the many likely practical issues. For instance, after substrate removal, excess crystalbond extruding above the top surface of the chip may pose problems for depositing a uniform layer of photoresist; etch resistance of the electrical vias to various etchants, and mechanical stability of suspended silicon structures supported by electrical vias are yet to be experimentally tested; presence of compressive and tensile material layers could lead to deformation of suspended structures.

A different route to building CMOS compatible optomechanical devices is using material slowness contrast based evanescent guiding of acoustic waves as pointed out in Chapter 3, which doesn't require any post-processing fabrication. Between Si and SiO_2, Si is the optically slower material with the higher optical index of refraction, but acoustically SiO_2 is the slower material. To simultaneously confine optical and acoustic waves using these two materials readily available in CMOS processes, different geometries can be explored, such as a slot waveguide with a SiO_2 strip between two Si strips, where both optical and acoustic fields can be designed to be localized in the SiO_2 region. In addition to optomechanics, on-chip microphotonic devices and circuits by itself is an interesting direction for further research as well. Potential applications include sensing, communication and RF signal processing.

Bibliography

[1] Robert Aigner. MEMS in RF-filter applications: thin film bulk-acoustic-wave technology. TRANSDUCERS'05. The 13th International Conference on, 1:5–8, 2005.

[2] AI Akhiezer. On the sound absorption in solids. Journal of Physics (USSR), 1:277, 1939.

[3] Orson L Anderson. The grüneisen ratio for the last 30 years. Geophysical Journal International, 143(2):279–294, 2000.

[4] Markus Aspelmeyer, Tobias J Kippenberg, and Florian Marquardt. Cavity optomechanics. Reviews of Modern Physics, 86(4):1391, 2014.

[5] Bertram Alexander Auld. Acoustic fields and waves in solids, volume 1. John Wiley & Sons, 1973.

[6] Bertram Alexander Auld. Acoustic fields and waves in solids, volume 2. RE Krieger, 1990.

[7] Farrokh Ayazi, Logan Sorenson, and Roozbeh Tabrizian. Energy dissipation in micromechanical resonators. SPIE Defense, Security, and Sensing, page 803119, 2011.

[8] Mahmood Bagheri, Menno Poot, Mo Li, Wolfram PH Pernice, and Hong X Tang. Dynamic manipulation of nanomechanical resonators in the high-amplitude regime and non-volatile mechanical memory operation. Nature nanotechnology, 6(11):726–732, 2011.

[9] Behraad Bahreyni and C Shafai. Investigation and simulation of xef 2 isotropic etching of silicon. Journal of Vacuum Science & Technology A: Vacuum, Surfaces, and Films, 20(6):1850–1854, 2002.

[10] Krishna C Balram, Marcelo I Davanço, Jin Dong Song, and Kartik Srinivasan. Coherent coupling between radiofrequency, optical and acoustic waves in piezo-optomechanical circuits. Nature Photonics, 2016.

[11] Christopher Batten, Ajay Joshi, Jason Orcutt, Anatol Khilo, Benjamin Moss, Charles W Holzwarth, Miloš A Popovic, Hanqing Li, Henry I Smith, Judy L Hoyt, et al. Building many-core processor-to-dram networks with monolithic cmos silicon photonics. IEEE Micro, 29(4), 2009.

[12] Ari Ben-Menahem and Sarva Jit Singh. Seismic waves and sources. Springer Science & Business Media, 2012.

[13] Przemek J Bock, Pavel Cheben, Jens H Schmid, Jean Lapointe, André Delâge, Dan-Xia Xu, Siegfried Janz, Adam Densmore, and Trevor J Hall. Subwavelength grating crossings for silicon wire waveguides. Optics express, 18(15):16146–16155, 2010.

[14] Wim Bogaerts, Pieter Dumon, Dries Van Thourhout, Dirk Taillaert, Patrick Jaenen, Johan Wouters, Stephan Beckx, Vincent Wiaux, and Roel G Baets. Compact wavelength-selective functions in silicon-on-insulator photonic wires. IEEE Journal of Selected Topics in Quantum Electronics, 12(6):1394–1401, 2006.

[15] Vladimir Borisovich Braginsky, VP Mitrofanov, Vladimir Ivanovich Panov, and Cynthia Eller. Systems with small dissipation. University of Chicago Press, 1985.

[16] Jay Brotz. Damping in CMOS-MEMS resonators. Masters Project Report in ECE. Carnegie Mellon University, 2004.

[17] RJ Bruls, HT Hintzen, G de With, R Metselaar, and JC van Miltenburg. The temperature dependence of the Grüneisen parameters of MgSiN2, AlN and β-Si3N4. Journal of Physics and Chemistry of Solids, 62(4):783–792, 2001.

[18] Colin K Campbell. Applications of surface acoustic and shallow bulk acoustic wave devices. Proceedings of the IEEE, 77(10):1453–1484, 1989.

[19] Jasper Chan, TP Mayer Alegre, Amir H Safavi-Naeini, Jeff T Hill, Alex Krause, Simon Gröblacher, Markus Aspelmeyer, and Oskar Painter. Laser cooling of a nanomechanical oscillator into its quantum ground state. Nature, 478(7367):89–92, 2011.

[20] SA Chandorkar, M Agarwal, R Melamud, RN Candler, KE Goodson, and TW Kenny. Limits of quality factor in bulk-mode micromechanical resonators. MEMS 2008. IEEE 21st International Conference on, pages 74–77, 2008.

[21] Hui Chen and Andrew W Poon. Low-loss multimode-interference-based crossings for silicon wire waveguides. IEEE photonics technology letters, 18(21):2260–2262, 2006.

[22] WC Chew. Electromagnetic theory on a lattice. Journal of Applied Physics, 75(10):4843–4850, 1994.

[23] Marcus S Dahlem, Charles W Holzwarth, Henry I Smith, Erich P Ippen, and Miloš A Popović. Dynamical slow light cell based on controlled far-field interference of microring resonators. In Integrated Photonics Research, Silicon and Nanophotonics, page IMC4. Optical Society of America, 2010.

[24] Nathan Dostart, Yangyang Liu, and Miloš A Popović. Acoustic waveguide eigenmode solver based on a staggered-grid finite-difference method. Scientific reports, 7(1):17509, 2017.

[25] AE Duwel, Jeff Lozow, Christopher J Fisher, Terese Phillips, Roy H Olsson, and Marc Weinberg. Thermal energy loss mechanisms in micro-to nano-scale devices. SPIE Defense, Security, and Sensing, pages 80311C–80311C, 2011.

[26] Kejie Fang, Matthew H Matheny, Xingsheng Luan, and Oskar Painter. Optical transduction and routing of microwave phonons in cavity-optomechanical circuits. Nature Photonics, 2016.

[27] NB Feilchenfeld, FG Anderson, T Barwicz, S Chilstedt, Y Ding, J Ellis-Monaghan, DM Gill, C Hedges, J Hofrichter, F Horst, et al. An integrated silicon photonics technology for o-band datacom. In Electron Devices Meeting (IEDM), 2015 IEEE International, pages 25–7. IEEE, 2015.

[28] Tatsuhiko Fukazawa, Tomohisa Hirano, Fumiaki Ohno, and Toshihiko Baba. Low loss intersection of si photonic wire waveguides. Japanese Journal of Applied Physics, 43(2R):646, 2004.

[29] Cale M Gentry and Miloš A Popović. Dark state lasers. Optics letters, 39(14):4136–4139, 2014.

[30] C Lee Giles and Walter J Wild. Fresnel reflection and transmission at a planar boundary from media of equal refractive indices. Applied Physics Letters, 40(3):210–212, 1982.

[31] George Goubau and F Schwering. On the guided propagation of electromagnetic wave beams. IRE Transactions on Antennas and Propagation, 9(3):248–256, 1961.

[32] Andrew S Grove. Physics and technology of semiconductor devices. John Wiley & Sons Inc, 1967.

[33] D Hatanaka, I Mahboob, K Onomitsu, and H Yamaguchi. Phonon waveguides for electromechanical circuits. Nature nanotechnology, 9(7):520–524, 2014.

[34] Hermann A Haus. Waves and fields in optoelectronics. Prentice-Hall, 1984.

[35] BG Helme and PJ King. The phonon viscosity tensor of Si, Ge, GaAs, and InSb. physica status solidi (a), 45(1), 1978.

[36] TS Hickernell, FM Fliegel, and FS Hickernell. The elastic properties of thin-film silicon nitride. In Ultrasonics Symposium, 1990. Proceedings., IEEE 1990, pages 445–448. IEEE, 1990.

[37] Charles W Holzwarth, Jason S Orcutt, Hanqing Li, Milos A Popovic, Vladimir Stojanovic, Judy L Hoyt, Rajeev J Ram, and Henry I Smith. Localized substrate removal technique enabling strong-confinement microphotonics in bulk si cmos processes. In Conference on lasers and electro-optics, page CThKK5. Optical Society of America, 2008.

[38] Robert Hull. Properties of crystalline silicon. Number 20. IET, 1999.

[39] EP Ippen and RH Stolen. Stimulated brillouin scattering in optical fibers. Applied Physics Letters, 21(11):539–541, 1972.

[40] Eiji Iwase, Pui-Chuen Hui, David Woolf, Alejandro W Rodriguez, Steven G Johnson, Federico Capasso, and Marko Lončar. Control of buckling in large micromembranes using engineered support structures. Journal of Micromechanics and Microengineering, 22(6):065028, 2012.

[41] Steven G Johnson, Mihai Ibanescu, MA Skorobogatiy, Ori Weisberg, JD Joannopoulos, and Yoel Fink. Perturbation theory for maxwell?s equations with shifting material boundaries. Physical review E, 65(6):066611, 2002.

[42] Adam M Jones, Christopher T DeRose, Anthony L Lentine, Douglas C Trotter, Andrew L Starbuck, and Robert A Norwood. Ultra-low crosstalk, cmos compatible waveguide crossings for densely integrated photonic interconnection networks. Optics express, 21(10):12002–12013, 2013.

[43] Ivan P Kaminow. Optical integrated circuits: a personal perspective. Journal of Lightwave Technology, 26(9):994–1004, 2008.

[44] Massoud Kaviany. Principles of heat transfer. John Wiley & Sons, 2002.

[45] Amit Khanna, Youssef Drissi, Pieter Dumon, Roel Baets, Philippe Absil, J Pozo, DMR Lo Cascio, M Fournier, JM Fedeli, L Fulbert, et al. epixfab: the silicon photonics platform. In SPIE Microtechnologies, pages 87670H–87670H. International Society for Optics and Photonics, 2013.

[46] TJ Kippenberg, SM Spillane, and KJ Vahala. Demonstration of ultra-high-q small mode volume toroid microcavities on a chip. Applied Physics Letters, 85(25):6113–6115, 2004.

[47] Tobias J Kippenberg and Kerry J Vahala. Cavity opto-mechanics. Optics Express, 15(25):17172–17205, 2007.

[48] J Lamb, M Redwood, and Z Shteinshleifer. Absorption of compressional waves in solids from 100 to 1000 mc/sec. Physical Review Letters, 3(1):28, 1959.

[49] Lev Davidovich Landau and Eugin M Lifshitz. Course of Theoretical Physics Vol 7: Theory and Elasticity. Pergamon press, 1959.

[50] MF Lewis. Attenuation of high-frequency elastic waves in quartz and fused silica. The Journal of the Acoustical Society of America, 44(3):713–716, 1968.

[51] Dongyao Li and David G Cahill. Attenuation of 7 ghz surface acoustic waves on silicon. Physical Review B, 94(10):104306, 2016.

[52] Heliang Liu, Hwayaw Tam, PKA Wai, and Edwin Pun. Low-loss waveguide crossing using a multimode interference structure. Optics Communications, 241(1):99–104, 2004.

[53] Yangyang Liu and Miloš A Popović. High-Q contacted ring microcavities with scatterer-avoiding “wiggler” bloch wave supermode fields. Applied Physics Letters, 104(20):201102, 2014.

[54] Yangyang Liu, Jeffrey M Shainline, Xiaoge Zeng, and Milos Popovic. Ultra-low-loss waveguide crossing arrays based on imaginary coupling of multimode bloch waves. In Integrated Photonics Research, Silicon and Nanophotonics, pages IM1A–4. Optical Society of America, 2013.

[55] Yangyang Liu, Jeffrey M Shainline, Xiaoge Zeng, and Miloš A Popović. Ultra-low-loss cmos-compatible waveguide crossing arrays based on multimode bloch waves and imaginary coupling. Optics letters, 39(2):335–338, 2014.

[56] Carol Livermore and Joel Voldman. 6.777j/2.751j material properties database. `http://web.mit.edu/~6.777/www/matprops/pecvd_sio2.htm`. Accessed Dec 19, 2016.

[57] Carol Livermore and Joel Voldman. 6.777j/2.751j material properties database. `http://www.mit.edu/~6.777/matprops/pecvd_sin.htm`. Accessed Dec 19, 2016.

[58] Nicolae Lobontiu. Dynamics of microelectromechanical systems, volume 17. Springer Science & Business Media, 2014.

[59] Jing Ma and Michelle L Povinelli. Mechanical kerr nonlinearities due to bipolar optical forces between deformable silicon waveguides. Optics express, 19(11):10102–10110, 2011.

[60] Marc Madou. Fundamentals of microfabrication. 1997. CRC Press LLC. Capítulo, 1, 2003.

[61] C Manolatou, Steven G Johnson, Shanhui Fan, Pierre R Villeneuve, HA Haus, and JD Joannopoulos. High-density integrated optics. In J. Lightwave Technol. Citeseer, 1999.

[62] Radhika Marathe, Bichoy Bahr, Wentao Wang, Zohaib Mahmood, Luca Daniel, and Dana Weinstein. Resonant body transistors in IBM's 32 nm SOI CMOS technology. Microelectromechanical Systems, Journal of, 23(3):636–650, 2014.

[63] HUMPHREY J Maris. Interaction of sound waves with thermal phonons in dielectric crystals. Physical Acoustics, 8:279–345, 2012.

[64] Warren Perry Mason. Crystal physics of interaction processes, volume 23. Academic Press, 1966.

[65] Moritz Merklein, Birgit Stiller, Khu Vu, Stephen J Madden, and Benjamin J Eggleton. A chip-integrated coherent photonic-phononic memory. arXiv preprint arXiv:1608.08767, 2016.

[66] Sayyed Reza Mirnaziry, Christian Wolff, MJ Steel, Benjamin J Eggleton, and Christopher G Poulton. Stimulated brillouin scattering in silicon/chalcogenide slot waveguides. Optics Express, 24(5):4786–4800, 2016.

[67] DT Morelli and JP Heremans. Thermal conductivity of germanium, silicon, and carbon nitrides. Applied physics letters, 81(27):5126–5128, 2002.

[68] COMSOL Multiphysics. Comsol multiphysics user guide (version 4.3 a). COMSOL, AB, pages 39–40, 2012.

[69] R Nava, MP Vecchi, J Romero, and B Fernandez. Akhiezer damping and the thermal conductivity of pure and impure dielectrics. Physical Review B, 14(2):800, 1976.

[70] Norihiko Nishiguchi. Guided acoustic phonons in quantum wires: Theory of phonon fiber. Japanese journal of applied physics, 33(5S):2852, 1994.

[71] A.A. Oliner. Waveguides for acoustic surface waves: A review. Proceedings of the IEEE, 64(5):615–627, May 1976.

[72] Jason S. Orcutt, Benjamin Moss, Chen Sun, Jonathan Leu, Michael Georgas, Jeffrey Shainline, Eugen Zgraggen, Hanqing Li, Jie Sun, Matthew Weaver, Stevan Urošević, Miloš Popović, Rajeev J. Ram, and Vladimir Stojanović. Open foundry platform for high-performance electronic-photonic integration. Opt. Express, 20(11):12222–12232, May 2012.

[73] Miloš Popović. Theory and design of high-index-contrast microphotonic circuits. PhD thesis, Massachusetts Institute of Technology, 2008.

[74] Milos Popovic. Low-loss bloch wave guiding in open structures and highly compact efficient waveguide-crossing arrays, February 14 2012. US Patent 8,116,603.

[75] Milos A Popovic, Erich P Ippen, and Franz X Kartner. Low-loss bloch waves in open structures and highly compact, efficient si waveguide-crossing arrays. In Lasers and Electro-Optics Society, 2007. LEOS 2007. The 20th Annual Meeting of the IEEE, pages 56–57. IEEE, 2007.

[76] Miloš A Popović, Christina Manolatou, and Michael R Watts. Coupling-induced resonance frequency shifts in coupled dielectric multi-cavity filters. Optics express, 14(3):1208–1222, 2006.

[77] Christopher G Poulton, Ravi Pant, Adam Byrnes, Shanhui Fan, MJ Steel, and Benjamin J Eggleton. Design for broadband on-chip isolator using stimulated brillouin scattering in dispersion-engineered chalcogenide waveguides. Optics express, 20(19):21235–21246, 2012.

[78] Christopher G Poulton, Ravi Pant, and Benjamin J Eggleton. Acoustic confinement and stimulated brillouin scattering in integrated optical waveguides. JOSA B, 30(10):2657–2664, 2013.

[79] Kyle Preston, Sasikanth Manipatruni, Alexander Gondarenko, Carl B Poitras, and Michal Lipson. Deposited silicon high-speed integrated electro-optic modulator. Optics express, 17(7):5118–5124, 2009.

[80] Peter T Rakich, Paul Davids, and Zheng Wang. Tailoring optical forces in waveguides through radiation pressure and electrostrictive forces. Optics express, 18(14):14439–14453, 2010.

[81] Peter T Rakich, Miloš A. Popović, Marin Soljačić, and Erich P Ippen. Trapping, corralling and spectral bonding of optical resonances through optically induced potentials. Nature Photonics, 1(11):658–665, 2007.

[82] Peter T Rakich, Charles Reinke, Ryan Camacho, Paul Davids, and Zheng Wang. Giant enhancement of stimulated brillouin scattering in the subwavelength limit. Physical Review X, 2(1):011008, 2012.

[83] R. Ruby. 11e-2 review and comparison of bulk acoustic wave fbar, smr technology. Ultrasonics Symposium, 2007. IEEE, pages 1029–1040, Oct 2007.

[84] Clemens CW Ruppel and Tor A Fjeldly. Advances in surface acoustic wave technology, systems and applications, volume 1. World Scientific, 2000.

[85] Amir H Safavi-Naeini, TP Mayer Alegre, Jasper Chan, Matt Eichenfield, Martin Winger, Qiang Lin, Jeffrey T Hill, DE Chang, and Oskar Painter. Electromagnetically induced transparency and slow light with optomechanics. Nature, 472(7341):69–73, 2011.

[86] Christopher J. Sarabalis, Jeff T. Hill, and Amir H. Safavi-Naeini. Guided acoustic and optical waves in silicon-on-insulator for brillouin scattering and optomechanics. APL Photonics, 1(7), 2016.

[87] Shreyas Y Shah, Mian Zhang, Richard Rand, and Michal Lipson. Master-slave locking of optomechanical oscillators over a long distance. Physical review letters, 114(11):113602, 2015.

[88] Jeffrey M Shainline, Gustavo Fernandes, Zhijun Liu, and Jimmy Xu. Broad tuning of whispering-gallery modes in silicon microdisks. Optics express, 18(14):14345–14352, 2010.

[89] Jeffrey M Shainline, Jason Orcutt, Mark T Wade, Roy Meade, Ofer Tehar-Zehav, Zvi Sternberg, Vladimir Stojanovic, and Milos Popovic. Multi-modal optical microcavities for loss avoidance. In CLEO: Science and Innovations, pages CM1F–2. Optical Society of America, 2013.

[90] Jeffrey M Shainline, Jason S Orcutt, Mark T Wade, Kareem Nammari, Ofer Tehar-Zahav, Zvi Sternberg, Roy Meade, Rajeev J Ram, Vladimir Stojanović, and Miloš A Popović. Depletion-mode polysilicon optical modulators in a bulk complementary metal-oxide semiconductor process. Optics letters, 38(15):2729–2731, 2013.

[91] RM Shelby, MD Levenson, and PW Bayer. Guided acoustic-wave brillouin scattering. Physical Review B, 31(8):5244, 1985.

[92] Heedeuk Shin, Jonathan A Cox, Robert Jarecki, Andrew Starbuck, Zheng Wang, and Peter T Rakich. Control of coherent information via on-chip photonic–phononic emitter–receivers. Nature communications, 6, 2015.

[93] Heedeuk Shin, Wenjun Qiu, Robert Jarecki, Jonathan A Cox, Roy H Olsson III, Andrew Starbuck, Zheng Wang, and Peter T Rakich. Tailorable stimulated brillouin scattering in nanoscale silicon waveguides. Nature communications, 4, 2013.

[94] Soitec. PHOTONICS-SOI for high-speed optical transceivers in data centers. `https://www.soitec.com/en/products/photonics-soi`, 2017 (accessed August 29, 2017).

[95] Richard Soref. The past, present, and future of silicon photonics. IEEE Journal of selected topics in quantum electronics, 12(6):1678–1687, 2006.

[96] Thomas Stark, Matthias Imboden, Sabri Kaya, Alket Mertiri, Jackson Chang, Shyamsunder Erramilli, and David Bishop. A MEMS tunable mid-infrared plasmonic spectrometer. ACS Photonics, 2015.

[97] Howard R Stuart. Waveguide lenses with multimode interference for low-loss slab propagation. Optics letters, 28(22):2141–2143, 2003.

[98] Chen Sun, Mark T Wade, Yunsup Lee, Jason S Orcutt, Luca Alloatti, Michael S Georgas, Andrew S Waterman, Jeffrey M Shainline, Rimas R Avizienis, Sen Lin, et al. Single-chip microprocessor that communicates directly using light. Nature, 528(7583):534–538, 2015.

[99] Xiankai Sun, King Y Fong, Chi Xiong, Wolfram HP Pernice, and Hong X Tang. Ghz optomechanical resonators with high mechanical q factor in air. Optics express, 19(22):22316–22321, 2011.

[100] Xiankai Sun, Ke Xu, and Hong X Tang. Monolithically integrated, ultrahigh-frequency cavity nano-optoelectromechanical system with on-chip germanium waveguide photodetector. Optics letters, 39(8):2514–2517, 2014.

[101] Siddharth Tallur and Sunil A Bhave. A silicon electromechanical photodetector. Nano letters, 13(6):2760–2765, 2013.

[102] Raphaël Van Laer, Bart Kuyken, Dries Van Thourhout, and Roel Baets. Interaction between light and highly confined hypersound in a silicon photonic nanowire. Nature Photonics, 9(3):199–203, 2015.

[103] Charles Vassallo. Optical waveguide concepts. Elsevier, 1991.

[104] Ru Ju Wang, Wei Hua Wang, Feng Ying Li, Li Min Wang, Yong Zhang, Ping Wen, and Ji Fang Wang. The grüneisen parameter for bulk amorphous materials. Journal of Physics: Condensed Matter, 15(3):603, 2003.

[105] Michael Robert Watts. Polarization independent microphotonic circuits. PhD thesis, Massachusetts Institute of Technology, 2005.

[106] Gustavo S Wiederhecker, Long Chen, Alexander Gondarenko, and Michal Lipson. Controlling photonic structures using optical forces. Nature, 462(7273):633–636, 2009.

[107] Gustavo S Wiederhecker, Sasikanth Manipatruni, Sunwoo Lee, and Michal Lipson. Broadband tuning of optomechanical cavities. Optics Express, 19(3):2782–2790, 2011.

[108] Kirt R Williams, Kishan Gupta, and Matthew Wasilik. Etch rates for micromachining processing-part ii. Journal of microelectromechanical systems, 12(6):761–778, 2003.

[109] Kirt R Williams and Richard S Muller. Etch rates for micromachining processing. Journal of Microelectromechanical systems, 5(4):256–269, 1996.

[110] C Wolff, R Soref, CG Poulton, and BJ Eggleton. Germanium as a material for stimulated brillouin scattering in the mid-infrared. Optics express, 22(25):30735–30747, 2014.

[111] TO Woodruff and H Ehrenreich. Absorption of sound in insulators. Physical Review, 123(5):1553, 1961.

[112] GQ Wu, DH Xu, B Xiong, and YL Wang. Effect of air damping on quality factor of bulk mode microresonators. Microelectronic Engineering, 103:86–91, 2013.

[113] Qianfan Xu, Bradley Schmidt, Sameer Pradhan, and Michal Lipson. Micrometre-scale silicon electro-optic modulator. nature, 435(7040):325, 2005.

[114] Yi Yu, Mikkel Heuck, Sara Ek, Nadezda Kuznetsova, Kresten Yvind, and Jesper Mørk. Experimental demonstration of a four-port photonic crystal cross-waveguide structure. Applied Physics Letters, 101(25):251113, 2012.

[115] Yang Zhang, Amir Hosseini, Xiaochuan Xu, David Kwong, and Ray T Chen. Ultralow-loss silicon waveguide crossing using bloch modes in index-engineered cascaded multimode-interference couplers. Optics letters, 38(18):3608–3611, 2013.

[116] Yi Zhang, Shuyu Yang, Andy Eu-Jin Lim, Guo-Qiang Lo, Christophe Galland, Tom Baehr-Jones, and Michael Hochberg. A cmos-compatible, low-loss, and low-crosstalk silicon waveguide crossing. IEEE Photon. Technol. Lett, 25(5):422–425, 2013.

Appendix A

A 3D Finite Difference Photonic Eigenmode Solver

A.1 The Discrete Electromagnetic Wave Equation

The electromagnetic wave equation for a linear non-magnetic and source-free medium is

$$(\nabla^2 - \mu_0 \overline{\overline{\varepsilon}} \partial_t^2)\mathbf{E} = 0 \tag{A.1}$$

which is an eigenvalue problem that can be solved numerically [22]. On a discrete 3D grid, defining the fore fields on the edges of a pixel and the back fields on the faces of a pixel, the discrete fore curl operator $\tilde{\nabla}\times$ operates on a fore field $\tilde{\mathbf{F}}$ to yield a back field $\hat{\mathbf{F}}$ (Fig. A.1.1), and vice versa. Assuming a harmonic time dependence of $\exp(j\omega t)$, the wave equation (Eqn. A.1) can be discretized as

$$\overline{\overline{\varepsilon_r}}^{-1} \hat{\nabla} \times \tilde{\nabla} \times \tilde{\mathbf{E}} = k_0^2\ \tilde{\mathbf{E}} \tag{A.2}$$

which is an eigenequation with the square of the free space wavenumber k_0 being the eigenvalue and eigenmode fore field $\tilde{\mathbf{E}}$ being the eigenvector.

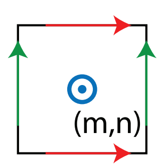

Figure A.1.1: A 2D pixel with fore fields defined on the edges (red and green) and a back field defined on the face center (blue).

$\tilde{E}_x$	$M \times (N+1) \times (P+1)$	$\hat{F}_x$	$(M+1) \times N \times P$
$\tilde{E}_y$	$(M+1) \times N \times (P+1)$	$\hat{F}_y$	$M \times (N+1) \times P$
$\tilde{E}_z$	$(M+1) \times (N+1) \times P$	$\hat{F}_z$	$M \times N \times (P+1)$

Table A.1: Length of column vectors describing the three components of the fore electric field $\tilde{\mathbf{E}}$ and the back field $\hat{\mathbf{F}} = \tilde{\nabla} \times \tilde{\mathbf{E}}$, defined on an $M \times N \times P$ grid.

A.2 The Fore and Back Curl Operators

For a three dimensional grid of size $M \times N \times P$, Table A.1 lists the dimensions of the components of the fore electric field $\tilde{\mathbf{E}}$ and the back field $\hat{\mathbf{F}} = \tilde{\nabla} \times \tilde{\mathbf{E}}$. Collapsing $\tilde{\mathbf{E}}$ into a column vector of length $[M \times (N+1) \times (P+1)] + [(M+1) \times N \times (P+1)] + [(M+1) \times (N+1) \times P]$, the $\overline{\overline{\varepsilon_r}}^{-1} \hat{\nabla} \times \tilde{\nabla} \times$ operator in Eqn. A.2 becomes a square matrix, as shown below.

Taking the fore cur on the fore electric field,

$$\tilde{\nabla} \times \tilde{\mathbf{E}} = \begin{vmatrix} \hat{\mathrm{i}} & \hat{\mathrm{j}} & \hat{\mathrm{k}} \\ \tilde{\partial}_x & \tilde{\partial}_y & \tilde{\partial}_z \\ \tilde{E}_x & \tilde{E}_y & \tilde{E}_z \end{vmatrix} = \begin{bmatrix} 0 & -\tilde{\partial}_z & \tilde{\partial}_y \\ \tilde{\partial}_z & 0 & -\tilde{\partial}_x \\ -\tilde{\partial}_y & \tilde{\partial}_x & 0 \end{bmatrix} \cdot \begin{bmatrix} \tilde{E}_x \\ \tilde{E}_y \\ \tilde{E}_z \end{bmatrix} \tag{A.3}$$

The discrete fore curl operator $\tilde{\nabla}\times$ can therefore be written in matrix form

$$\tilde{\nabla}\times = \tilde{\mathbf{T}} = \begin{bmatrix} \tilde{\mathbf{T}}_{xx} & \tilde{\mathbf{T}}_{xy} & \tilde{\mathbf{T}}_{xz} \\ \tilde{\mathbf{T}}_{yx} & \tilde{\mathbf{T}}_{yy} & \tilde{\mathbf{T}}_{yz} \\ \tilde{\mathbf{T}}_{zx} & \tilde{\mathbf{T}}_{zy} & \tilde{\mathbf{T}}_{zz} \end{bmatrix} = \begin{bmatrix} 0 & -\tilde{\partial}_z & \tilde{\partial}_y \\ \tilde{\partial}_z & 0 & -\tilde{\partial}_x \\ -\tilde{\partial}_y & \tilde{\partial}_x & 0 \end{bmatrix}, \qquad \tilde{\mathbf{T}}_{xx} = \tilde{\mathbf{T}}_{yy} = \tilde{\mathbf{T}}_{zz} = 0 \tag{A.4}$$

The off-diagonal submatrices can be constructed by considering its operation on components of the fore electric field $\tilde{\mathbf{E}}$. For example, the y component of $\tilde{\mathbf{E}}$ is defined on all pixel edges parallel to the y axis (red arrows in Fig. A.2.1), forming a column vector $\tilde{E}_y$ of length $(M+1) \times N \times (P+1)$. $\tilde{\mathbf{T}}_{xy}$ operates on $\tilde{E}_y$ to take the difference between adjacent pixels along $-z$ direction,

$$\tilde{\mathbf{T}}_{xy} = -\tilde{\partial}_z = -\frac{1}{\Delta z} \cdot \overbrace{\begin{bmatrix} -1 & \overleftrightarrow{\scriptstyle (M+1)\times N} & 1 & & & \\ & -1 & & & 1 & \\ & & \ddots & & & \ddots \\ & & & -1 & & & 1 \end{bmatrix}}^{(M+1)\times N\times(P+1)} \left.\vphantom{\begin{bmatrix} 1\\1\\1\\1 \end{bmatrix}}\right\} {\scriptstyle (M+1)\times N\times P} \tag{A.5}$$

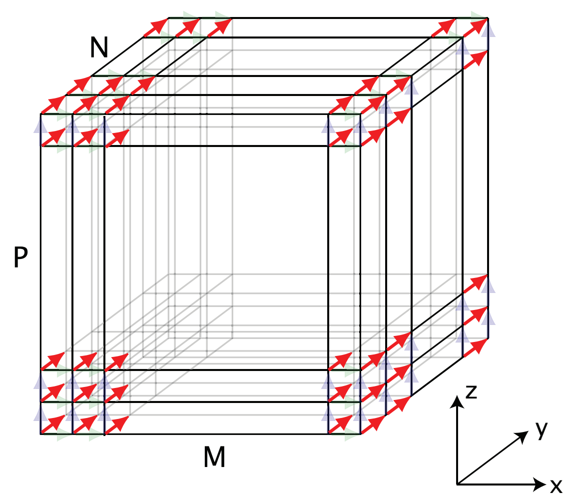

Figure A.2.1: $\tilde{E}_y$, y component of the fore electric field $\tilde{\mathbf{E}}$, defined on an $M \times N \times P$ grid.

resulting in a back field with dimension $(M+1)\times N \times P$. Let the resulting back field from taking the fore curl on the fore electric field be

$$\hat{\mathbf{F}} = \tilde{\nabla} \times \tilde{\mathbf{E}} \tag{A.6}$$

Eqn. A.2 becomes

$$\overline{\overline{\varepsilon_r}}^{-1} \hat{\nabla} \times \hat{\mathbf{F}} = k_0^2 \, \tilde{\mathbf{E}} \tag{A.7}$$

The back curl operator $\hat{\nabla}\times$ can again be constructed in matrix form:

$$\hat{\nabla}\times = \hat{\mathbf{T}} = \begin{bmatrix} \hat{\mathbf{T}}_{xx} & \hat{\mathbf{T}}_{xy} & \hat{\mathbf{T}}_{xz} \\ \hat{\mathbf{T}}_{yx} & \hat{\mathbf{T}}_{yy} & \hat{\mathbf{T}}_{yz} \\ \hat{\mathbf{T}}_{zx} & \hat{\mathbf{T}}_{zy} & \hat{\mathbf{T}}_{zz} \end{bmatrix} = \begin{bmatrix} 0 & -\hat{\partial}_z & \hat{\partial}_y \\ \hat{\partial}_z & 0 & -\hat{\partial}_x \\ -\hat{\partial}_y & \hat{\partial}_x & 0 \end{bmatrix} \tag{A.8}$$

The submatrix $\hat{\mathbf{T}}_{xy}$ operates on $\hat{F}_y$ (Fig. A.2.2), and takes the form

$$\hat{\mathbf{T}}_{xy} = -\hat{\partial}_z = -\frac{1}{\Delta z} \cdot \overbrace{\left[\begin{array}{cccccc} b_f & & & & & \\ & \ddots & & & & \\ & & b_f & & & \\ \hline -1 & \xleftrightarrow{M\times(N+1)} & 1 & & & \\ & -1 & & 1 & & \\ & & \ddots & & \ddots & \\ & & & -1 & & 1 \\ \hline & & & b_b & & \\ & & & & \ddots & \\ & & & & & b_b \end{array}\right]}^{\text{M}\times\text{(N+1)}\times\text{P}} \left.\vphantom{\begin{array}{c}1\\1\\1\\1\\1\\1\\1\\1\\1\\1\end{array}}\right\} \text{M}\times\text{(N+1)}\times\text{(P+1)} \tag{A.9}$$

The back field $\hat{F}_y$ has $M \times (N+1) \times P$ elements defined on pixel faces on a $M \times N \times P$ grid (Fig. A.2.2). The middle rows of the $\hat{\mathbf{T}}_{xy}$ submatrix takes the difference adjacent pixels along $-z$ direction, to result in a fore field of size $M \times (N+1) \times (P-1)$ matching the dimension of the middle rows of the fore electric field $\tilde{\mathbf{E}}$, excluding only the top and bottom surfaces, on the right side of Eqn. A.7. The top (bottom) $M \times (N+1)$ rows of $\hat{\mathbf{T}}_{xy}$ account for boundary condition on

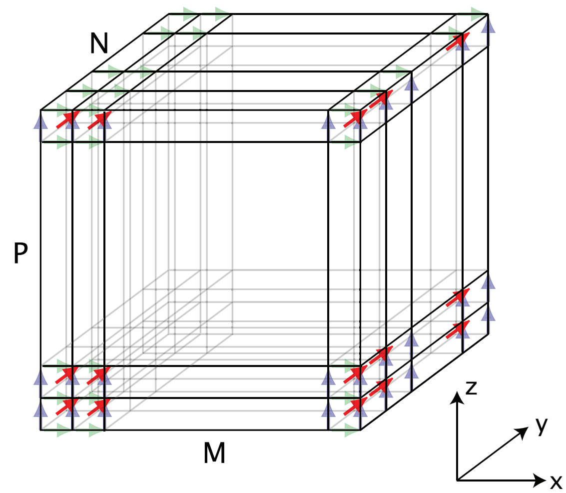

Figure A.2.2: $\hat{F}_y$, y component of the back field resulting from a fore curl operation on a fore electric field $\hat{\mathbf{F}} = \tilde{\nabla} \times \tilde{\mathbf{E}}$, defined on a M×N×P grid.

the top (bottom) surface of the grid. The perfect electric conductor (PEC) boundary condition requires that $\hat{n} \times \mathbf{E} = 0$ and $\hat{n} \cdot \mathbf{H} = 0$, which in the case of $\hat{\mathbf{T}}_{xy}$ sets $E_y = 0$ on the boundary, i.e. $b_{\mathrm{PEC}} = 0$. The perfect magnetic conductor (PMC) boundary condition requires $\hat{n} \times \mathbf{E} = 0$ and $\hat{n} \cdot \mathbf{H} = 0$. Using the method of images, $\partial_z E_x = 0$ and $F_y = -\partial_x E_z$ is symmetric across the boundary, i.e. $b_{\mathrm{PMC}} = 2$. With $\tilde{\nabla}\times$ and $\hat{\nabla}\times$ both constructed in matrix form, Eqn. A.2 becomes $\mathbf{H} \cdot \tilde{\mathbf{E}} = k_0^2 \tilde{\mathbf{E}}$, where $\mathbf{H} = \overline{\overline{\varepsilon_r}}^{-1} \cdot \hat{\mathbf{T}} \cdot \tilde{\mathbf{T}}$ and

$$\overline{\overline{\varepsilon_r}}^{-1} = \begin{bmatrix} \varepsilon_x^{-1}(1) & & & & & & & & \\ & \ddots & & & & & & & \\ & & \varepsilon_x^{-1}(\mathrm{end}) & & & & & & \\ & & & \varepsilon_y^{-1}(1) & & & & & \\ & & & & \ddots & & & & \\ & & & & & \varepsilon_y^{-1}(\mathrm{end}) & & & \\ & & & & & & \varepsilon_z^{-1}(1) & & \\ & & & & & & & \ddots & \\ & & & & & & & & \varepsilon_z^{-1}(\mathrm{end}) \end{bmatrix} \tag{A.10}$$

is a diagonal matrix when the grid axes are aligned with material principal axes, which describes the spatial distribution of relative permittivity of an index structure. For a given k_0, the Bloch-Floquent boundary condition can be further implemented in $\mathbf{H}$ to simulate periodic structures.

A.3 Two Test Cases

In the following section, we use the 3D eigenmode solver described above to solve two simple structures with known analytical solutions, a homogeneous rectangular box with uniform index distribution and an inhomogeneous box with 1D parabolic index distribution.

A.3.1 A Homogeneous Box

For a charge-free rectangular box of dimension $A \times B \times C$ and uniform index $\varepsilon_r = 1$, with PEC boundaries on all 6 faces (Fig. A.3.1), the analytical solution of the electric field components

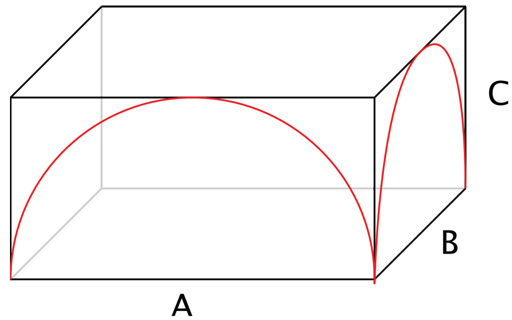

Figure A.3.1: A rectangular box of size $A \times B \times C$ and uniform index $n = 1$.

that satisfy Eqn.A.1 are given by

$$\begin{bmatrix} E_x \\ E_y \\ E_z \end{bmatrix} = \begin{bmatrix} E_{x0}\cos(k_x x)\sin(k_y y)\sin(k_z z) \\ E_{y0}\sin(k_x x)\cos(k_y y)\sin(k_z z) \\ E_{z0}\sin(k_x x)\sin(k_y y)\cos(k_z z) \end{bmatrix} e^{-i\omega t} \tag{A.11}$$

with

$$k_x = \frac{N_x \pi}{A}, k_y = \frac{N_y \pi}{B}, k_z = \frac{N_z \pi}{C} \tag{A.12}$$

where N_x, N_y and N_z are integers, and

$$k_x^2 + k_y^2 + k_z^2 = k_0^2 \tag{A.13}$$

Setting $N_x = N_y = 1$ and $N_z = 0$, one resonant mode of this structure has $k_x = \frac{\pi}{A}$, $k_y = \frac{\pi}{B}$, $k_z = 0$ and

$$k_0 = \pi\sqrt{\frac{1}{A^2} + \frac{1}{B^2}} \tag{A.14}$$

Solving the same problem using the eigenmode solver described in this section on a $15\times15\times15$ grid, Fig. A.3.2 shows the elements in the discrete operators $\tilde{\nabla}\times$, $\hat{\nabla}\times$ and $\hat{\nabla}\times\tilde{\nabla}\times$. Figure A.3.3 shows 2D slices of the electric field components of the numerically solved eigenmode. Comparing to the analytical solution (Eqn. A.14), error in numerically solved wave number $|k_{0,\text{numerical}} - k_0|$ shows $O(dx^2)$ dependence on grid size (Fig. A.3.4).

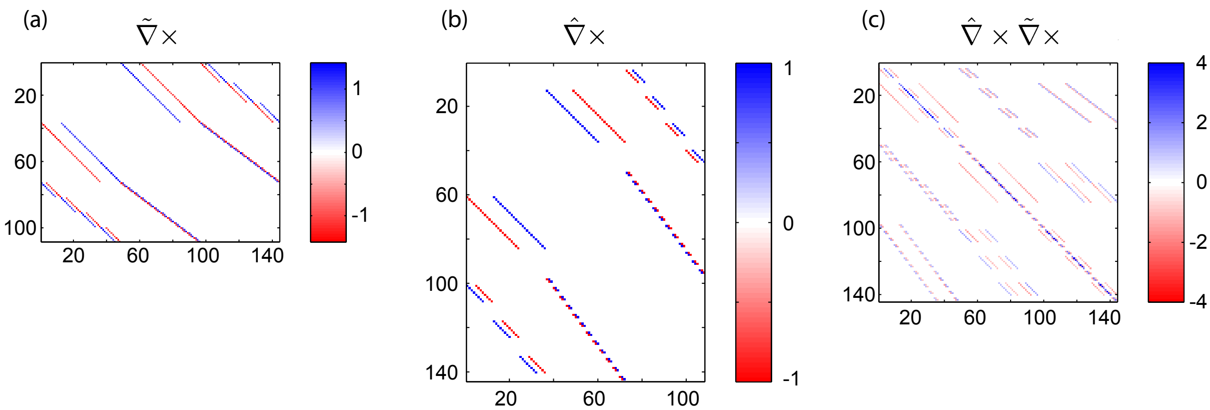

Figure A.3.2: Elements of the discrete curl operators in matrix form on a $15 \times 15 \times 15$ grid for numerically solving the wave equation (Eqn. A.2). (a) Fore curl $\tilde{\nabla}\times$ (b) back curl $\hat{\nabla}\times$ (c) $\hat{\nabla} \times \tilde{\nabla}\times$.

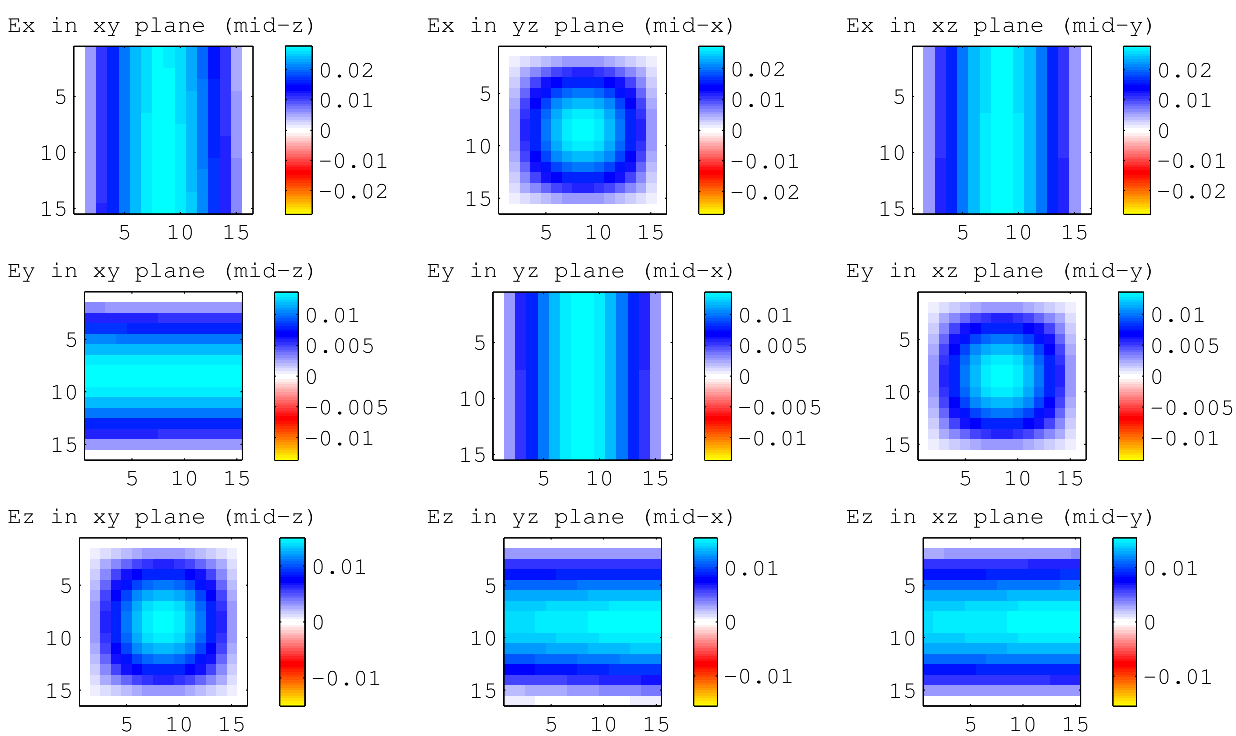

Figure A.3.3: Simulated eigenmode fields of a homogeneous rectangular box on a $15 \times 15 \times 15$ grid with PEC boundary condition on all 6 faces.

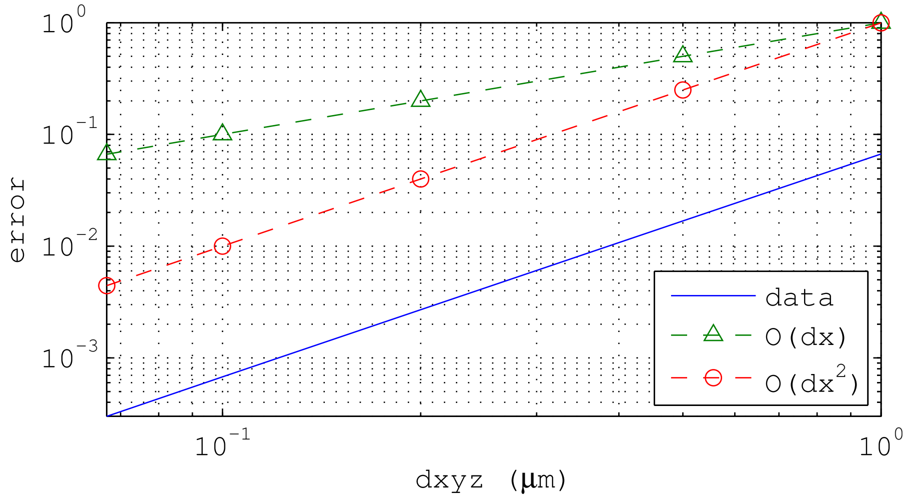

Figure A.3.4: Error between numerically solved wave number and analytical solution (Eqn. A.14) $|k_{0,\text{numerical}} - k_0|$ vs. grid size $dxyz$ for a homogeneous box.

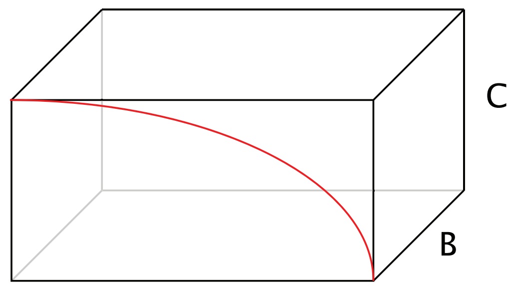

Figure A.3.5: A rectangular box of size $A \times B \times C$ and 1D parabolic index distribution $\varepsilon_r = \varepsilon_M(1 - \alpha x^2)$.

A.3.2 An Inhomogeneous Box with 1D Parabolic Index Distribution

The analytical solution of an inhomogeneous rectangular box of dimension $A \times B \times C$ and index distribution $\varepsilon_r = \varepsilon_M(1-\alpha x^2)$, with PEC boundaries on all 6 faces (Fig. A.3.5–A.3.6) is given by

$$\mathbf{E} = \hat{\mathbf{z}} \cdot E_{z0} \exp(-\alpha x^2) \tag{A.15}$$

with wave number

$$k_0 = \sqrt{\frac{2\alpha}{\varepsilon_M}} \tag{A.16}$$

Figure A.3.3 shows 2D slices of the electric field components of the numerically solved eigenmode using the eigenmode solver. Comparing to the analytical solution (Eqn. A.16), error in numerically solved wave number $|k_{0,\text{numerical}} - k_0|$ again shows $O(dx^2)$ dependence on grid size (Fig. A.3.8).

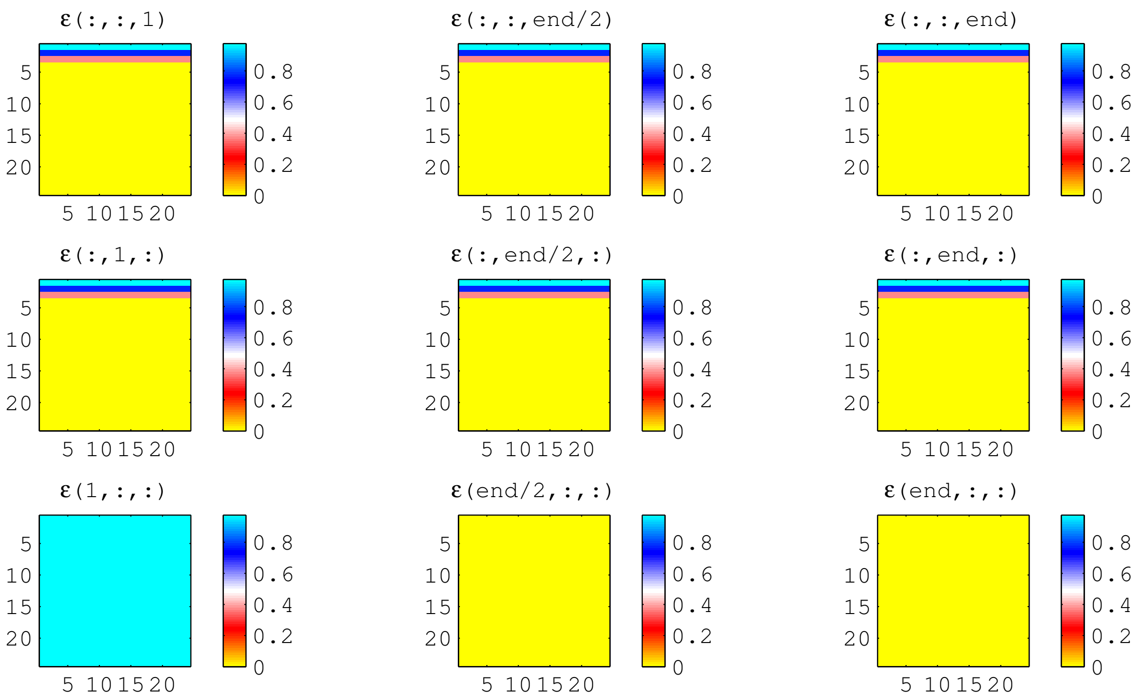

Figure A.3.6: 2D slices of the relative permittivity ε_r of a rectangular box with 1D parabolic index distribution $\varepsilon_r = \varepsilon_M(1 - \alpha x^2)$.

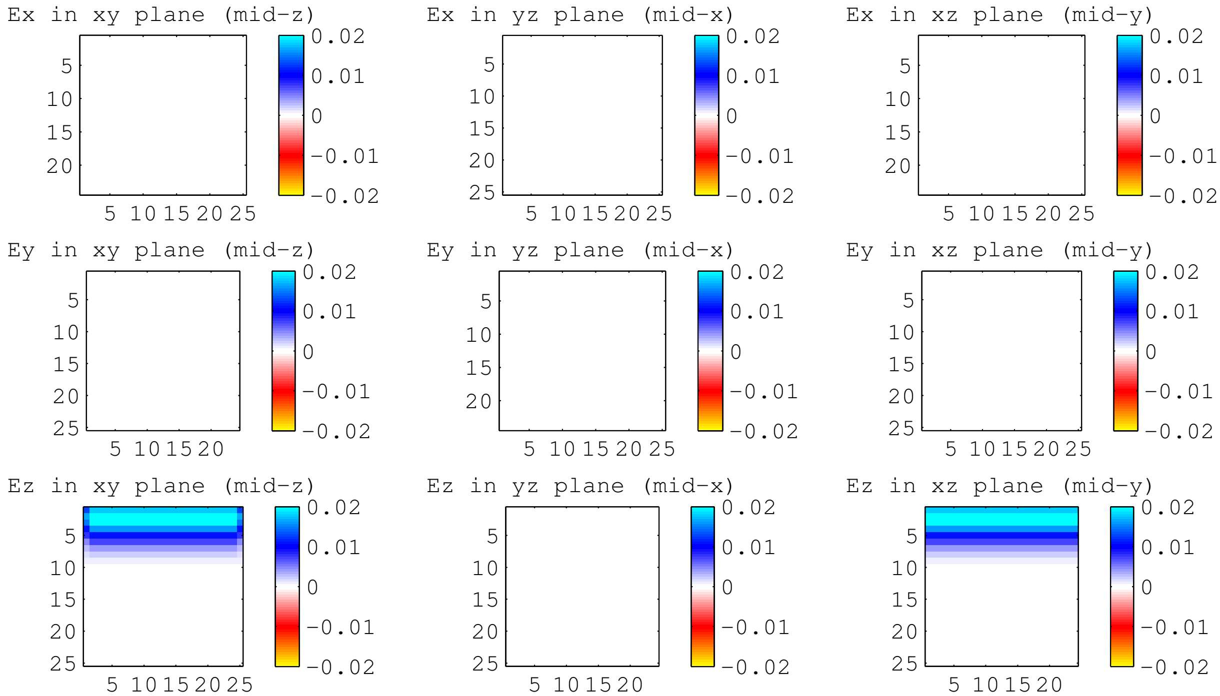

Figure A.3.7: Simulated eigenmode fields of an inhomogeneous rectangular box with 1D parabolic index distribution on a $25 \times 25 \times 25$ grid with PEC boundary condition on all 6 faces.

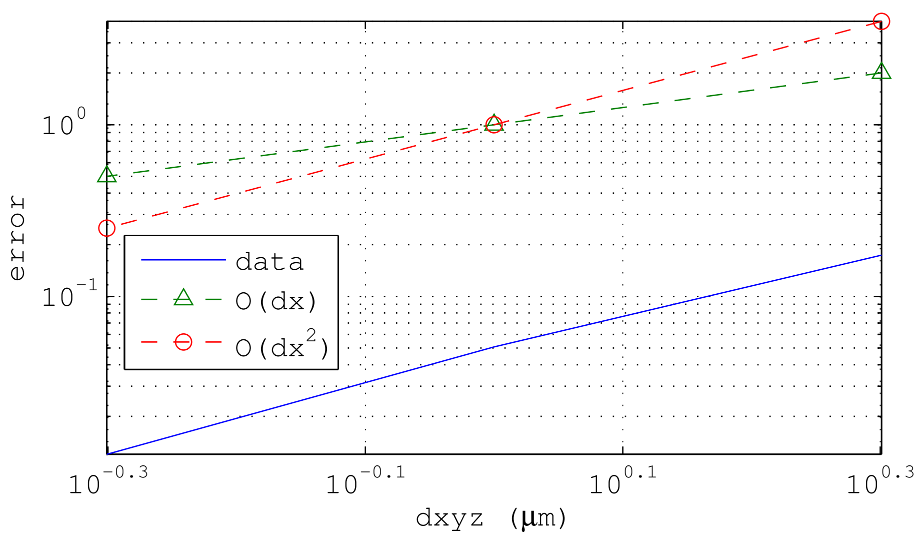

Figure A.3.8: Error between numerically solved wave number and analytical solution (Eqn. A.16) $|k_{0,\text{numerical}} - k_0|$ vs. grid size $dxyz$ for an inhomogeneous box with 1D parabolic index distribution.

Appendix B

Fabrication Techniques

B.1 Silicon Device Release in SOI

The wiggler resonators discussed in Chapter 2.4 are fabricated through IMEC (via ePIXfab) in a custom SOI process with a 220 nm silicon device layer, and released at the Colorado Nanofabrication Lab (CNL) and the MEMS lab at University of Colorado at Boulder. Figure B.1.1 shows the process flow for selectively suspending these structures in post processing.

The chip is coated with negative photoresist NR9-1000P on a spinner at 4000 rpm for 40 s, followed by a soft bake on a hot plate at 150°C for 60 s to obtain a thickness of 900 nm. A Chromium mask is created using Heidelberg DWL 66FS mask generator with etch windows and

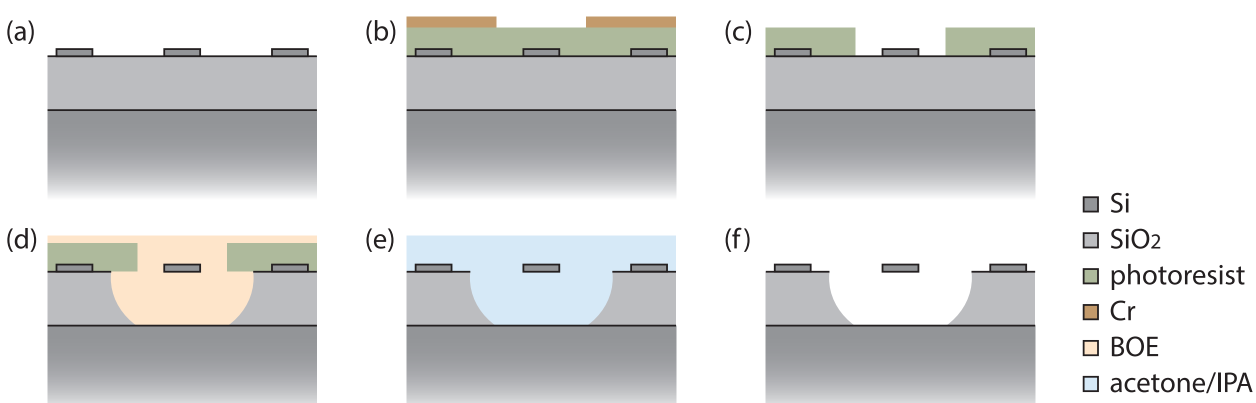

Figure B.1.1: Process flow for suspending silicon structures in an SOI process. A negative resist is spun on the substrate and patterned with a chromium mask to serve as etch windows; oxide under the resonator is then selectively etched with a buffered HF solution (BOE); liquid under device layer is replaced with acetone and IPA and eliminated in a CO_2 critical point dryer.

alignment marks. Figure B.1.2a shows an example of a developed mask, with a single vertical strip covering the resonator region of an entire column of devices.

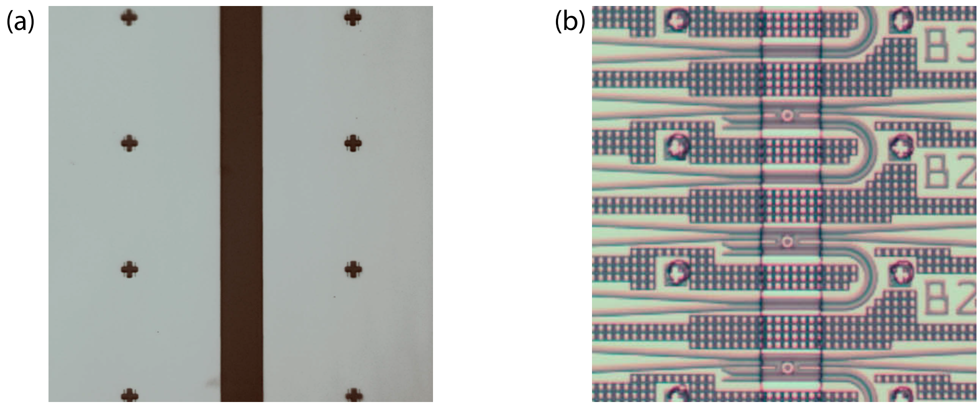

Figure B.1.2: Optical micrographs showing the definition of etch windows through photolithography. (a) Patterned Chromium mask with alignment marks and a vertical strip as etch window. (b) Developed photoresist using the mask shown in (a).

The pattern is transferred to the photoresist using a KARL SUSS MJB3 mask aligner with 15 s exposure, followed by a post-exposure bake on a hot plate at 100°C for 60 s. The photoresist is developed with RD-6 immersion for 3 s, rinsed with DI water and inspected under a microscope. Figure B.1.2b shows a chip with developed photoresist, exposing a vertical etch window as defined by the mask shown in Fig. B.1.2a.

The chip (covered by developed photoresist as an etch mask) is then immersed in 5:1 buffered HF solution (BOE) at room temperature for 30 min, to remove the oxide under the Si device layer within etch windows defined by the patterned photoresist at an etch rate around 100 nm/min. After etching, the chip is transferred to a small container with minimal amount of BOE to prevent exposing the chip surface to air. The liquid immersing the chip is replaced with DI water for rinsing, followed by acetone for removing the remaining photoresist, and subsequently IPA or methanol, with special attention taken to not have the chip above liquid surface at any time, lest the liquid trapped under the suspended structures evaporate and surface tension cause the resonators or waveguides to stick to the bottom substrate. The immersed chip is dried in a Bal-Tec/Leica CPD030 critical point dryer, where liquid methanol is replaced with liquid CO_2. During critical point drying, CO_2 is brought, from a high pressure liquid state, to a critical temperature and pressure where liquid and gas phases are indistinguishable, so from this supercritical fluid state to a gas state at room temperature and atmosphere pressure, there is no abrupt change in state (or density), so the damaging effects associated with surface tension can be avoided. Figure B.1.2b shows micrograph of a chip with suspended wiggler resonators, using rectangular shaped etch windows as shown in Fig. B.1.2a. The fallen square pieces visible in Fig. B.1.2b are Si density fill shapes which are standard in various fabrication processes. Excluding density fill around structures to be suspended in mask layout prior to the fabrication of the chips, or reducing the size of the etch windows can both prevent these squares from falling on nearby photonic structures, causing scattering problems. In Fig. B.1.2a, the alignment of the etch mask and the photonic chip is off by a few microns. This could be improved by adding an edge bead removal step after spinning on photoresist.

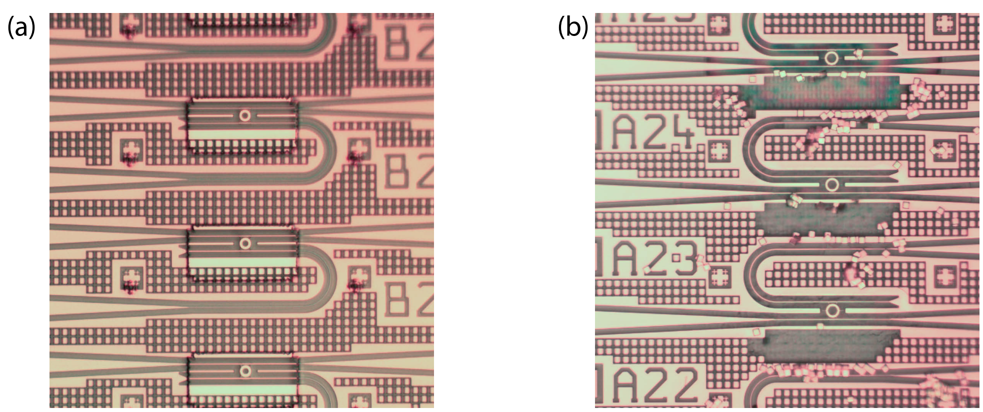

Figure B.1.3: Optical micrographs showing the suspending of wiggler resonators. (a) Developed photoresist with individual rectangular etch windows instead of a vertical strip across multiple devices. (b) Released wigglers, with fallen density fill.

Figure B.1.4 shows SEMs of two released wiggler resonators with four and six contacts connecting to the input and output bus waveguides. Resonators with outer radii ranging from $2-4\,\mu$m, ring waveguide widths $700-1000$ nm, and contact widths $100-300$ nm are successfully suspended. Contacts start to break at 100 nm width (Fig. B.1.4 b).

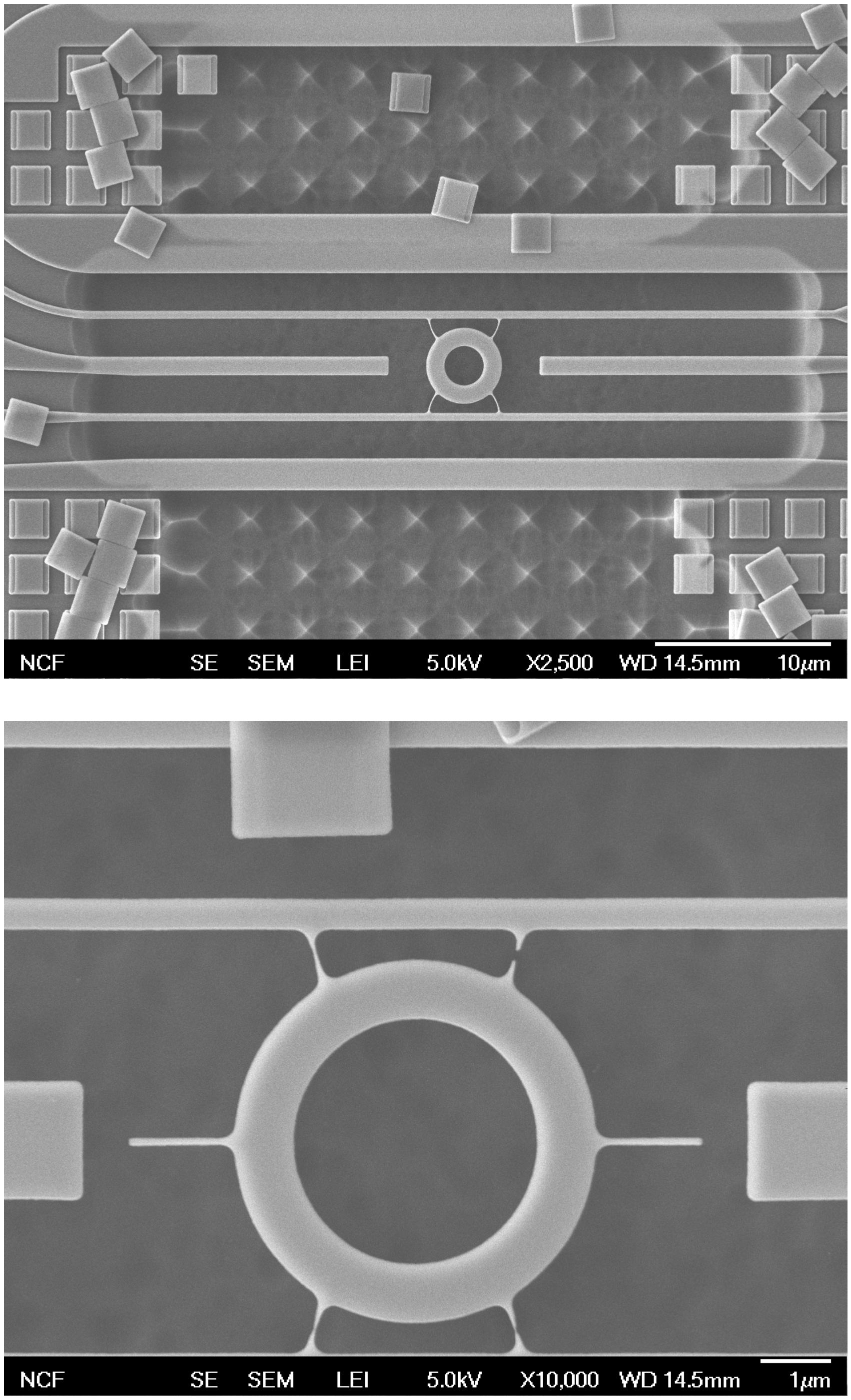

Figure B.1.4: SEMs of suspended wiggler resonators with (a) four and (b) six contacts connecting to input and ouput bus waveguides.

B.2 Silicon Substrate Removal for Zero-change CMOS Chips

The chips are fabricated in IBM's 45nm CMOS process, and the post-processing for substrate removal is done at Center for Nanoscale Systems (CNS) at Harvard University. Each individual chip has a size of $3\,\mathrm{mm}\times 6\,\mathrm{mm}$, and the total thickness of Si substrate to be removed is $250\,\mu$m. The first $\sim 235\,\mu$m is removed using a regular non-Bosch process in a SPTS Rapier Si DRIE etcher for better uniformity and higher etch rate, and while the remaining $\sim 15\,\mu$m is removed in a in-house XeF_2 etcher for better selectivity against SiO_2.

RIE etching of the first $235\,\mu$m is done in two steps. A CMOS chip, and a bare Si chip cleaved to be slightly larger in size, are both mounted on the same glass slide with crystalbond. A kapton tape covers a small portion of the bare Si chip, so the surface underneath is not etched during RIE and can serve as an initial thickness reference. The glass slide is further mounted on a 6 inch oxide wafer, as a standard requirement of the etcher. Since the thickness of Si to be removed here is much larger than most applications, and RIE etch rate selectivity for Si vs. SiO_2 is roughly 150:1 [108], the oxide wafer (with $2\,\mu$m of thermal oxide on Si) is further coated with $\sim 10\,\mu$m of photoresist AZ4620 at 2000 rpm and baked at $90\,^{\circ}$C for 30 min. After a non-Bosch timed etch of 300 s, the bare Si chip is inspected under an optical profilometer, with the kapton tape removed. Step height different from the first etch step is measured and etch rate calculated ($18.10\,\mu$m/min). A new piece of kapton tape is re-placed to cover part of the bare Si reference chip, and a second timed etch is done using the same recipe, with a target total etch thickness of $235\,\mu$m, and calibrated etch rate from the first etch. The bare Si chip is measured again after the second etch, for final thickness removed using RIE ($236.6\,\mu$m, with a calculated etch rate of $18.08\,\mu$m/min in the second RIE etch step).

Since XeF_2 has a severe loading effect and etch rate can be greatly reduced if total surface area is large, the calibration of etch rate is done separately, with a bare Si chip of the same size. A Mitutoyo digital Calibre is used to measure the thickness of the Si chip before and after a XeF_2 etch with 40 s pulses $\times$ 40 cycles (~ 1 hr). Si thickness removed is $\sim 6\,\mu$m (at the center of the chip where etch rate is slowest). To remove the remaining $\sim 15\,\mu$m of Si on the CMOS chip, 120 cycles of 40 s pulses are used, with an estimated slight over etch. Photonic structures are clearly visible after this XeF_2 etch. Contact profilometer measurements show no abrupt step difference in final chip surface, confirming that the device layer is intact.

For future experiments, the target RIE removal thickness can be increased from the current $235\,\mu$m to $240 - 245\,\mu$m with the etch time for the first RIE step increased to 400 s, since etch rate seems consistent between two etches with the same conditions, if the etch times are roughly close. This would reduce the total process time, and improve overall surface uniformity.